Study on bonding mechanism and properties evaluation in diffusion bonding of magnesium/aluminum alloys

Ming Zhao

Saitama Institute of Technology

October，2014

Contents

Chapter 1 Introduction

1.1 Background and significance

Nowadays, the increasing of energy and the environment pressure to save the limited earth resources and to reduce environmental pollution has become a very important focus which all of the world's countries have concerned. With the development of science and technology, the consumption of metal materials has risen sharply; the mineral resources of metal commonly used on the earth are becoming poor [1, 2]. One of the lightest engineering materials, magnesium alloy has a good thermal conductivity, easy processing and recyclability, and damping vibration, electromagnetic shielding and other functions [3]. Therefore, if possible magnesium alloy is used to replace a lot of aluminum alloy and steel structure material, the premise of guarantee product performance and product weight can be greatly reduced, it will greatly reduce the energy consumption and environmental pollution, it has huge market potential in the place such as aerospace, automobile transportation and electronic information [4]. In automobile industry, for example, studies have shown that the fuel used in automobiles and in which fuel of 60% was used in self-respect; the fuel was saved by 5.5% because of reducing 10% weight of the car. As demands are rising in the world, the car market competitions in the developed countries of auto manufacturers spend large sum of money on the research and development of the automotive lightweight materials [5]. Aluminum alloy materials used on automotive products at home and abroad, the development of lightweight play a dominant role in the production process of the car [6]. The magnesium alloy casting which used in the cars are growing fast and the consumption of the magnesium alloy has become the second in the consumption of the metal as while as the aluminum.

In present, with a variety of research and development of high

performance magnesium alloy, magnesium alloy structure is beginning to get application in all fields. Structural connection technology is indispensable to the widespread use of support, so the connection technology degree will directly affect the development of magnesium alloy in use process [7]. With magnesium and magnesium alloys used in various industries, the rapid growth of magnesium and magnesium alloy connection problems aroused people's great attention, but the welding performance of magnesium alloy is not well, it is difficult to achieve a reliable connection and become the bottleneck that restrict the application of magnesium alloys technology and become the key technology of presses for solution.

In recent years, some researchers studied on ammonia arc welding (TIG, MIG), electron beam welding (EBW) (LBW), laser welding and friction stir welding (FSW) of magnesium（magnesium alloy）and aluminum alloy, but there are still many malpractices because the low melting point of magnesium, linear expansion coefficient and thermal conductivity, so that easy to generate the brittle intermetallic compounds, cracks and porosity in the welding process [8-10]. There is a wide joint and easy to deformity after welding defects in the heat affected zone. So through the study for Mg and Al dissimilar metals, the law of the Mg/Al dissimilar metal weld formation was researched, it was realized that the connection of dissimilar metals was reliably, it has important social and economic benefits to expand the application of magnesium alloy structural materials [11].

1.2 The development and application of magnesium alloy

1.2.1 The development status of magnesium alloy

With the development of science and technology, the consumption of metal materials had raised sharply, the current commonly resources on the earth has been affected [12]. The material of the new century mainly include that rich resources, energy conservation and environmental protection, in which light weight and high strength material conformed to the material requirements of the new century, development of Mg alloy is one of the most promising green new structural materials [13-16]. Mg in sea water accounts was about the earth's crust of 2.3% and reserves was bout 2.1×10^{15}t, which have significant reserves of Mg in salt lake.

Main research and development of Mg, plasticity and toughness of the material in surrounding, corrosion resistance and fatigue resistance and so on comprehensive performance were developed; new type of Mg alloy can be prepared through adoption of new alloy elements and new corrosion process [17-20]. Development important equipment is suitable for mass production of Mg alloy; in which the development of new type high performance Mg alloy system; the atmosphere of Mg alloy smelting process protection, the flame retardant Mg alloy technology and surface treatment technology, and the problem of Mg alloy with the welding of dissimilar materials had been concerned in varieties fields.

Mg - Al - Mg, Mg - Al - Mn, Mg - Al - Si and Mg - Al - Re system had been developed in order to meet the mechanical requirements on the properties of Mg alloy structure industry, some new type of Mg alloy had been widely applied, such as electronic communication products, lightweight, high strength, corrosion resistance of Mg - Li alloy and Mg - Re alloys and high temperature were used in the field of aerospace Mg alloy. The technology of flame

retardant Mg alloy appeared as Mg alloy prepared technology was further improved; at the same time, Mg alloy melt environmental protection technology and Mg alloy micro-arc oxidation surface treatment technology emerged [21]. This phenomenon significantly promoted the applications of Mg alloy in automotive, aerospace and other fields.

1.2.2 The application of magnesium alloy

Mg alloy compared to other commonly materials of physical and mechanical properties are shown in table 1.1. Mg alloy has the outstanding performance characteristics to make its application prospect become more widely [22]. Mg alloy gradually replaces various structure steels, Al alloy and other material had been widely used in automobiles, electronics, communications and other civilian areas.

Table 1.1 Performance comparisons for several materials.

Alloy	Density /g·cm-3	Melting point /°C	Heat conductivity /W·m-1·K-1	Tensile strength /MPa	Yield strength /MPa	Elongation /%	Specific strength /GPa	Young modulus /GPa
Mg AZ91	1.82	596	72	280	160	8	154	45
Mg AM60	1.79	615	62	270	140	15	151	45
Al 380	2.7	595	100	315	160	3	117	71
Steel	7.86	1520	42	517	400	22	66	200
ABS	1.03	90	0.2	35	---	40	34	2.1
PC	1.23	160	0.2	104	---	3	85	6.7

Mg alloy is applied in the car industry to meet the requirements of automotive safety, energy saving and environmental protection, the auto lightweight goals was effectively realized [23-28]. Car designer and production enterprises were achieved in recent years in order to reduce vehicle emissions pollution, improve fuel efficiency and reduce CO_2 emissions; it was found that the Mg alloy parts can significantly reduce vehicle weight, fuel consumption and the emissions of our fleet. The second generation of magnesium wheel yet only 514 kg decreased by 28% than the weight of aluminum wheel. For a car, 10% reduction in weight and fuel quantity can be reduced by 6% - 8%. The large-scale application of Mg alloy in the car production has more than 60 kinds of parts [29, 30]. The application of Mg alloys as components in the car as shown in figure 1.1.
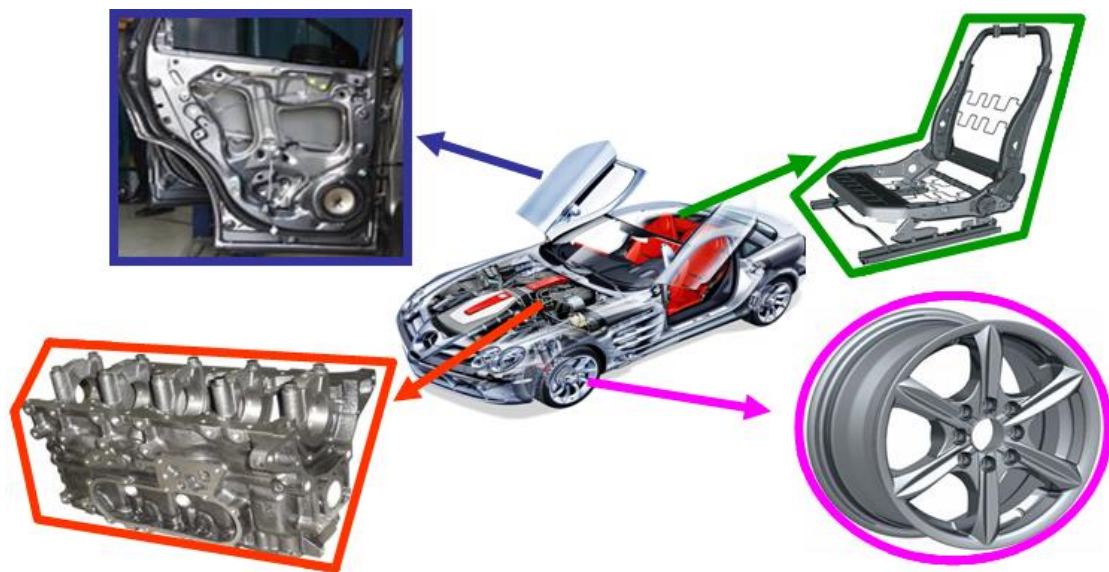
Fig. 1.1 Application of Mg alloys as components in the car.

In the field of electronics and communication, Mg alloy also got people greatly concern, such as TV, computer, monitor, camera shell are using plastic, these products will produce a large amount of waste pollution materials [31]. Mg alloy as an alternative can effectively reduce the pollution. In present, there are some products has been developed, but is still in the stage of research and

development.

Mg alloy in cutting-edge fields such as aerospace, military defense received great attention [32]. Mg alloy as a structural material has the advantages of satisfying the demands of the development of today's airframe structure materials in aircraft engine, aircraft, missile skin, the external hull and landing gear, in which satellite and the rocket shell adopts various kinds of casting and the deformation of magnesium alloys. Mg alloy as a structure not only can reduce weight, also can greatly reduce costs, such as satellite reduce 1 kg each, rocket can reduce 500 kg and save $10 million [33]. Mg alloy as lightweight metal structure material in realizing, the light weapons and equipment improved the tactical weapons each phase performance to play an important role. For example, a larger number of vehicles, aluminum alloy parts, engineering plastics, missiles and artillery, the photoelectric instrument and military equipment made relevant Mg alloy parts and was completely feasible in technology [34]. With the constant improvement of the Mg alloy preparation and processing technology of Mg alloy, which more widely applied in various industries in the future and provided important resources guarantee for sustainable development strategy.

1.3 Magnesium alloy welding research status

Welding and joining of magnesium alloys exert a profound effect on magnesium application expansion, especially in ground and air transportations where large-size, complex components are required. This applies to joints between different grades of cast and wrought magnesium alloys for dissimilar joints with other materials [35].

Due to specific physical properties of magnesium, the welding requires low and well controlled power input. Moreover, very high affinity of magnesium alloys to oxygen requires shielding gases which protect the liquid weld from an environment [36]. To magnify complexity, solid state reaction with oxygen forms a thermodynamically stable natural oxide layer on magnesium surface; the phenomenon is an inherent deficiency of joining. Both the conventional and novel welding techniques were adapted to satisfy these requirements, it is including that arc welding, resistance spot welding, electromagnetic welding, friction stir welding, electron beam and laser welding [37]. Since fusion welding has a tendency to generate porosities and part distortion, many alternative joining practices were implemented. These included that soldering, brazing, adhesive bonding and mechanical fastening [38]. However, the latter techniques have also disadvantages associated. For example, with stress induced by drilling holes during mechanical fastening, preheating during clinching or extensive surface was conducted in adhesive bonding [39]. Hence, experiments are progress with completely novel ideas of magnesium joining [40].

An application of magnesium is often multi-material structures, requiring dissimilar joints, involving magnesium alloys as one side; there are alloys with drastically different properties. How to weld dissimilar materials is one of the most difficult problems in welding. A difference in physicochemical properties of dissimilar joint components creates challenges for mechanically bolted

assemblies as well [41].

So far, the melting magnesium aluminum soldering welding in electron beam welding, magnetic pulse welding and resistance spot welding, TIG welding, MIG welding, laser welding, laser and electric arc welding, etc., the solid-state welding explosion welding, the common friction welding, friction stir welding, vacuum diffusion welding and brazing [42-48]. Domestic and foreign researches used generally magnesium alloy and aluminum alloy friction stir welding to made a certain progress. Now above research status of magnesium alloy and aluminum alloy welding points are as following:

1.3.1 Arc welding

There are two basic methods of arc welding. In an inert gas tungsten arc welding (TIG), an arc is generated between a non-consumable tungsten electrode and the welded metal. The electrode and welded metal are shielded with an inert gas. In general, welding can be made with or without filler. In this case, the filler is used and there is a form of wire in order to conduct the welding. For magnesium alloys, filler rods may be the same chemistry as welded part or lower melting range [49]. The latter allows the weld to remain liquid until other parts of the weld are solid, thus reducing the probability of cracking. During an inert gas metal arc welding (MIG), the arc is formed between the consumable electrode and the part to be welded [50]. The electrode is continuously provided from the spool. Both the welded area and the arc zone are protected by a gas shield.

The specific heat of magnesium is around 1 $Jg^{-1}°C^{-1}$ but due to lower density of magnesium, its heat capacity is lower than aluminum or steel in table 2. Due to similar melting ranges of Mg and Al alloys and the lower latent heat of fusion of magnesium alloys the heat required to melt magnesium is two third of that required for melting the same volume of aluminum alloys [51]. Relatively high coefficient of thermal expansion of magnesium alloys of 26 μm

8

m^{-1}°C^{-1} and high thermal conductivity of 51 Wm^{-3}K^{-1} make it susceptible to distortion during welding.

Table 2 Selected properties of AZ91 magnesium alloy, A6061 aluminum alloy, ZA12 zinc alloy and AISI 304 stainless steel.

Property	Units	AZ91	A6061	ZA12	Steel304
Melting range	°C	470-595	582-652	377-432	1400-1455
Density	g cm^{-3}	1.8	2.7	6.0	8.0
Modulus of elasticity	GPa	45	68.9	83	200
Thermal conductivity (20°C)	Wm^{-3}K^{-1}	51	180	116	16.2
Coefficient of thermal expansion (20-100°C)	μm m^{-1}°C^{-1}	26.0	23.6	24.1	17.2
Specific heat （20°C）	Jg^{-1}°C^{-1}	0.8	0.896	0.450	0.5
Latent heat of fusion pure base metals	J/g	368	398	272	113
Electrical resistivity	μΩm	0.0000143	0.00000360	0.00000610	0.0000720

For transition metal alloys, a technique exists of flux-assisted gas tungsten

arc welding (FATIG) when the welding path is coated with chemical fluxes [52]. In general, fluxes allow full penetration welding at greater rates using relatively inexpensive gas tungsten arc as the heat source. Using argon shielding and chloride fluxes, magnesium alloy welding tests showed an increasing in weld penetration as much as one hundred percent [53]. The deeper weld penetration was accompanied by higher heat input. Among several chlorides, including LiCl, $CaCl_2$, $CdCl_2$, $PbCl_2$ and $CeCl_3$, cadmium chloride was the most effectively. Images of arc area during welding revealed that the heat flux from the arc appeared more concentrated towards the center of the pool with chloride additions.

The solidification microstructure of the weld is controlled depending on the thermal gradient and growth rate under cooling, [54]. The microstructure of MIG welded AZ91D alloy with AZ61 as welding wire were consisted of solid solution of α-Mg and intermetallic compound of $Mg_{17}Al_{12}$ [55]. The weld contained roughly 7% of Al. In HAZ near the fusion line, subjected to temperatures between solidus and liquids, a part of α-Mg solid solution and eutectics distributed at grain boundaries and experienced melting. Thus, after subsequent solidification, the boundary regions formed islands of eutectic solid solution of α-Mg surrounded by $Mg_{17}Al_{12}$ precipitates [56]. The chloride fluxes during welding using FA-TIG technique affected the weld microstructure. It appears that alloying from fluxes did not drastically affect on the solute partitioning during solidification. The AZ21 fusion zone, obtained with cadmium chloride fluxes, was significantly more dendrite than the zone of the alloy identically welded without fluxes. It is believed that differences in microstructure between welds with and without chloride fluxes are caused by thermal gradient [57-60]. During welding with cadmium chloride, the arc temperature was significantly higher and the liquid weld experienced higher constitutional under cooling.

In addition to extensive porosity, hot cracking is considered the major problem of magnesium welding. This is especially true for a repair practice

where thick plates are welded using the metal inert gas technique. During MIG welding of 10 mm thick plates of AZ91D, two types of hot cracking occurred: solidification cracking of weld and liquation cracking in HAZ [61]. In general, solidification cracking takes place within a specific temperature range when a liquid film appears between dendrites. Solidification cracking occurred within the crater at the weld end and was caused by the high segregation of Mn, Al and Zn accompanied by high tensile stress. A frequency of both types of cracks increased at low welding speeds and was associated with high heat input and tensile stress. The experimental observations indicate that for MIG welding of magnesium alloys a reduction in the heat input reduces the frequency of cracks in weld and HAZ.

1.3.2 Laser beam welding

The term laser is an acronym for light Amplification by Stimulated Emission of Radiation. The solid or gaseous media are stimulated to emit a monochromatic, coherent source of light focused source and delivered to the workplace [62]. A delivery by hard optics explores mirrors and lenses for laser deflection and focusing. A limitation of hard optics is the short distance between the laser source and welded part. The use of fiber optics cable allows a longer separation of laser source. The latter is also more suitable for manipulation by robotics [63]. There are two major types of lasers, commonly used in industrial applications. The laser of Neodymium-doped Yttrium-Aluminum-Garnet explores a crystalline rod in the ultraviolet range with a wavelength of 1.06 μm. The CO_2 laser is based on gaseous media and has a wavelength of 10.6 μm.

During the welding laser fires, many pulses per second as shown in Fig. 1.2, the light is absorbed by the metal, so that causing the keyhole effect because the beam drills, melts and vaporizes some metal volume. When the pulse ends, the molten metal around the keyhole flows back after solidification forms a spot

weld. A shielding gas is used to protect the molten metal [64]. Welding may be created with or without a filler metal. As major benefits of laser beam welding, there are quoted: high travel speeds, minimal amount of heat added during welding, resulting in a small heat affected zone, low part distortion, no slag or spatter and great flexibility in tooling design.
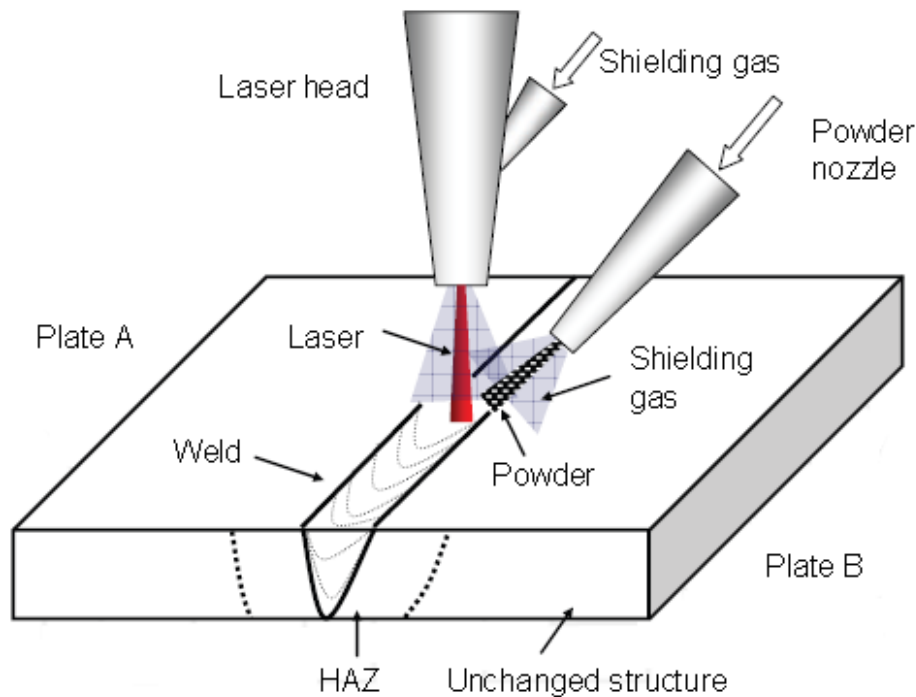
Fig.1.2. Schematic of laser beam welding process.

The AM60 alloy, welding with a continuous wave CO_2 laser formed a weld with the narrow heat affected zone and no obvious grain coarsening [65]. The fusion zone was fine-grained with high density of $Mg_{17}Al_{12}$ precipitates. The redistribution of elements occurred during welding with lower Mg and higher Al content in weld than that in the base alloy. A hardness of the fusion zone reached the higher level than the base alloy.

The mechanism of porosity during continuous-wave Nd-YAG laser beam welding of AM60B cast alloy revealed a significant increase in fusion-zone porosity for most of welding conditions. The pre-existing pores, coalescence and expansion were seen as the cause of porosity increase. The keyhole was

found more stable compared to welding of Al alloys, but its stability did not substantially affect the overall porosity. During CO_2 laser welding of AZ31 wrought alloy, pores were found in welds mainly around the fusion boundary [66]. For wrought alloy, the level of initial porosity is relatively low; pore formation during welding is attributed to the surface contamination and hydrogen rejection from the solid phase during solidification. It appears that porosity is created due to a collapse of the keyhole and turbulent flow in the weld.

In recent, an analytical thermal model for welding the magnesium alloy WE43 was developed. Since laser welding is controlled by many parameters including that power, beam characteristics, welding speed, focal position, gas flow and material characteristics, the optimum is a complex task. The model allows determining the penetration depth and the bead width as a function of both the incident laser power and the welding speed. Modeling along with experimental verification was also used to study the keyhole formation and the geometry of weld profiles during welding of ZE41A-T5 alloy with Nd-YAG laser. Generally, the weld width and fusion area decrease with increasing welding speed [67]. It was found that the excessive reduction in laser power resulted in lower surface power density and change of the welding mode through partially penetrated keyhole to the conduction mode. There was no significant effect of the filler wire feed rate on the coupling and melting efficiency.

Hybrid laser beam technologies are defined as a combination of a laser beam source with an additional secondary beam source or another joining technique. A hybrid laser-TIG welding (LATIG) of AZ31 alloy achieved higher welding speed compared to that in laser or TIG welding. The penetration depth was twice for TIG and four times for laser welding. The same combination of laser beam and TIG was used to weld AZ31B magnesium alloy with mild steel by applying a nickel interlayer. As a result, semi metallurgical bonding was achieved. Along the Mg – Ni interlayer, the Mg_2Ni phase with solid solution of Ni in Fe formed. However, at the interface of molten pool and steel, the fusion

zone did not interact with solid solution, it is the mechanical bonding.

A new method of hybrid joining, called laser continuous weld bonding, was developed as an alternative to laser welding and adhesive bonding. The technique was successful in joining of AZ31B magnesium and A6061 aluminum alloys by reducing a volume of brittle intermetallic compounds of Al_3Mg_2 and $Mg_{17}Al_{12}$ phases which are formed in the fusion zone by reducing the joint strength. The intermetallic phase formation was reduced because the fluid generated by the gasification of adhesives. It appears that the rising of adhesive vapor slows down the downward movement of liquid Mg, so that the content was reduced in the weld. Hence, the weld is composed of two-phase mixture with less intermetallic compound and more solid solution.

1.3.3 Friction stir welding

Friction stir welding is a relatively new joining technique and was invented in 1991 by the welding institute, England (TWI). It uses a rotating, non-consumable and cylindrical shouldered tool to deform the surrounding material without melting [68]. Thus, the joint is essentially formed in a solid state. Due to frictional contact of the tool and welded parts, the heat generated plasticize metal. As the tool moves forward, its special profile forces plasticized material to the back and the joint is formed because substantial forging force consolidates material. The process is accompanied by severe plastic deformation which involving dynamic recrystallization of the base metal.

There are many benefits associated with friction stir welding. A low heat input and bonding below the melting point result in higher joint properties and lower distortion. The severe plastic deformation was introduced by the tool action to generate the fine-grained microstructure [69]. The process is energy efficient and environmentally friendly with no fumes or UV radiation. Since there is no weld gravity issue, various welding positions are possible as orbital, vertical or overhead. As likely drawbacks of friction stir welding, the large force

and system stiffness requirements are quoted. Another drawback was a fixed pin capable handling of only one material thickness. However, modern solutions offer pins which can retract or expand within material, so that causing welding components with varying thickness.

The total energy generated per unit length of the weld E equals the energy because friction between the tool and the work piece Ef and the energy generated due to the plastic deformation of the work piece Ep:

$$E = E_f + sE_p \tag{1-1}$$

Where: s is the scaling factor introduced in order to control the effect of the energy from plastic deformation. The friction component Ef is expressed by:

$$E_f = 2\mu F\left(\frac{1}{3}r_0 + \frac{r_i^2}{r_0^2}h\right)\frac{\omega}{\upsilon_0} \tag{1-2}$$

r_o is the radius of the shoulder, r_i is the radius of the pin, h is the height of the pin, ω is the pin angular speed, μ is the friction coefficient, F is the compressive force.

The development of weld microstructure is controlled by shear deformation and thermal effects. In weld of wrought AZ61 alloy, the crystallographic texture develops with a strong concentration of {0001} basal planes being heterogeneously distributed in stir zone [70]. It was suggested that texture develops because shear deformation was caused by the rotating pin. Deformation of magnesium with hexagonal close packed structure is controlled by a slip along {0001} basal plane. Therefore, formation of the texture during welding affects the mechanical properties of weld. During friction stir welding of two AZ61 plates with a thickness of 6.3 mm both the transition and stir regions developed similar grain size, much finer than in the base alloy.

The technique of friction stir welding was applied to join magnesium with steel. During welding of AZ31 alloy and stainless steel 400, the rotation speed and pin axis orientation affected the microstructure and strength of the joint. The maximum strength of a butt type joint achieved approximately 70% of the strength measured for pure magnesium. The effect of tool geometry on microstructure and mechanical properties of Mg-steel welding was also studied. For brushed finished steel joints, the strength increased significantly with the probe length. Also microstructure was found to be sensitive to the probe length. The longer probe resulted in diffusion bonding while the shorter probe provided only the mechanical bond. The different observations were recorded for zinc coated steel where the probe length did not improve the joint strength. In that case, the short probe contributed to the defect-free joint.

1.3.4. Electromagnetic welding

Electromagnetic welding explores a phenomenon that current carrying conductors exert a force on each other as shown in Fig. 1.3. The force depends on the current direction and is repulsive for opposite direction flow and attractive for the same flow direction. In practice, the electric current in the coil creates an eddy current within the work piece which generates forces between the coil and the material placed within it [71]. During the welding process, these forces cause the outer work piece to plastically deform after accelerating towards the inner work piece, thus, a solid state weld was achieved. There are several modifications of magnetic welding which were successfully applied for magnesium. Similar concept of electromagnetic compression forming was used for processing of hollow profiles of magnesium alloys.

Magnetic pulse welding is a solid state joining process and has a modification called pressure seam welding [72]. Very high currents are generated by discharging a set of charged capacitors rapidly through the coil

which surrounds the component to be welded. The eddy currents oppose the magnetic field in the coil and a repulsive force is created which drives the parts together at very high force speed and creates an explosive or impact type of weld. The eddy current i is expressed by the following equation:

$$\nabla \times i = -\kappa \left(\frac{\partial B}{\partial t} \right)$$ (1-4)

Where: κ and B are electrical conductivity and magnetic flux density, respectively.
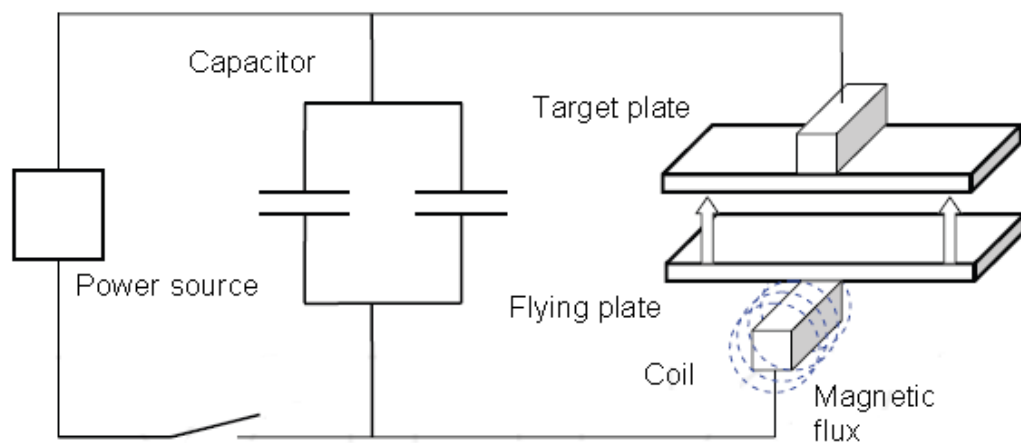
Fig.1.3 Schematic diagram of electromagnetic pulse welding.

Where: Bo_2 and Bi_2 are magnetic flux densities at lower and upper surfaces of welded sheet, μ is magnetic permeability, δ is the depth skin effect, given by the following:

$$\delta = \sqrt{2 / \omega \kappa \mu}$$ (1-5)

Where: ω is the angular frequency of changing field.

The technique provided satisfactory results for Al- AZ91 magnesium alloy.

The sheets with a thickness of 0.5 to 1 mm were seam welded to produce a weld having the width of 5 mm. The weld thickness was 10% less than the original sheet thickness. It is believed that the weld zone is formed as a combined effect of heating by eddy currents and the strong impulse electromagnetic force (magnetic pressure). No clear fusion boundary in the joint interface was microscopically detected. The transition layer had the characteristic wavy shape without any significant heat affected zone.

The same concept called electromagnetic impact welding was used for 0.6 mm sheet of AZ31 magnesium alloy and 1 mm thick A3003 aluminum alloy. The differences in electrical conductivities of Al and Mg led to the skin depth of 0.7 mm in Al and 0.6 mm in Mg alloys [72]. The weld microscopy revealed a wavy interface and complete metal continuity without weld defects. Both x-ray diffraction and electron microscopy did not detect the intermetallic phase at the interface, it result showed a lack of melting. When welding was conducted at optimum conditions, failure during tensile testing occurred beyond the weld in the base metal.

The electromagnetic compression of tubular profiles with high electrical conductivity is an innovative joining process for lightweight materials [73]. The components are joined by using pulsed magnetic fields which apply radial pressures of up to 200 MPa. Since there is no contact between components to be joined, there is not possible to cause damage of the welded parts. The method was tested for aluminum alloys and has potentials for magnesium.

1.3.5 Diffusion bonding

Diffusion bonding represents a solid state joining where two materials are brought into close contact at elevated temperatures of less than 0.7 Tm under moderate pressure, thus the atomic migration is not accompanied by macro-deformation [74]. Since temperature does not exceed melting, it allows to eliminate many problems associated with fusion welding. The process is

typically conducted in a press; the heating was through conventional methods or induction units. Microwave sources are also explored for this purpose. To obtain high bonding, the surface should be clean and flat. There are three major stages of the bonding progress. First, a contact between materials occurs through the mating surfaces. During the second stage, diffusion within grain boundaries predominate eliminated pores and ensured arrangements of grain boundaries. During the third stage, the volume diffusion dominates and process was completed.

Diffusion bonding was found applicable for pure magnesium and its alloys. For pure magnesium rolled sheet, tests were carried out at the pressure range of 2-20 MPa, temperature range from 300°C to 400°C and time periods up to 72 h. The maximum lap shear strength was 0.888 at a bonding pressure of 20 MPa, temperature 400°C and for time of 1 h. A ductile fracture was revealed after the compression lap shear test [75].

During manufacturing of complex sheet structures, diffusion bonding is often combined with super plastic forming. The combination allows reducing weight and fabrication cost, when compared with mechanically fastened structures. The technology was successfully implemented for super plastic magnesium alloy AZ31 with a grain size of approximately 17 μm. The maximum of lap shear strength was 0.85 at a bonding pressure of 3 MPa and a bonding temperature of 400°C and time of 3 h. No bond line was revealed during microscopic observations indicating the extensive diffusion [76]. A successful diffusion bonding was also achieved for a super plastic alloy AZ31 hot rolled at 250°C. Having a grain size of 8.5 μm, the alloy behaved in a super plastic manner within the temperature range of 250-300°C. The diffusion bonding and super plasticity are grain size dependent, thus structures with finer grains will have lower bonding temperature. The effect is related to the bonding mechanism where diffusion controls the joint formation. The numerous voids, initially present at the interface between joined metals will disappear because the plastic flow and diffusion towards the void surface. For

finer grains the boundary diffusion has the higher contribution because more grain boundaries intersect with voids [77].

For dissimilar joints of Mg alloys, special importance is Al. the reason is the substitution of Al with Mg in automotive industry, which requires Mg-Al joints. An example is the Mg/Al joint was conducted under vacuum bonding at 460-480°C, time of 40-60 min and a pressure of 0.08-0.10 MPa. Hence, the diffusion zone was formed with two different transition regions on both sides. At the interface with Al, various Mg_xAl_y phases, such as Mg_2Al_3 and $Mg_{17}Al_{12}$ were formed. On the Mg side, Mg_2Al_3 phase was formed. The latter has fcc structure as opposed to hcp of magnesium. It is claimed that Mg_2Al_3 phase has the positive effect on cracking resistance of the joint.

The major obstacle during welding of Mg and Al is a formation at the interface between both alloys brittle compounds of Mg-Al, so that causing cracking during service [78]. Thus eliminating or improving interlayer is the critical factor in producing strong joints. One of possible solutions is to introduce an interlayer between Al and Mg for AZ31B and A6061 alloys, Zn interlayer was found to be effective. The Zn layer with a thickness of 60 μm was deposited on Al surface by hot dipping. The bonding was conducted at 360°C for 3 s.

Diffusion bonding was proved effectively for joining Mg with alloys having substantially higher melting ranges, such as Cu alloys. Joints made at the bonding temperature of 450°C, pressure of 12 MPa and time of 30 min exhibited shear strength of 66 MPa and bonding strength of 81 MPa [79].

The new technique of in-situ joint formation of magnesium cast and wrought components without necessity of welding was proposed at recently. The focus of this technique is to eliminate the natural oxide layer presented on magnesium and to replace it with metallic $Zn/MgZn_2$ layer by a sequence of chemical, electrochemical and heat treatments. The objective is to change the surface reactivity and increase surface wet ability, so that creating Mg-Mg compound [80]. The process verification performed on AZ31 substrate joined

with AJ62 cast alloy and pure Mg, an area-wide metallurgic in nature and defect free interface between both couples were revealed. The coating material dissolved into the bulk metal during casting. The issue of formation of shrinkage cavities at the interface can be solved by selecting appropriate solidification intervals.

1.4 Application prospect of this topic

According to micro structure and elemental diffusion for Mg/Al dissimilar metals on welding interface, the internal contact of Mg/Al metals welding craft and joint performance was revealed. The main experiment and theoretical basis was provided for the development of Mg/Al dissimilar metals basic craft. Whose metal structure has importance theoretical significance and practical value on automotive, aerospace, the application in the field of defense.

1.5 Summary

During last decade, a substantial progress was made in welding and joining of magnesium alloys. In addition to improvement in conventional fusion welding techniques, novel methods and their hybrids were developed. They allow producing commercially viable joints of different grades of cast and wrought magnesium alloys. Although there is a substantial progress on fusion welding, its application to dissimilar joints involved a number of materials with drastically different properties, but it is still limited. Also, alternative joining technologies which require local deformation are not fully successful because limited formability of magnesium. Novel ideas aimed to eliminate the detrimental effect of natural oxides on magnesium surface seemed to represent a step in correct direction. They may require complex surface engineering solutions but preliminary tests are promising. Therefore, there is a search for alternative methods of joining magnesium alloys. Especially, the dissimilar alloys attracted widely attention.

References

[1] K. Abderrazak, W. Salem, H. Mhiri, G. Lapalec, M. Autric. Modeling of CeO_2 laser welding of magnesium alloys, Optics and Laser Technology, 2008, **40**, 581-588.

[2] T. Aizawa, M. Kashani, K. Okagawa. Application of magnetic pulse welding for aluminum alloys and SPCC steel sheet joints, Welding Research, 2007, **86**, 119-124.

[3] H. Al-Kazzaz, M. Medraj, X. Cao, M. Jahazi. Nd:YAG laser welding of aerospace grade ZE41A magnesium alloy: Modeling and experimental investigations, Materials Chemistry and Physics, 2007, **109**, 61-76.

[4] P. Barreiro, V. Schulze. D. Loehe. Influence of process parameters on structure and mechanical properties of joints produced by electromagnetic forming and friction stir welding, Advanced Materials Research, 2008, **43**, 47-56.

[5] W. Cai, P. Wang, W. Yang. Assembly dimensional prediction for selfpiercing riveted aluminum panenls, Inter. Journal of Machine Tools Manufacturing, 2005, **45**, 695-704.

[6] Y. Chen, K. Nakata. Effect of tool geometry on microstructure and mechanical properties of friction stir lap welded magnesium alloy and steel, Materials and Design, 2009, **30**, 3913-3919.

[7] C. Chi, C, Chao, T. Liu, C. Wang. Relational analysis between parameters and defects for electron beam welding of AZ-series of magnesium alloys, Vacuum, 2008, **82**, 1177-1182.

[8] C. Chi, C. Chao. Characterization on electron beam welds and parameters for AZ31B-F extrusive plates, Journal of Materials Processing Technology, 2007, **182**, 369-373.

[9] M. Elthalabawy, I. Khan. Microstructural development of diffusion brazedaustenitic stainless steel to magnesium using nickel interlayer,

Materials Characterization, 2007, **61**, 703-712.

[10] A. Emam, E. Domiaty. A refined energy-based model for friction-stir welding, World Academy of Science, Engineering and Technology, 2009, **53**, 1016-1022.

[11] J. Gilmore, V. Dunfold, G. Parteidge. Journal of Materials Science, 1991, **26**, 3119-3124.

[12] G. Humpston, M. Jacobson. Principles of Soldering, ASM International, Materials Park, Ohio.

[13] F. Islam, M. Medraj. The phase equilibria in the Mg-Ni-Ca system, Calphad, 2005, **29**, 289-302.

[14] J. Jia, A. Atrens, G. Song, T. Muster. Simulation of galvanic corrosion of magnesium coupled to a steel fastener in NaCl solutiion, Materials and Corrosion, 2005, **56**, 468-474.

[15] R. Johnson, P. Threadgill. Friction stir welding of magnesium alloys, Magnesium Technology, 2003, **23**, 190-198.

[16] S. Kore, J. Imbert, M. Worswick, Y. Zhou. Electromagnetic impact welding of Mg to Al sheets, Science and Technology of Welding and Joining, 2009, **14**, 549-553.

[17] N. Kumbhar, K. Bhanumurthy. Friction stir welding of Al6061 alloy, Asian Journal of Experimental Science, 2008, **22**, 63-74.

[18] K. Lee, S. Kumai, T. Arai, T. Aizawa. Interfacial microstructure and strength of steel/aluminum alloy lap joint fabricated by magnetic pressure seam welding, Materials Science and Engineering A, 2007, **471**, 95-101.

[19] Y. Li, P. Liu, J. Wang, H. Ma. XRD and SEM analysis near the diffusion bonding interface of Mg/Al dissimilar materials, Vacuum, 2008, **82**, 15-19.

[20] L. Liu, J. Tan, X. Liu. Reactive brazing of Al alloy to Mg alloy using zinc-based brazing alloy, Materials Letters, 2007, **61**, 2373-2377.

[21] L. Liu, J. Wang, G. Song. Hybrid laser-TIG welding, laser beam welding and gas tungsted arc welding of AZ31B magnesium alloy, Materials Science and Engineering A, 2004, **381**, 129-133.

[22] L. Liu, L. Xie. Adhesive bonding between Mg alloys and polypropylene, Materials Technology: Advanced Performance Materials, 2007, **22**, 76-80.

[23] L. Liu, J. Tan, L. Zhao, X. Liu. The relationship between microstructure and properties of Mg/Al brazed joints using Zn filler metal, Materials Characterization, 2008, **59**, 479-483.

[24] L. Liu, H. Wang, Z. Zhang. The analysis of laser welds bonding of Al alloy to Mg alloy, Scripta Materially, 2007, **56**, 473-476.

[25] L. Liu, Z. Wu. Microstructure and interfacial reactions of soldering magnesium alloy AZ31B, Materials Characterization, 2010, **61**,13-18.

[26] Y. Luo, G. You, H. Ye, J. Liu. Simulation on welding thermal effect of AZ61 magnesium alloy based on three-dimensional modeling of vacuum electron beam welding heat source, Vacuum, 2010, **84**, 890-895.

[27] L. Ma, D. He, X. Li, J. Jiang. High frequency soldering of magnesium alloy AZ31B using Zn-Al filler metal, Materials Letters, 2010, **64**, 596-598.

[28] G. Mahendran, V. Balasuramanian, T. Senthilvelan. Influence of diffusion bonding process parameters on bond characteristics of Mg-Al, Transactions of Nonferrous Metals Society of China, 2010, **20**, 997-1005.

[29] M. Marya, G. Edwards. Chloride contribution in flux-assisted GTA welding of magnesium alloys, Welding Journal, 2002, **12**, 291-298.

[30] M. Marya, G. Edwards. The laser welding of magnesium alloy AZ91D, Welding World, 2000, **44**, 31-37.

[31] R. Neugbauer, C. Kraus, S. Dietrich. Advances in mechanical joining of magnesium, CIRP Annals - Manufacturing Technology, 2008, **57**, 283-286.

[32] K. Papis, J. Loffler, P. Uggowitzer. Interface formation between liquid and solid Mg alloys - An approach to continuously metallurgic joining of magnesium parts, Materials Science and Engineering A, 2010, **527**, 2274-2279.

[33] S. Park, Y. Sato, H. Kokawa. Metallurgical and Materials Transactions A, 2003, **34**, 987-996.

[34] S. Park, Y. Sato, H. Kokawa. Effect of micro-texture on fracture location in friction stir weld of Mg allloy AZ61 during tensile test, Scripta Materialia, 2003, **49**, 161-166.

[35] D. Poddar. Solid-state diffusion bonding of commercially pure titanium and precipitation hardening stainless steel, International Journal of Recent Trends in Engineering, 2009, **1**, 93-99.

[36] V. Psyk, C. Beerwald, A. Klaus, M. Kleiner. Characterization of extruded magnesium profiles for electromagnetic joining, Journal of Materials Processing Technology, 2006, **177**, 266-269.

[37] Y. Quan, Z. Chen, Z. Yu, X. Gong, M. Li. Characteristics of laser welded wrought Mg-Al-Mn alloy, Materials Characterization, 2008, **59**, 1799-1804.

[38] X. Qui, G. Song. Interfacial structure of the joints between magnesium alloy and mild steel with nickel as interlayer by hybrid laser-TIG welding, Materials and Design, 2010, **31**, 605-609.

[39] H. Shi, R. Qiu, J. Zhu, K. Zhang, H. Yu, G. Ding. Effects of welding parameters on the characterestics of magnesium alloy joint welded by resistance spot welding with cover plates, Materials and Design, 2010, **31**, 4853-4857.

[40] J. Skar, H. Gjestland, L. Oosterkamp, D. Albright. Friction stir welding of magnesium die castings, Magnesium Technology 2004, TMS, Warrendale.

[41] H. Somekawa, H. Hosokawa, H. Watanabe, K. Higashi. Experimental study of diffusion bonding in pure magnesium, Materials Transactions, 2001, **42**, 2075-2078.

[42] H. Somekawa, H. Hosokawa, H. Watanabe, K. Higashi. Diffusion bonding in superplastic magnesium alloys, Materials Science and Engineering A, 2003, **339**, 328-333.

[43] H. Somekawa, H. Watanabe, T. Mukai, K. Higashi. Low temperature diffusion bonding in a superplastic AZ31 magnesium alloy, Scripta Materialia, 2003, **48**, 1249-1254.

[44] D. Sun, B. Lang, D. Sun, J. Li. Microstructure and mechanical properties of resistance spot welded magnesium alloy joints, Materials Science and Engineering A, 2007, **460**, 494-498.

[45] D. Sun, D. Sun, X. Gu, Z. Xuan. Hot cracking of metal inert gas arc welded magnesium, ISIJ International, 2008, **49**, 270-274.

[46] X. Wang, K. Wang. Microstructure and properties of friction stir butt-welded AZ31 magnesium alloy, Materials Science and Engineering A, 2006, **431**, 114-117.

[47] T. Watanabe, K. Kagiya, W. Yanagisawa, H. Tanabe. Solid state welding of steel and magnesium alloy using a rotating pin, *Quart.* Journal of Japanese Welding Society, 2006, **24**, 108-123.

[48] K. Westphal, T. Mulherkar, W. Schneiding. Joining of magnesium components using Al fasteners, Light Metal Age, 2005, **4**, 2-3.

[49] J. Shang, K. Wang, Q. Zhou, D. Zhang, J. Huang, G. Li, Microstructure characteristics and mechanical properties of cold metal transfer welding Mg-Al dissimilar metals. Mater. Des. 2012, **34**, 559–565.

[50] J. Wang, J. Feng, Y. Wang. Microstructure of Al-Mg dissimilar weld made by cold metal transfer MIG welding. Mater. Sci. Tech. Lond. 2008, **24**, 827–831.

[51] I. Bhamji, M. Preuss, R. Moat, P. Threadgill, A. Addison. Linear friction welding of aluminium to magnesium. Sci. Technol. Weld. Join. 2012, **17**, 368–374.

[52] H. Zhang, J. Song. Microstructural evolution of aluminum magnesium lap joints welded using MIG process with zinc foil as an interlayer. Mater. Lett. 2011, **65**, 3292–3294.

[53] F. Scherm, J. Bezold, U. Glatzel. Laser welding of Mg alloy MgAl3Zn1 (AZ31) to Al alloy AlMg3 (AA5754) using ZnAl filler material. Sci. Technol. Weld. Join. 2012, **17**, 364–367.

[54] F. Liu, Z. Zhang, L. Liu. Microstructure evolution of Al/Mg butt joints welded by gas tungsten arc with Zn filler metal. Mater. Charact, 2012, **69**,

84–89.

[55] F. Liu, DRen, D.X.; Liu, L.M. Effect of Al foils interlayer on microstructures and mechanical properties of Mg-Al butt joints welded by gas tungsten arc welding filling with Zn filler metal. Mater. Des. 2013, **46**, 419–425.

[56] L. Liu, F. Liu, M. Zhu. Study on Mg/Al weld seam based on Zn-Mg-Al ternary alloy. Materials, 2014, **7**, 1173–1187.

[57] L. Liu, X. Liu, S. Liu. Microstructure of laser-TIG hybrid welds of dissimilar Mg alloy and Al alloy with Ce as interlayer. Scr. Mater. 2006, **55**, 383–386.

[58] F. Liu, H. Wang, L. Liu. Characterization of Mg/Al butt joints welded by gastungsten arc filling with Zn-29.5Al-0.5Ti filler metal. Mater. Charact, 2014, **90**, 1–6.

[59] L. Liu, F. Liu. Effect of Ce on microstructure and properties of Mg/Al butt joint welded by gas tungsten arc with Zn-30Al-xCe filler metal. Sci. Technol. Weld. Join, 2013, **18**, 414–420.

[60] L. Liu, L. Xiao, J. Feng, Y. Tian, S. Zhou, Y. Zhou. The mechanisms of resistance spot welding of magnesium to steel. Metall. Mater. Trans. A 2010, **41**, 2651–2661.

[61] G. Song, G. An, L. Liu. Effect of gradient thermal distribution on butt joining of magnesium alloy to steel with Cu-Zn alloy interlayer by hybrid laser–tungsten inert gas welding. Mater. Des, 2012, **35**, 323–329.

[62] M. Gao, Z. Wang, X. Li, X. Zeng. Laser keyhole welding of dissimilar Ti-6Al-4V titanium alloy to AZ31B magnesium alloy. Metall. Mater. Trans. A, 2012, **43**, 163–172.

[63] M. Aonuma, K. Nakata. Effect of calcium on intermetallic compound layer at interface of calcium added magnesium–aluminum alloy and titanium joint by friction stir welding. Mater. Sci. Eng. B, 2010, **173**, 135–138.

[64] P. Penner, L. Liu, A. Gerlich, Y, Zhou. Feasibility study of resistance spot welding of dissimilar Al-Mg combinations with Ni based interlayers. Sci. Technol. Weld. Join, 2013, **18**, 541–550.

[65] M. Ring, W. Dahl. Fatigue properties of laser-beam weldments on the high

strength steels. Steel Res, 1994, **65**, 505–510.

[66] M. Alam, Z. Barsoum, P. Jonsén, H. Gblad, A. Kaplan. The influence of surface geometry and topography on the fatigue cracking behaviour of laser hybrid welded eccentric fillet joints. Appl Surf Sci, 2010, **256**, 1936–1945.

[67] M. Alam, Z. Barsoum, P. Jonsén, H. Gblad, A. Kaplan. Fatigue behaviour study of laser hybrid welded eccentric fillet joints – Part II: State-of-the-art of fracture mechanics and fatigue analysis of welded joints. In: Proceedings of NOLAMP 12 conference, Copenhagen, Denmark; 2009.

[68] M. Alam, Z. Barsoum, P. Jonsén, H. Gblad, A. Kaplan. The effects of surface topography and lack of fusion on the fatigue strength of laser hybrid welds. In: Proceedings of ICALEO 28 conference, Orlando, Florida, USA; 2009.

[69] A. Hobbacher. Fatigue design of welded joints and components, IIW document XIII 2151-07/XV-1254-07.

[70] M. Alam, Z. Barsoum, P. Jonsén, H. Gblad, A. Kaplan. Geometrical aspects of the fatigue behaviour of laser hybrid fillet welds. In: Proceedings of fatigue design conference, Senlis, Paris, France; 2009.

[71] A. Kaplan, P. Norman, G. Wiklund. The bifurcation flow chart as a method for a generalised theory, applied to spatter defects during laser welding. In: Proc. 12th NOLAMP, Copenhague (DK), FORCE technology; 2009.

[72] M. Gao, S. Mei, X. Li, X. Zeng. Characterization and formation mechanism of laser-welded Mg and Al alloys using Ti interlayer. Scr. Mater, 2012, **67**, 193–196.

[73] X. Qi, L. Liu. Fusion welding of Fe-added lap joints between AZ31B magnesium alloy and 6061 aluminum alloy by hybrid laser–tungsten inert gas welding technique. Mater. Des. 2012, **33**, 436–443.

[74] S. Darwish, A. Ghanya. Critical assessment of weld-bonded technologies. J. Mater. Process. Technol, 2000, **105**, 221–229.

[75] F. Brennan, P. Peleties, A. Hellier. Predicting weld toe stress concentration

factors for T and skewed T-joint plate connections. Int J Fatigue, 2000, **22**, 573–584.

[76] H. Pang. Analysis of weld toe profiles and weld toe cracks. Int J Fatigue, 1993, **15**, 31–36.

[77] H. Pang. Analysis of weld toe radius effects on fatigue weld toe cracks. Int J Press Vessels Pip, 1994, **58**, 171–177.

[78] J. Ferreira, C. Branco. Influence of the radius of curvature at the weld toe in the fatigue strength of fillet weld joints. Int J Fatigue, 1989, **11**, 29–36.

[79] V. Caccese, P. Blomquist, K. Berube, S. Webber, N. Orozco. Effect of weld geometric profile on fatigue life of cruciform welds made by laser/GMAW processes. Mar Struct, 2006, **19**, 1–22.

[80] T. Nykanen, X. Li, T. Bjork, G. Marquis. A parametric fracture mechanics study of welded joints with toe cracks and lack of penetration. Eng Fract Mech, 2005; **72**:1580–609.

Chapter 2 Experimental Materials and Methods

2.1 Introduction

For different welding joint, dissimilar metals diffused joint had different interface transition zone with different organizational structure and performance [1]. The organizational structure directly affect the weight of diffused welding joint, the formation depend on element diffused distribution nearby diffused interface, in which the organizational performance was comprehensive reflection of microstructure in transition zone [2]. With popularize and application of electron microscopy and electron microprobe techniques, the study on organizational performance reacted diffusion nearby interface became more thorough [3].

The paper was to study Mg/Al alloy joint strength and diffused organizational performance under pressure. The first, universal tensile testing machine was used to detect strength and calculate maximum principal stress under pressure. Scanning electron microscopy (SEM) was adopted to observe cut fracture form and micro structure in diffused bonding zone. By electron microprobe (EPMA) and X-ray diffraction (XRD), the element distributed on fusion zone and micro phase structure were detected and analyzed and lay the importance foundation for the depth study and popularize about Mg/Al alloy diffused joint micro organizational structure.

2.2 Experimental base metal

The materials were cut off by the unit length of 15×50 mm, the section was machined from rolled plates of the 2 mm thick AZ31B magnesium and the 2 mm thick Al-6061 alloys. The machining size is shown in Fig.2.1; two kinds of superimposed and docking equipped method were adopted to conduct

diffused bonding. The chemical composition of base metal was shown in Table 2.1 and Table 2.2. The specimens were polished with the #600 and #1200 sandpaper. In removing impurities process, the polished material was placed in the mixture of ethanol and acetone (the mixing ratio = 1:1) and kept 3min in the ultrasonic cleaner. Then the specimens were desiccated after being cleaned with water.

Table 2.1 Components of MgAZ31 alloy (wt. %).

Al	Zn	Mn	Ca	Si	Cu	Ni	Fe	Mg
2.5-3.5	0.5-1.5	0.2-0.5	0.04	0.1	0.05	0.005	0.005	Bal.

Table 2.2 Components of Al6061 alloy (wt. %).

Mg	Zn	Mn	Si	Cu	Fe	Ti	Cr	Al
0.9678	0.0005	0.0038	0.5527	0.2175	0.1401	0.0127	0.0718	Bal.

(a) Superimposed equipped mode

(b) Docking equipped mode
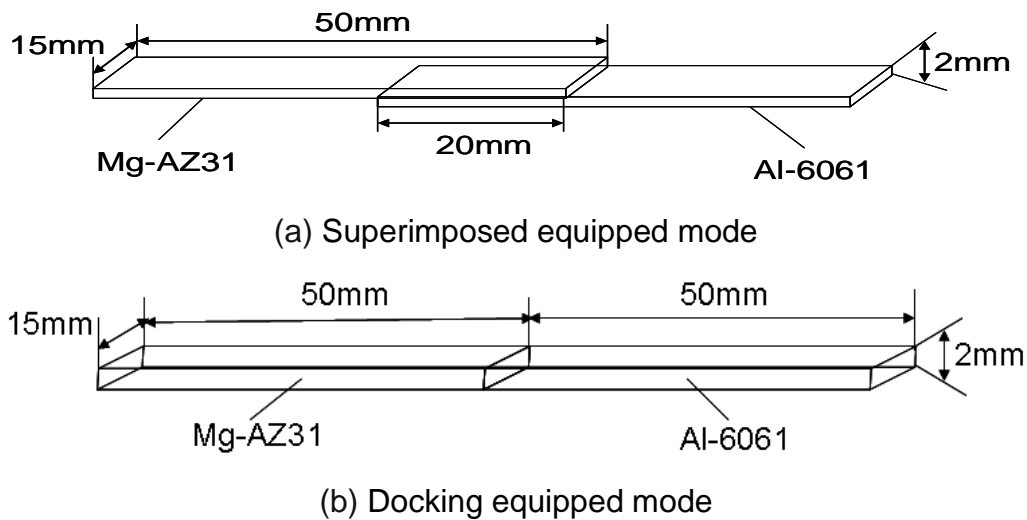
Fig.2.1 Sample processing size chart.

Magnesium alloys are mixtures of magnesium with other metals, including aluminum, manganese, silicon, copper, rare earths and zirconium. Magnesium is the lightest structural metal. Physical and chemical performance of Mg as shown in table2.1, Mg was hexagonal close-packed structure and no

allotrope change. The crystal structure is shown in Fig.2.2. Magnesium alloys have a hexagonal lattice structure, which affects the fundamental properties of these alloys. Plastic deformation of the hexagonal lattice is more complicated than in cubic latticed metals like aluminum, copper and steel [4]. Therefore magnesium alloys are typically used as cast alloys, but research of wrought alloys has been more extensive since 2003. Cast magnesium alloys are used for many components of modern cars, and magnesium block engines have been used in some high-performance vehicles; die-cast magnesium is also used for camera bodies and components in lenses.

Crystal structure image of Mg   Crystal structure image of Al
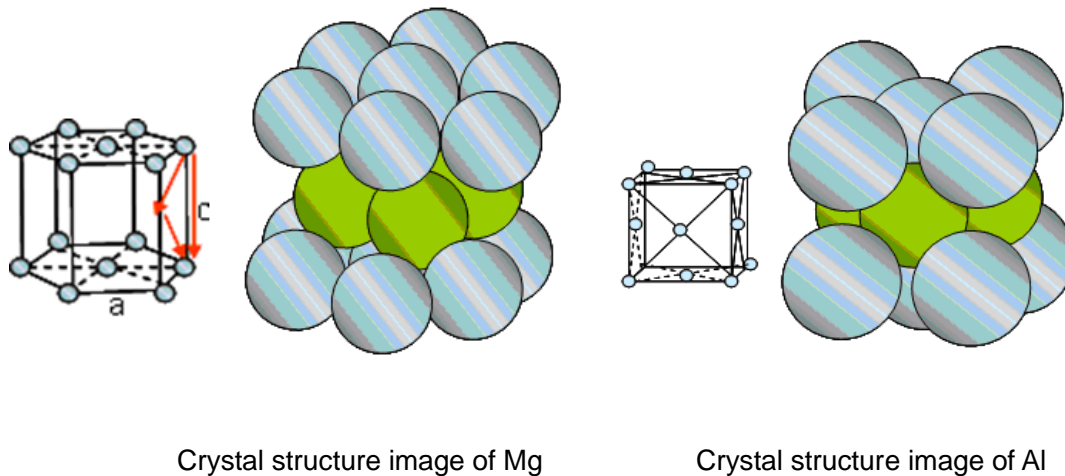
Fig. 2.2 Crystal structure image.

Table2.3 Thermo physical characteristic and mechanical property.

Material	Melting point /℃	Boiling point /℃	Density /g・cm-3	Specific heat capacity /J・kg-1・K-1	Heat conductivity /W・m-1・K-1	Tensile strength /MPa	Young modulus /GPa	Elongation /%
Mg-AZ31	649	1090	1.74	1038	155.5	165	44	44
Al-6061	660	2520	2.70	917	238	175	72	42

Aluminum is a relatively soft, durable, lightweight, ductile animal liable metal with appearance ranging from silvery to dull gray, depending on the surface roughness. It is nonmagnetic and does not easily ignite. Physical and mechanics performance as shown in Fig.2.2, Aluminum is a good thermal and electrical conductor, having 59% the conductivity of copper, both thermal and electrical, while having only 30% of copper's density. Aluminum is capable of being a superconductor with a superconducting critical temperature of 1.2 Kelvin and a critical magnetic field about 100 gauss (10milliteslas) [5]. Aluminum atoms arranged in a face-centered cubic (fcc) structure. Structural model as shown in Fig.2.3, Aluminum has stacking-fault energy of approximately about 200 mJ/m^2. Alloys composed mostly of aluminum have been very important in aerospace manufacturing since the introduction of metal skinned aircraft. Aluminum-magnesium alloys are both lighter than other aluminum alloys and much less flammable than alloys that contain a very high percentage of magnesium.

The chemicals reaction between metals produced when the both of Mg and Al were bonded because the metals had the difference of physical and chemical [6]. The study analyzed Mg-Al binary phase diagram to control bonding temperature, so that reach greater bonding effect. The Al-Mg phase diagram is shown in Fig 2.3. The dotted line in phase diagram clearly indicated separately phase change of the Mg-AZ31 and Al-6061 from high temperature to low temperature [7]. According to the weight percent of Mg-AZ31 in the phase diagram, L phase appear above 650℃, L-α phase appear from 590℃ to 650℃, α phase is 210℃ to 590℃, α-β phase is below 210℃. Binary alloy state diagram is the actual reflect of metallurgical reaction of Mg and Al (The process from liquid phase to solid phase, the microstructure in transition zone and element distribution on diffused bonding surface were analyzed, the results show that Mg and Al solid state reaction formed product in the element concentration under the heating temperature [8]. As shown in Fig. 2.3. Phase

diagram shows the aluminum solid solution (Al), the liquid phase L and the magnesium solid solution (Mg) at 470℃ produced in phase fields [9].

Under equilibrium conditions, the bonding could contain single-phase and solidification regions. However, reaction involving range of the R phase formed is very small under the temperature from 300℃ to 350℃. It is assumed that the structure of the solidified bonded zone present from 410℃ to 450℃, the formation of $Mg_{17}Al_{12}$ phase in the middle of the temperature range is more noticeable in Fig. 2.3(a,b). The composition range for the $Mg_{17}Al_{12}$ phase has been established, it is shown that the composition of the phase is from 45% to 60% according to the percents of Mg [10]. A composition range of 40% extends over a greater distance the $Mg_{17}Al_{12}$ phase has greater compositional ranges [11]. It is results that Mg forms from low concentration phase to high concentration phase in turn. And when the concentration of Mg and Al is approximate, reaction formed $Mg_{17}Al_{12}$ phase. The eutectic $Mg_{17}Al_{12}$ phase formed through the analysis of phase diagram under the temperature of 437℃. Therefore, bonded experiment could be carried out under the temperature. But also provide a theoretical basis for temperature setting in this study.
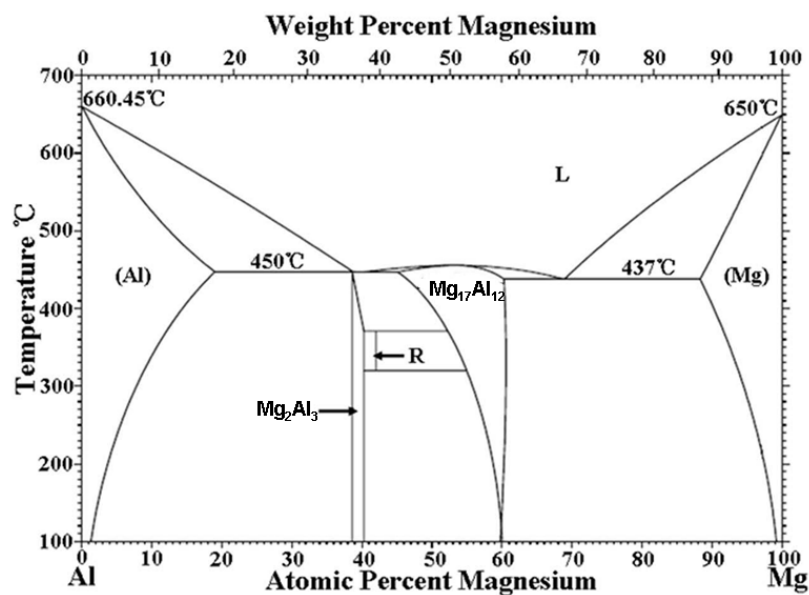
Fig. 2.3 (a) Al-Mg alloy phase diagram.
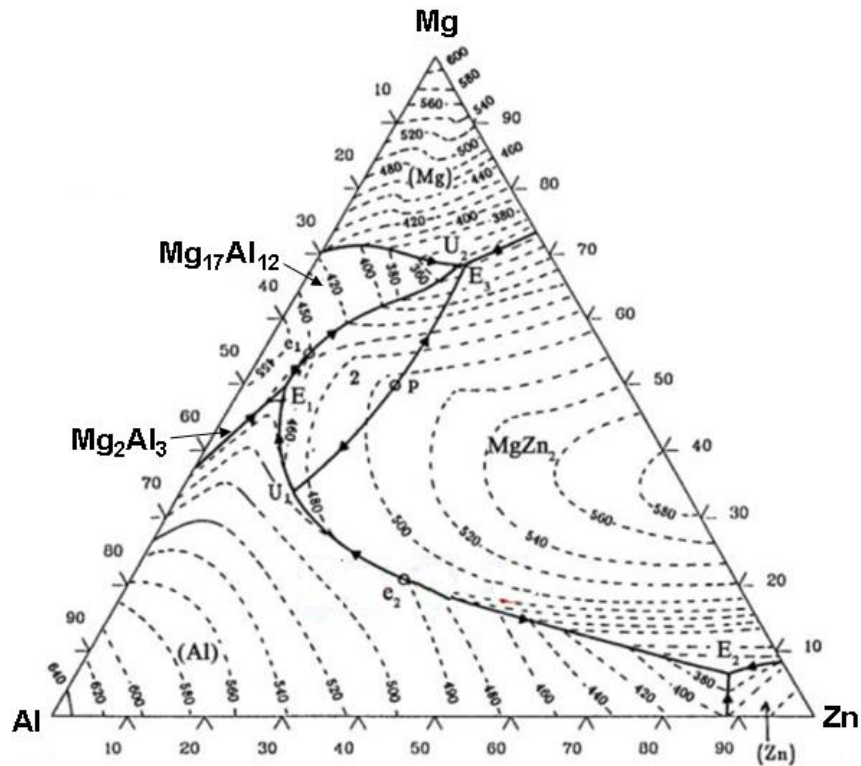
Fig. 2.3(b) Mg-Al-Zn alloy phase diagram.

2.3 Test equipment and technology

Adopting vacuum diffused welding process for Mg and Al alloy conducted welding. According to physical and chemical performance confirmed bonding process parameters under different craft conditions with pressure/no pressure.

2.3.1 Equipment and craft of diffused welding under pressure

When conducted diffused welding for Mg/Al alloy, the equipment could pressure and control temperature was adopted as shown in Fig. 2.4. The power was 45KW which selected unidirectional vertical to pressure. It is constituted of vacuum furnace, pressure system, heating system and control temperature system [12]. Because of the computer play the control role, the heating temperature, welding pressure, holding time and vacuum degree could be precisely controlled to improve precise degree and reliability in the welding process.
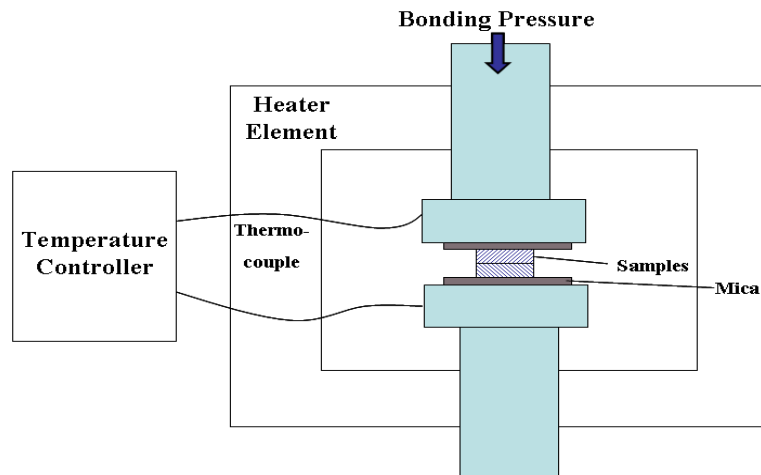
Fig. 2.4 Schematic of diffused bonding under pressure.

The specimen was polished with the #600 and #1200 sandpaper. Using metallographic sandpaper polished Mg/Al welded joint on the surface of the sample. For removing the impurities, the polished material was placed in the mixture of ethanol and acetone (mixing ratio of 1:1) and kept 3min cleaning in the ultrasonic cleaner, the surface is bright and clean. Then use polishing liquid on the velvet polishing processing, until the surface is bright and clean, no scratches [13]. But the higher the activity of Mg and Al still can form oxidation film after polishing, so the sample surface treatment should be strictly controlled the formation of oxide film. Then the specimens were desiccated after water cleaning. Finally, clean and flat specimen would be equipped and superimposed according to the method and was compressed put into the vacuum furnace. The really picture of sample loading is as shown in Fig. 2.5. The range of diffused welding craft parameters was that the heating temperature was from 400℃ to 460℃, holding time was 10-15min, bonding pressure was 0.1-0.5MPa and vacuum degree was 1.33×10^{-4}Pa.
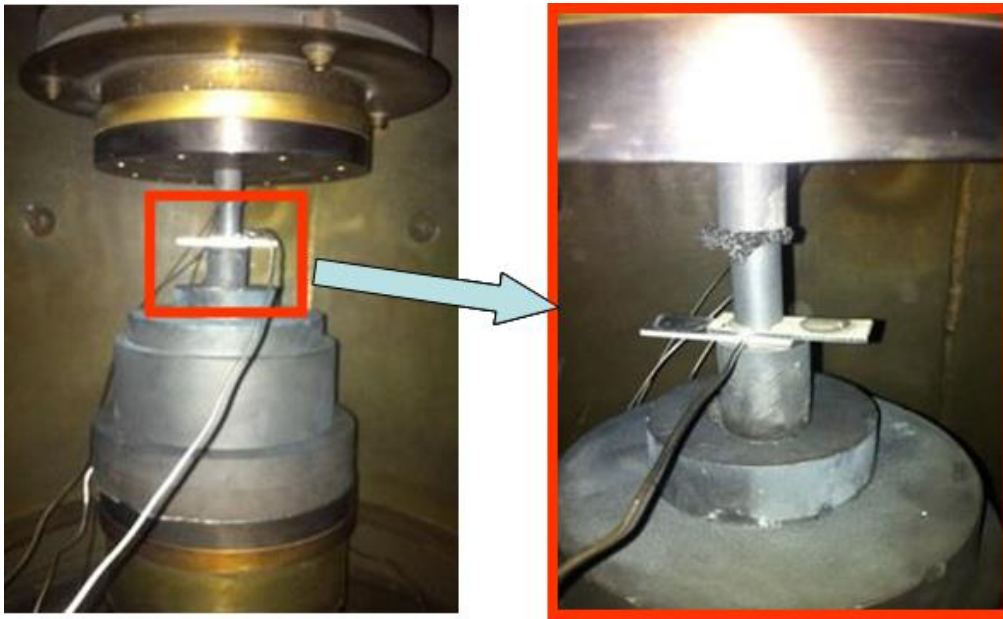
Fig. 2.5 Schematic of diffused bonding under pressure.

By the equipment of vacuum diffused welding, the different heating temperature, holding time and pressure adopted to conduct process experiment for Mg/Al diffused welding. Craft parameters were as shown in table 2.4 and bonding state under typical condition was as shown in Fig. 2.6.

Table 2.4 Temperature and pressure.

TRY	1	2	3	4	5
Temperature （MAX）	480°C	420°C	430 °C	440 °C	440°C
KN(MAX)	1	0.5	0.28	0.07	0.16

The specimen TRY1 produced obviously deformed and made the crystal grain coarse, the brittleness increasing and extrusion deformation on the joint due to high heating temperature and pressure, so that diffused connect did not formed. It is shown that the effect was obviously for diffused welding process when the temperature and pressure was high cause to not easy to obtain good

diffused joint. Under reduced the heating temperature and pressure, bonding interface did not formed effective area contact the atoms in whose surface was not fully lead to effectively diffused connect was not formed.
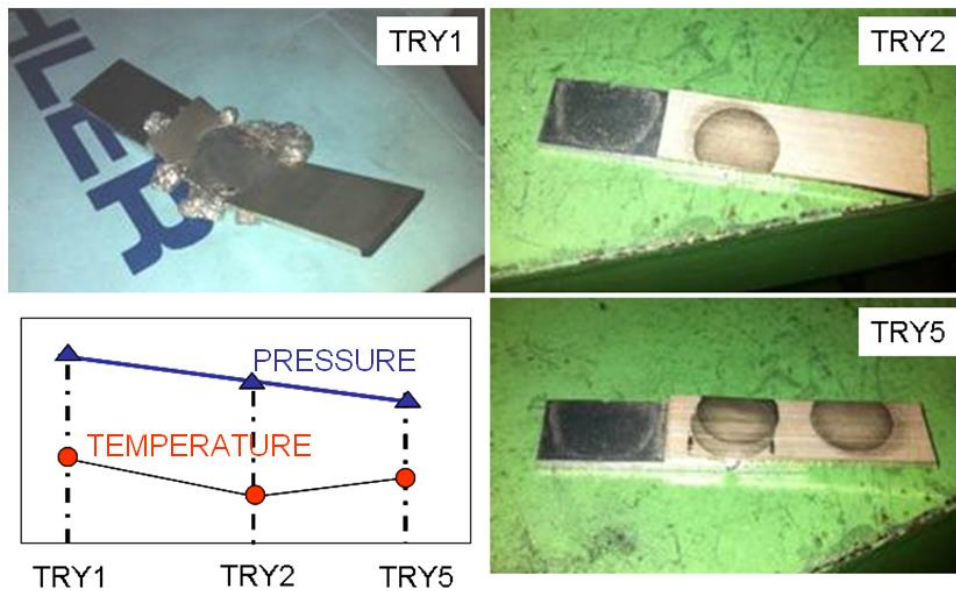
Fig.2.6 Bonding state image under typical craft parameters.

The heating temperature was raised while reduced pressure, the base material did not produced plastic deformation and the brittle rupture phenomenon and could obtain good diffused joint. A large area of effective contact on the interface produced a certain atoms diffused bonding. It is shown that the good diffused joint may be obtained under the heating temperature and pressure [14]. According to above the experimental results of pressure diffused welding craft, the good diffused bonding joint was obtained under the heating temperature and diffused welding pressure 0.16MPa.

2.3.2 Equipment and craft under no pressure diffusion

The specimen pre-polished cleaned was put into homemade fixture by docking method in Fig.2.7 and Fig.2.8. Thermocouple was connected to measure the temperature so that the correct test temperature can be secured.

In the diffusion welding process, Ar as protective gas was used. Flow meter was 150mm/hg. The optimization pressure craft parameters were obtained by a large of experiments. When the heating temperature was 440°C, the diffused effect was best. At the same time, the heating rate, holding time and cooling rate as three platforms under constant temperature for diffused effect to conduct analysis. Figure 2.9 was the process parameters curve of the heating rate, heating time and cooling rate.
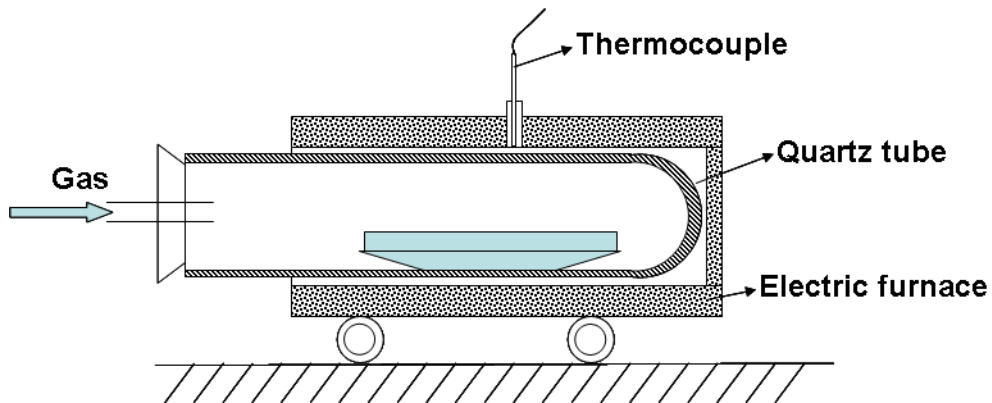
Fig.2.7 Electric furnace schematic.
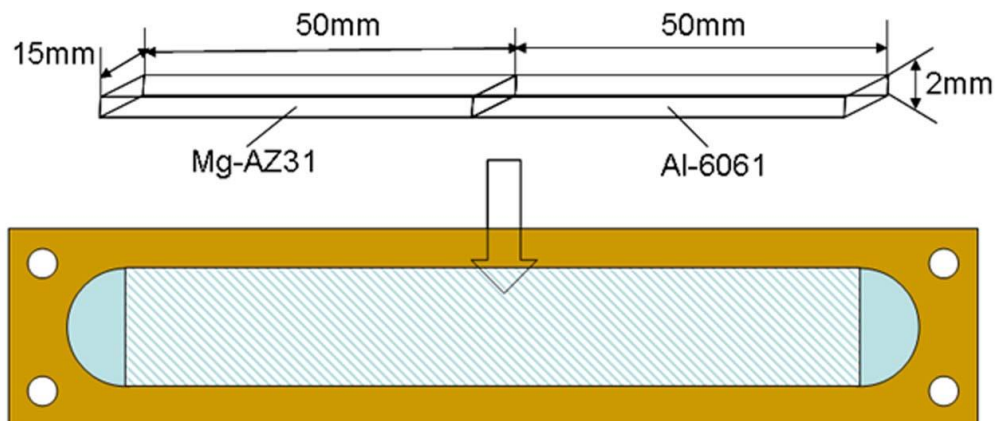
Fig.2.8a Bonding mode and homemade fixture.
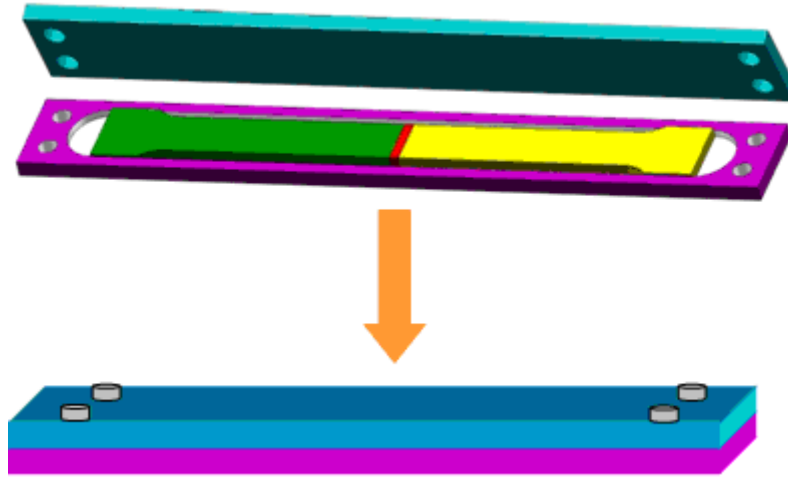
Fig.2.8b　Bonding mode and homemade fixture.
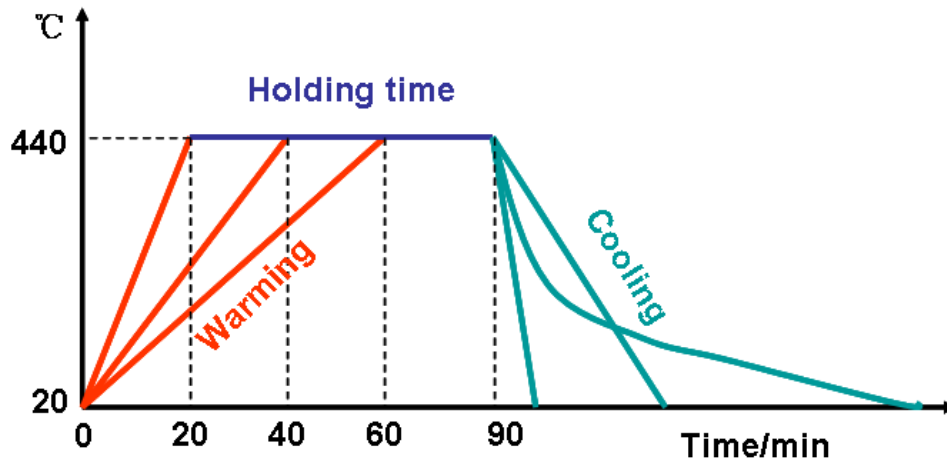
Fig.2.9 Process parameters curve under heating time-cooling rate.

2.4 Sample preparation and corrosion

The organizational structure and performance on the bonding interface Mg/Al alloy diffused joint was analyzed after cutting specimen. Firstly, prepared specimen was observed by cut method about organizational corrosion for bonding zone. Line cut method to diffused joint was used under pressure and no pressure. The cut of joint specimen was as shown in Fig. 2.10.
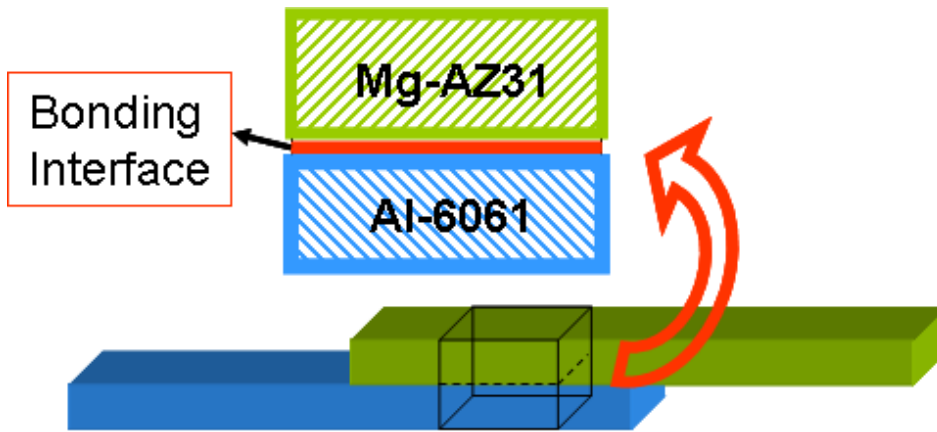
Fig 2.10 Pressurized joint specimens cut diagram.
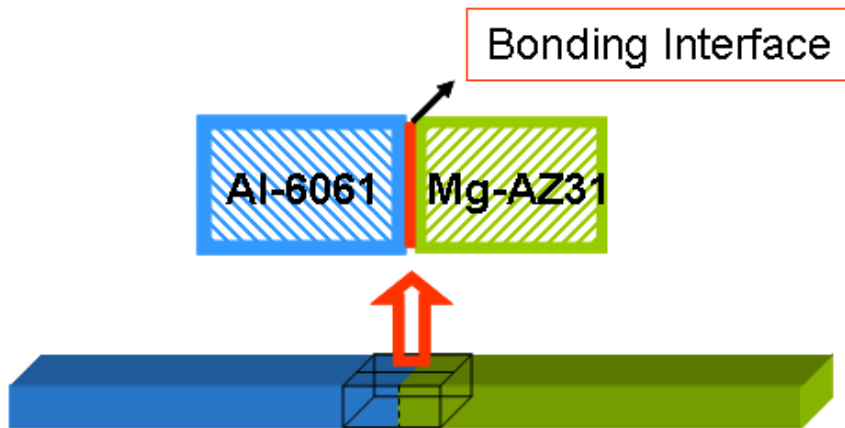
Fig.2.11 No pressurized joint specimens cut diagram.

The specimen was polished with the #600 and #1200 sandpaper. Using metallographic sandpaper polished Mg/Al welded joint on the surface of the sample, For removing the impurities, the polished material was placed in the mixture of ethanol and acetone (mixing ratio of 1:1) and kept 3min cleaning in the ultrasonic cleaner, the surface is bright and clean. Then use polishing liquid on the velvet polishing processing until the surface is bright, clean and no scratches. But the higher the activity of Mg and Al still can form oxidation film after polishing, so the sample surface treatment should be strictly controlled the formation of oxide film, and then according to the different corrosion resistance of Mg, Al. Interface Mg side corrosion of alcohol concentration 10%

HNO$_3$ solution or put sample coated with MgO style deerskin grinding paste; Al side corrosion was carried out as a degree of HF 5% alcohol solution. Then the specimens were desiccated after water cleaning [15]. Subtle organization of diffused zone on diffused interface after corrosion treatment on the surface was observed. The specimen no corroded was applied to conduct elemental analysis and determination. The sheet specimen cut from Mg/Al diffused interface by FIB was used by transmission electron microscopy (TEM). The sampling position was shown in Fig. 2.12.
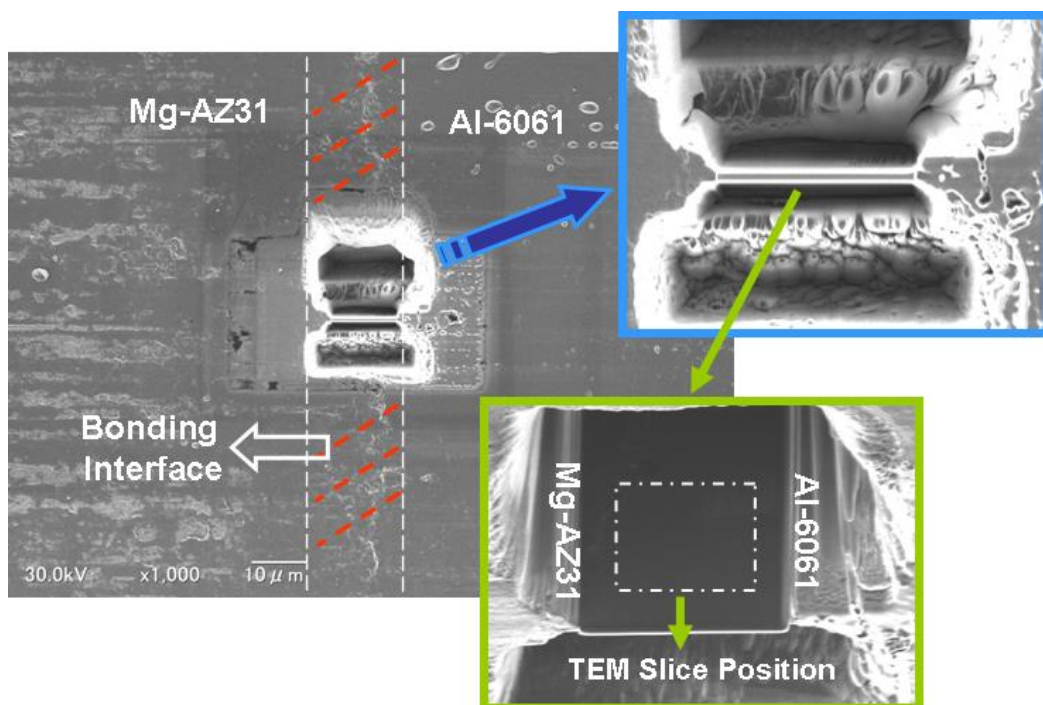
Fig. 2.12 TEM sampling position.

2.5 Experiment detection and analysis

The specimen after bonding was conducted tensile experiment by electronic universal testing machine, tensile equipment as shown in Fig. 2.13, tensile rate was 0.5mm/min. The tensile strength under pressure was as shown in Fig. 2.13.

In order to secure the stress of the tensile tests on the same vertical line,

the both ends of the text pieces are added with 2 mm thick metal gaskets. Principal stress was calculated by establishing Mohr's stress circle model due to torque deflection easy to be produced in tensile process [16]. When the tensile strength under no pressure was detected, in order to further obtain accurate ultimate tensile strengths, butt joint diffused bonding was conducted under the same experimental condition to avoid produce torque deflection [17]. According to international standard ISO6898-2 made the specimen process a certain size as shown in Fig. 2.13.
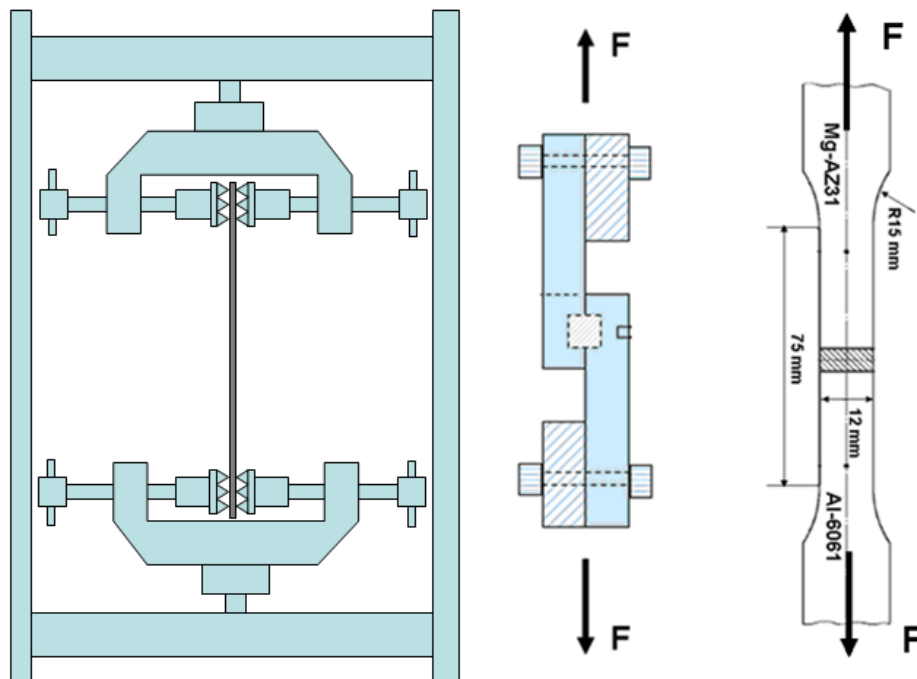
Fig.2.13 Stress analysis of fracture interface.

The effect of process parameters such as bonding temperature, bonding pressure, holding time and surface roughness on shear strength, bonding strength, diffusion layer thickness and interface characterization were analyzed [18]. Scanning Electron Microscopy (SEM), EPMA, TEM, Electron Dispersive Spectrum (EDS) and X-ray Diffraction (XRD) techniques were used to characterize the joints. And section after tensile was observed, the fracture mechanism under different conditions were analyzed. Simulation of stress and

strain was conducted by ANSYS software and to analyze the position easy to produce fracture and to statement for bonding mechanism according crystal structure.

2.6 Concluding remarks

The section adopted chemical composition and performance Mg and Al bases about topics experiment, provided equipment and craft parameters of Mg/Al dissimilar metals welding experiment. The preparation of joint and significant erosion technology on micro organization were also adopted. The methods and the parameters of the mechanical properties, micro organization, element distribution and micro structure of Mg/Al dissimilar metals on welding zone were stated. The fracture and bonding mechanism on the interface were analyzed according to crystal structure.

References

[1] P. Sanders, J. Keske, K. Leong, G. Kornecki. High power Nd:YAG and CO_2 laser welding of magnesium. J. Laser. Appl, 1999, **11**, 96–103.

[2] K. Leong, G. Kornecki, P. Sanders, J. Keske. Laser Beam Welding of AZ31B-H24 Magnesium Alloy. In Proceedings of the ICALEO 98: Laser Materials Processing Conference, Orlando, FL, USA, 16–19 November 1998.

[3] B. Mordike, T. Ebert. Magnesium: Properties-applications-potential. Mater. Sci. Eng. A, 2001, **302**, 37–45.

[4] M. Marya, D. Olson, G. Edwards. Welding of Magnesium Alloys for Transportation Applications. In Proceedings of the Materials Solution '00 on Joining of Advanced and Specialty Materials, St. Louis, MO, USA, 9–11 October 2000, pp. 122–128.

[5] M. Pastor, H. Zhao, T. DebRoy. Continuous wave Nd:yttrium aluminium garnet laser welding of AM60B magnesium alloys. J. Laser. Appl. 2000, **12**, 91–100.

[6] E. Aghion, B. Bronfin. Magnesium alloys development towards the 21st century. Mater. Sci. Forum, 2000, **350**, 19–30.

[7] M. Marya, G. Edwards, S. Marya, D. Olson. Fundamentals in the Fusion Welding of Magnesium and Its Alloys. In Proceedings of the Seventh JWS International Symposium, Kobe, Japan, 20–22 November 2001.

[8] X. Cao, M. Jahazi, J. Immarigeon, W. Wallace. Review of laser welding techniques for magnesium alloys. J. Mater. Process. Technol, 2006, **171**, 188–204.

[9] P. Liu, Y. Li, H. Geng, J. Wang. Microstructure characteristics in TIG welded joint of Mg Al dissimilar materials. Mater. Lett, 2007, **61**, 1288–1291.

[10] H. Baker, H. Okamoto. Alloy Phase Diagrams, 9th ed.; ASM International: Geauga County, OH, USA, 1995.

[11] J. Wang, Y. Li, P. Liu, H. Geng. Microstructure and XRD analysis in the interface zone of Mg-Al diffusion bonding. J. Mater. Process. Technol. 2008, **205**, 146–150.

[12] E. Hajjari, M. Divandari, S. Razavi, S. Emami, T. Homma, S. Kamado. Dissimilar joining of Al Mg light metals by compound casting process. J. Mater. Sci. 2011, **46**, 6491–6499.

[13] Y. Miyashita, R. Borrisutthekul, J. Chen, Y. Mutoh. Application of twin laser beam on AZ31-A5052 dissimilar metals welding. Key Eng. Mater. 2007, **353**, 1956–1959.

[14] V. Firouzdor, S. Kou. Al-to-mg friction stir welding effect of material position, travel speed, and rotation speed. Metall. Mater. Trans. A 2010, **41**, 2914–2935.

[15] S. Yutaka, H. Seung, M. Masato, K. Hiroyuki. Constitutional liquation during dissimilar friction stir welding of Al and Mg alloys. Scr. Mater. 2004, **50**, 1233–1236.

[16] S. Hirano, K. Okamoto, M. Doi, H. Okamura, M. Inagaki, Y. Aono. Microstructure of dissimilar joint interface of magnesium alloy and aluminum alloy by friction stir welding. Quart. J. Jpn. Weld. Soc. 2003, **21**, 539.

[17] S. Park, M. Michiuchi, Y. Sato, H. Kokawa. Dissimilar Friction-Stir Welding of Al Alloy 1050 and Mg Alloy AZ31. In Proceedings of the International Welding/Joining Onference-Korea, Gyeongju, Korea, 28–30 October 2002.

[18] Y. Yan, D. Zhang, C. Qiu, W. Zhang. Dissimilar friction stir welding between 5052 aluminum alloy and AZ31 magnesium alloy. Trans. Nonferrous Met. Soc. China 2010, **20**, 619–623.

Chapter 3 Organizational characteristics and interface strength on diffusion bonding of Mg-AZ31/Al-6061 under pressure

3.1 Introduction

According to Mg/Al binary alloys phase diagram, it is known that Mg/Al substrates metal under a certain pressure formed Mg/Al eutectic by Mg and Al elements inter diffusion at 437°C in the heating temperature process. When AZ31 alloy and 6061 alloy together heating up to above eutectic temperature, eutectic phase would appear on contact surface, so that directly diffused effect for Mg/Al dissimilar metals conducted connection.

For craft aspect, the scale of the substrate metals under diffused reaction was difficult to control. Because eutectic was increasing in holding time, the process of eutectic formed was not stopped until only under the heating temperature reduced lower than eutectic temperature [1, 2]. But the joint performance was mainly decided through the reaction on joint interface. What reactions were produced and what were the amounts and form, in which distributed states for joint performance played a decisive role [3]. For Mg and Al dissimilar metals under pressure diffused bonding, eutectic phase of brittleness intermetallic compounds and simple phase formed diffused layers between substrates, so that controlling intermetallic compounds amount for improving joint performance played a key role before effectively bonding.

Mg/Al alloy under pressure was affected by Mg heat brittleness because Mg/Al different conduct heat parameters easy to produce pores in joint welding line, so that seriously affected the organizational performance of Mg/Al dissimilar metals joint [4]. Therefore, reducing diffused shortcoming and

obtaining good performance diffused joint by the study of Mg/Al alloy diffused joint organizational performance under pressure had a importance significance [5].

The paper was to study Mg/Al alloy joint strength and diffused organizational performance under pressure. The first, universal tensile testing machine was used to detect strength and calculate maximum principal stress under pressure. Scanning electron microscopy (SEM) was adopted to observe cut fracture form and micro structure in diffused bonding zone. By electron microprobe (EPMA) and X-ray diffraction (XRD), the element distributed on fusion zone and micro phase structure were detected and analyzed and lay the importance foundation for the depth study and popularize about Mg/Al alloy diffused joint micro organizational structure.

3.2 Micro organizational structure on bonding interface under pressure

3.2.1 SEM image of interface zone

SEM observation of bonding interface microstructure nearby the transition zone of diffusion bonding surface can reflect forming and structure, the bonded samples of Mg/Al dissimilar metals were cut and the microscopic sample was prepared [6]. The transition zone of diffusion bonding was taken by scanning electron microscopy (SEM) is as shown in Fig.3.1. Diffusion bonding surface of Mg/Al has obvious diffusion characteristics and the white brilliant and diffusion zone of new phase compound was formed between base metal of Mg and Al, in which organizational characteristics is different with the base metal [7]. It is indicated that new phase compound was formed with sloppy structure in the side of Mg interface transition zone and the new phase compound appear dense structure in the side of Al and it is quite evident that the plate exhibits a typical dendrites' structure [8]. The pitting is uniform and the structure is rich, and a particle size exists in the range about less than 2μm. Mg/Al intermetallic compound formed under the condition of heating temperature and uniform apertures pitting is detected and the apertures pitting were small and distributed approximately uniformly. Finally, it is results that the structure is dense and uniform under pressure.
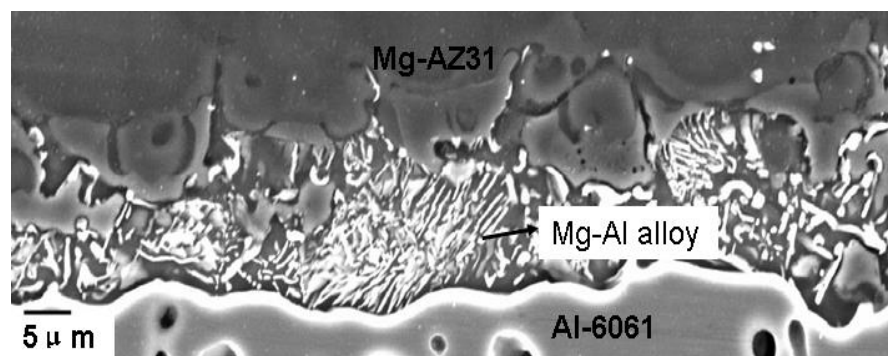
Fig.3.1 SEM microstructure of interface region under pressure.

3.2.2 XRD pattern structural characterization about intermetallic

As shown in Fig.3.2, the results show that $Mg_{17}Al_{12}$ can be generated by crystallites XRD analysis. As shown in Fig.3.2, the experimental results consist of multiple phases. Specifically, microstructure and the element concentration distribution analysis showed that Mg/Al intermetallic compound phase existed. In order to further research phase structure existed, the phase composition of Mg/Al dissimilar metals in diffusion interface was analyzed by X-ray diffraction experiment [9]. Cu-Kα target was adopted; working voltage is 40kV; working current is 150mA. It is results that Mg/Al intermetallic compound named $Mg_{17}Al_{12}$ phase was formed in transition zone of Mg/Al dissimilar metals after diffusing [10]. The forming of $Mg_{17}Al_{12}$ is near the one side of Mg base metal due to Al element neared Mg base metal accompanied empty seats and replacement diffusion mechanism; the diffusion bonding is more fully under pressure.
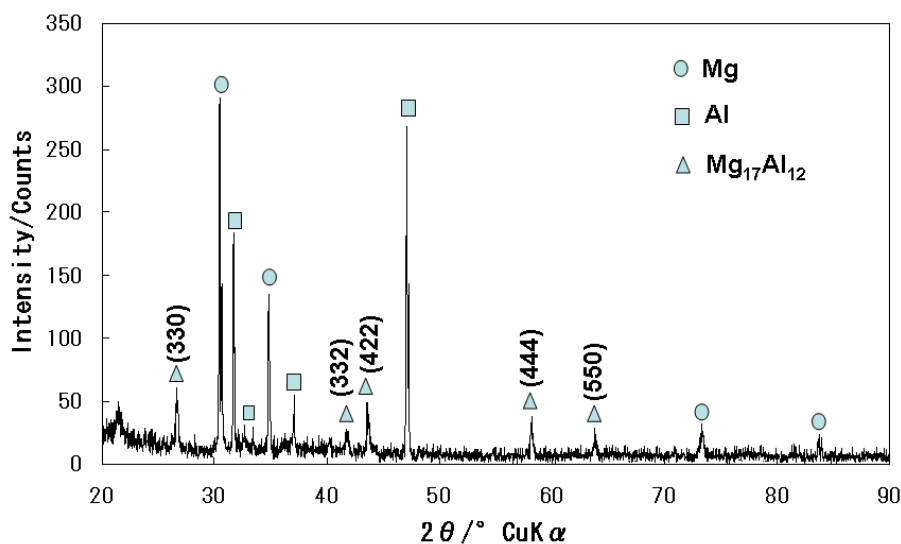
Fig.3.2 XRD patterns of bonding interface.

3.3.3 EPMA element distribution of interface zone

As shown in Fig.3.3, the elementary distributions in the transition zone of diffusion interface can be obtained by EPMA observation. Surface elementary

distribution in the transition zone of diffusion interface is as shown in the Fig.3.3. It is indicated that elements of Mg, Al, Si and Zn are mainly distributed in the transition layer. According to the distribution of Mg element and Al element, Mg and Al was obvious and was distributed separately between Mg side and Al side. Mg and Al elements mutual diffused to each side, so that reached a dense bonding [11]. The elementary distribution of Mg, Al, Si and Zn reflected the generation of Mg-Al-Zn alloy phase. The transition zone played the role of the mutual diffusion effect. The results are consistent with that of XRD analysis.
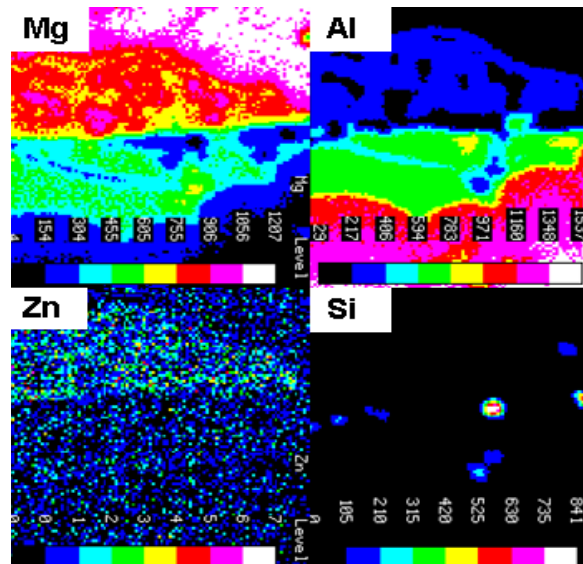
Fig 3.3 Elements face scan of the weld bonding of Mg to Al.
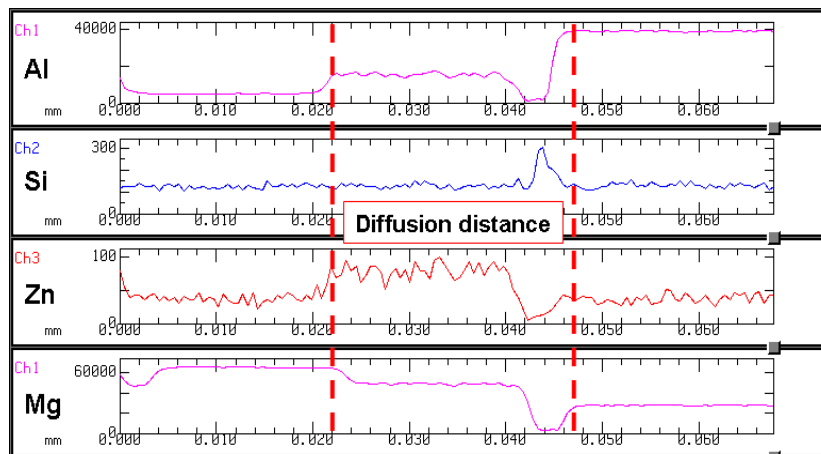
Fig 3.4 Elements line scan of the weld bonding of Mg to Al.

3.3 Mg/Al alloy tiny structure observation under pressure

3.3.1 TEM analysis of structure and position orientation

In order to further study phase structure of the Mg-AZ31/Al-6061 in transition interface zone, the structure near diffusion interface and position orientation relationship between phase structure were analyzed by TEM, as shown in Fig.3.5, Mg and Al transition sides are the electron diffraction diagrams and the index standardization result of $Mg_{17}Al_{12}$ was proved [12]. $Mg_{17}Al_{12}$ compounds existed near crystal boundaries in form of clumps, crystal face index of the body centered cubic (BCC) of $Mg_{17}Al_{12}$ phase structure is (444) by calibrating diffraction spots corresponding, crystal plane spacing is 0.152 nm, which closed to the result of XRD, thus further proves that the existence of $Mg_{17}Al_{12}$. As shown in Fig.3.6, the grain becomes refinement; the array is more compact and the diffusion is full [13]. The results were obtained based on XRD standard PDF card with pressure. $Mg_{17}Al_{12}$ exists in the boundary of crystal boundary, it is indicated that Al element diffused near Mg crystal boundary to gather together and bonded with precipitation Mg, so that achieve a certain effect [14]. The analysis based on the bonding density of Mg side in Mg/Al diffused interface with enhancement effect appeared in the region due to $Mg_{17}Al_{12}$ diffusion formed intermetallic phase [15]. It dispersed distributed on Mg crystal in granular second phase due to $Mg_{17}Al_{12}$ phase element diffusion formed in bulk form existence near Mg crystal boundary [16]. And it play a role of pinning for transition layer, but also to improve the bonding strength of the diffusion interface.
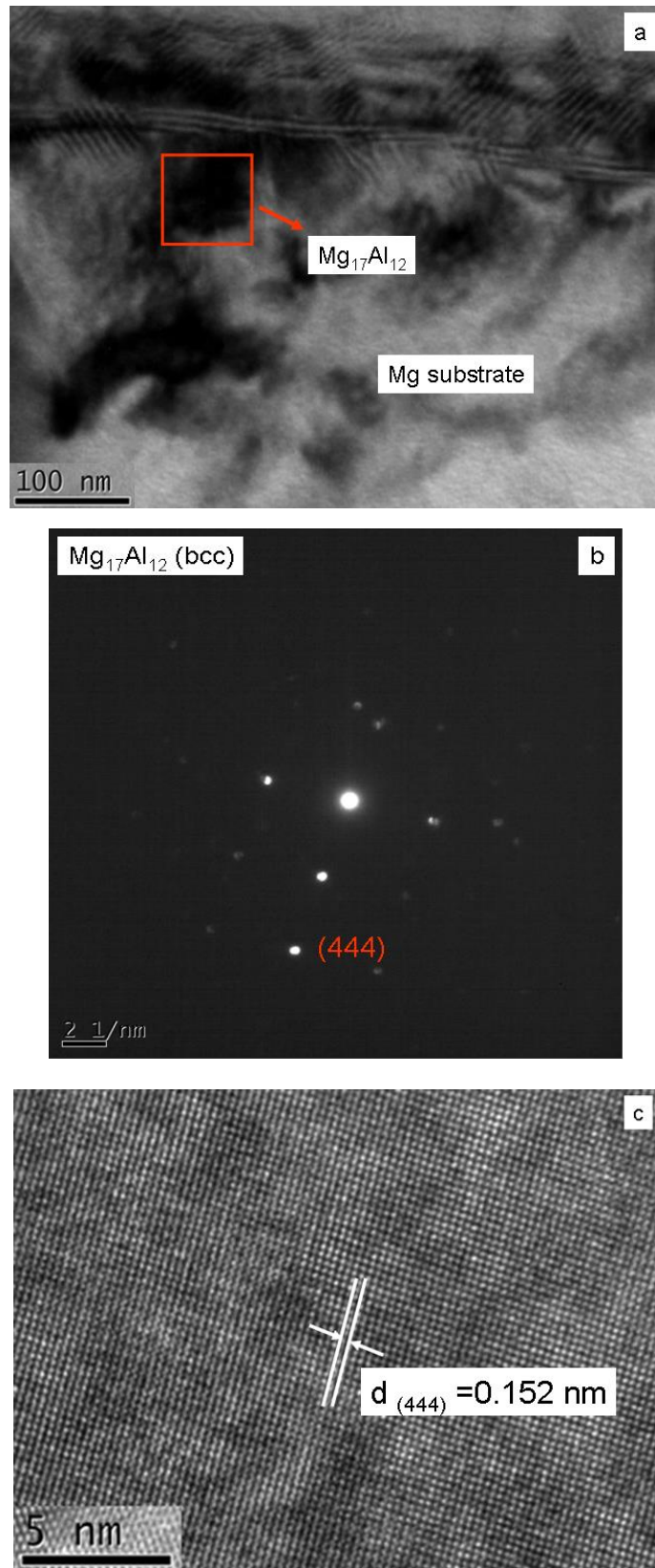
Fig.3.5 Feature of the fine structure near the Mg transition layer ($Mg_{17}Al_{12}$ phase) in the Mg/Al diffusion bonding interface.
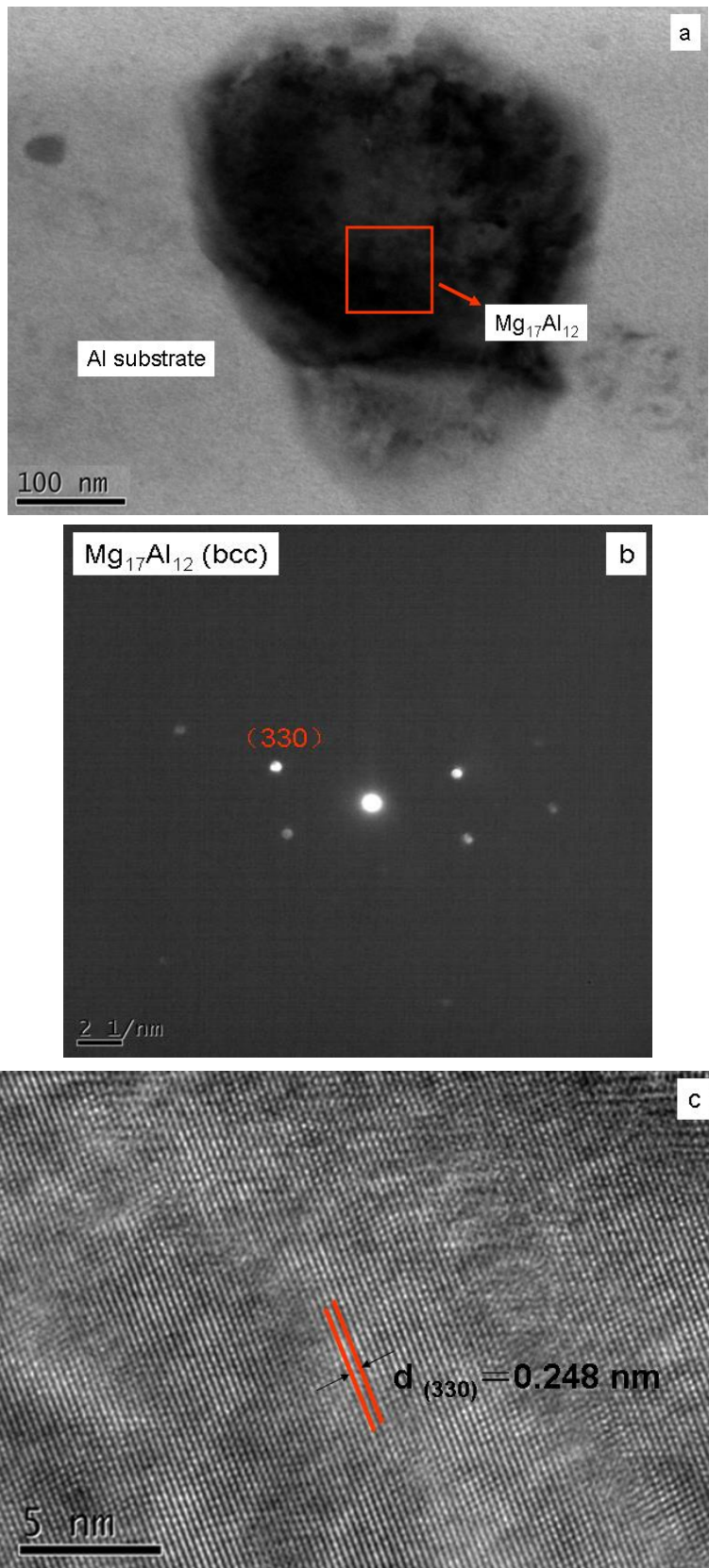
Fig.3.6 Feature of the fine structure near the Al transition layer ($Mg_{17}Al_{12}$

phase) in the Mg/Al diffusion bonding interface.

3.3.2 EDS analyzes of Mg-AZ31/Al-6061 diffusion interface

As shown in Fig. 3.7, the distribution of Mg and Al elements was observed in Mg/Al fracture interface transition layer by EDS analysis. It is indicated that mass percentage of Mg and Al is 55.96%: 40.13% in Mg side transition layer. That of Mg and Al is 44.8%: 48.88% in Al side transition layer [17]. Based organizational Al-base solid solution phase could be judged in reaction layer by the analysis of XRD. The distribution of Al element in Al side was uniform and the concentration was relatively higher was than that of Mg side and in which the content of Zn element was observed [18]. The results show that Al-base solid solution fully diffused to Mg side and formed dense bonding layer. In the bonding layer, the distribution of Mg element and Al element was uniform. The application of soak and sintering methods produced great effect for bonding and formed melt with MgAZ31 in bonding process. When Al-base solid solution inhibited brittle phase; it improves the tenacity of binding layer, so that improved mechanical strength; dense bonding can be achieved under no adding any materials between MgAZ31 and Al6061.

(a)   (b)
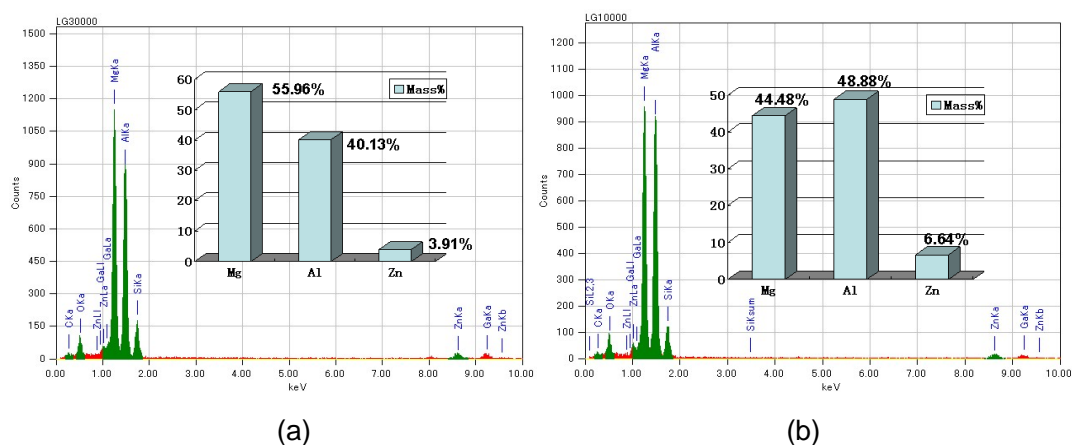
Fig.3.7 EDS analysis on the fracture of the bonding: (a) Mg-AZ31 (b) Al-6061.

3.4 Diffusion bonding strength of the Mg-AZ31/Al-6061 joint under pressure

3.4.1 Calculation tensile strength and maximum principal stress

In order to research bonding strength on diffused welding interface under pressure, CMTS150 micro-controlled electronic universal testing tensile machine was adopted to get tensile strength of Mg-AZ31/Al-6061 alloy diffused interface by using different process parameters. The size of tensile specimen is as shown in Fig. 3.8.
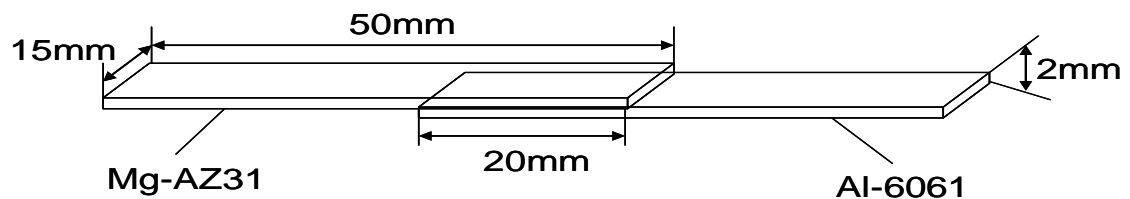
Fig. 3.8 The size of tensile specimen.

Tensile strengths of the bonding are evaluated by tensile testing at room temperature with a constant travel speed of 0.5 mm/min. Samples of bonded AZ31B Mg alloy (50mm×20mm×2mm) and 6061Al alloy (50mm×20mm×2mm) were used in the experiment. In order to secure the stress of the tensile tests on the same vertical line, both ends of the experiment are added with 2mm thick metal gaskets and then go on with the tensile test [19]. As is shown in Fig. 3.9(a), taking the overlapping welding samples for example, when the temperature has reached 440°C and the holding time is 60 minutes, and the measured tensile intensity at the overlap interface is 93 MPa.

In accordance with the different roles stress has played in the directions of the stress, it was fall into two categories: normal stress and shear stress [20]. A further stress analysis of the overlap interface was conducted on the overlap

interface and then the bonding parts of the samples have been divided into a lot of tiny rectangles [21]. A small rectangle was chosen from the overlap interface as a unit element for stress analysis. As is shown in Fig. 3.9(b), the normal stress is vertical to the X axis and the Y axis to be σ_x and σ_y, the shear stress is parallel to the X axis and Y axis to be τ_{yx}, τ_{xy} [22]. Because the added force is on the Y axis, it can be considered that the distributed components of σ_y and τ_{xy}. The stress of the σ_y as well as the surface are in conformity with the tensile test, its value may be used as the measured experiment value, namely σ_y and 93 MPa. The acting force is the same with σ_y. According to stress formula, it is result that the stress is equals to 186 MPa. It is indicated that the normal stress σ_y and shear stress τ_{xy} are of the same size and different directions [23]. Therefore the less stressed σ_y must be a certain angle θ of deflection. When deflected to the angle θ directions, there will be stress σ_1 generated to balance this torque [24]. The stress produced at the moment σ_1 is principal stress. Its stress direction will be round the X axis to the angle θ. According to the establishment of Mohr's stress circle Model we can know that the biggest principal stress is the on σ_1 axis. The σ_1 value can be calculated by calculating formula. The stress resulted from the θ deflection. From the equation (1) we can get the calculating formula (2). After calculation, it is indicated that the principal stress σ_1 equals to 238.22 MPa. It can be drawn from the experiments. After being sintered, Al based solid solution bonded with the participation of the Zn elements react has improved the separation out state of the brittle phase and enabling the interface obtaining the higher bonding intensity.

$$(\sigma_\theta - \frac{\sigma_x + \sigma_y}{2})^2 + \tau_\theta^2 = (\frac{\sigma_x - \sigma_y}{2})^2 + \tau_{xy}^2 \tag{1}$$

$$\sigma_1 = \frac{\sigma_x + \sigma_y}{2} + \sqrt{(\frac{\sigma_x - \sigma_y}{2})^2 + \tau_{xy}^2} \tag{2}$$
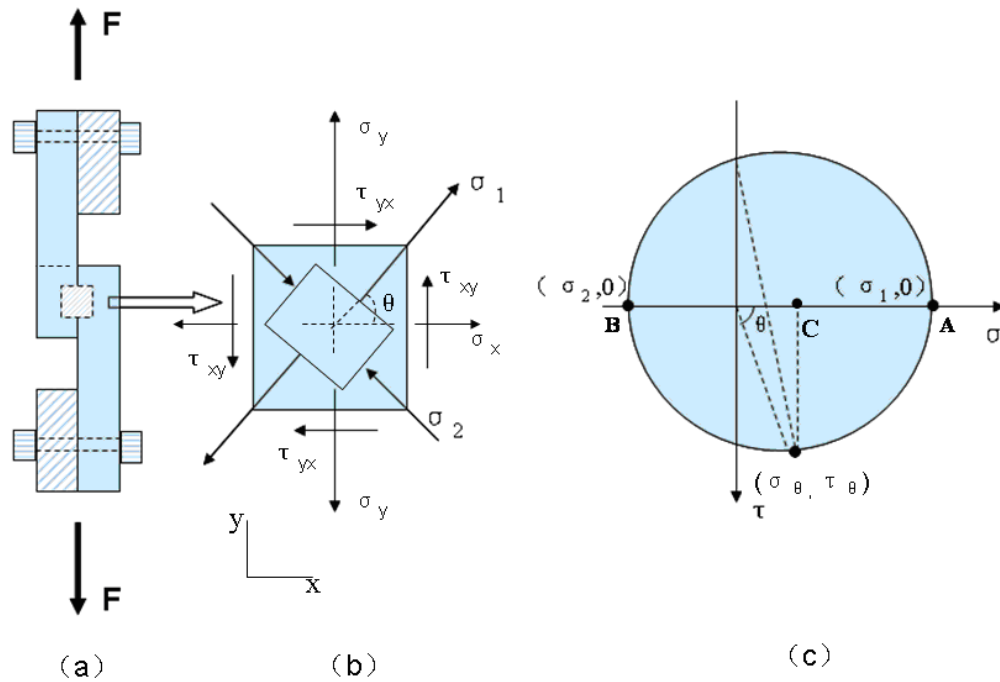
Fig. 3.9 Stress analysis image of fracture interface.

3.4.2 Observe of tensile fracture

The tensile fracture form of Mg/Al alloy diffused joint under pressure was observed by SEM to analyze fracture mechanism, so that help to understand the reason produce cracks on fusion.

The section morphology and fracture mechanism were observed by SEM. As shown in Fig. 3.10. The fracture belongs to typical ductile fracture morphology and the metal material produce micro hole with plastic deformation under the tensile strength [25]. At the sintering temperature of 440°C, with the increase of pressure, the interface bonding particles are transformed from the initial mechanical bonding to the mutual diffusion of elements. Meanwhile, the Zn elements in the Al base solid solution participating in the reaction and improve the dynamic performance of the interface [26]. With an increase of holding time, the diffusion of Mg, Al, Zn elements become more even and formed comparatively steady Mg-Al-Zn alloy layer. It has also held down the generation of the brittle phase which destroys

the mechanics intensity, and the ductile fracture attributes were clearly represented at the section.

Al side fracture was mainly constituted of many uneven pits. As shown in Fig. 3.10, dimple formation is due to metal material produce microscopic with the plastic deformation when joint fusion zone was under stress. The porous formed on precipitate or inclusions particles, as the stress increases, the hole constantly nucleating, growth, and connect to aggregates, finally, fracture was caused to form dimple.
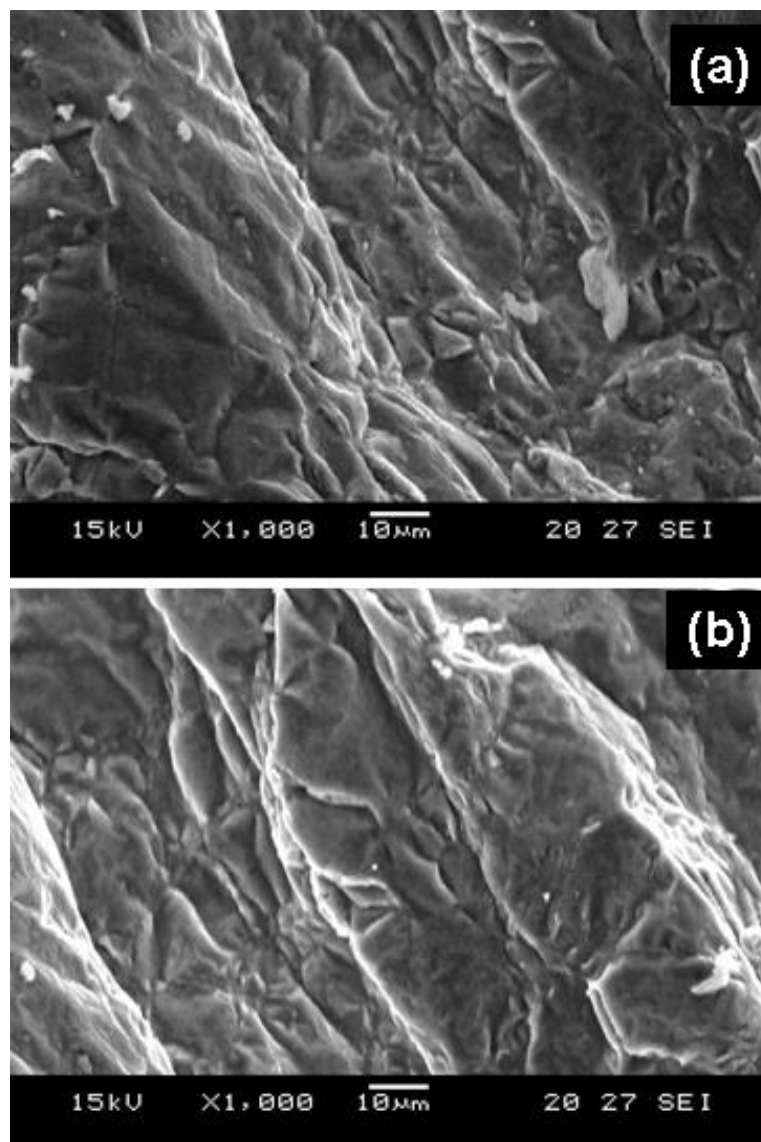
Fig. 3.10 SEM microstructure at the edge fracture of the bonding of Mg-AZ31 and Al-6061 (Al side).

Metal Mg fractured on elastic deformation stage and macro-brittle fracture was flush and bright. As shown in Fig. 3.11, joint Mg side fracture under pressure appear obvious brittleness fracture form and accompanied continuous plane and small flat plane belong to typical cleavage fracture [27]. Cleavage fracture was the brittleness form, when the fracture macroscopic plastic deformation was minimal. The form of Mg side fracture was the main cleavage accompanied a small of mixed fracture.
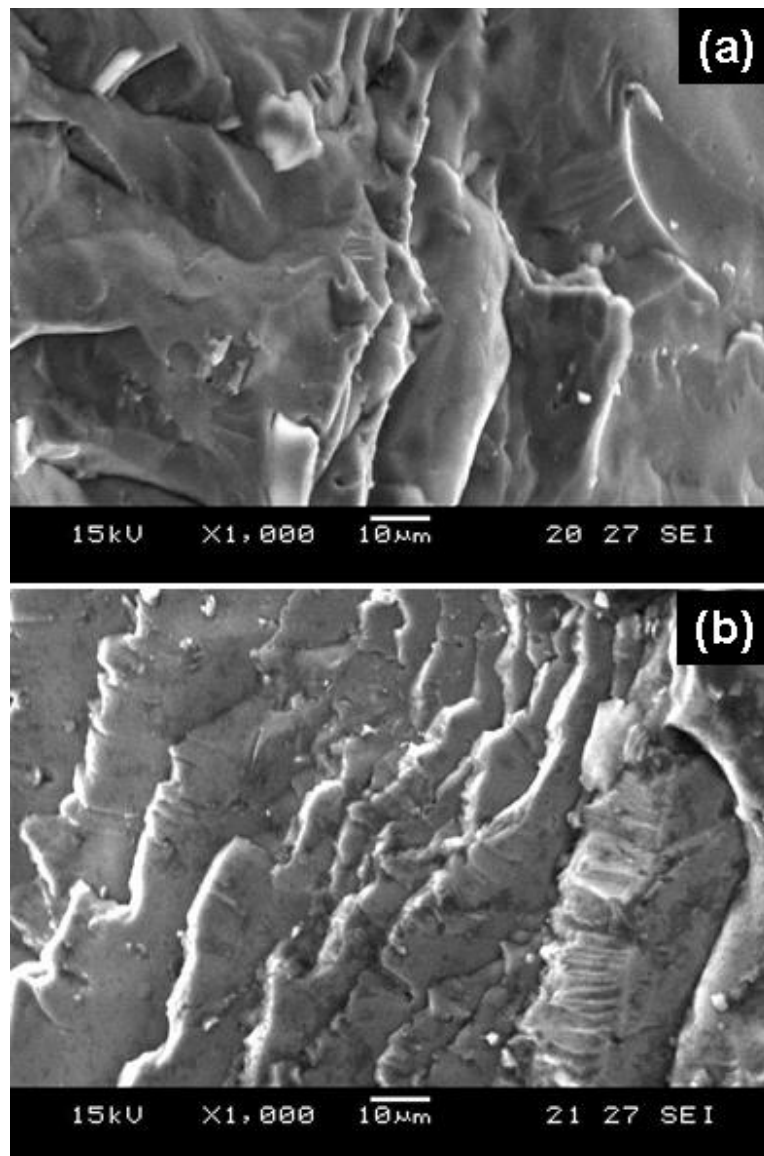
Fig.3.11 SEM microstructure at the edge fracture of the bonding of Mg-AZ31 and Al-6061 (Mg side).

According to the observation and analysis for joint fracture under pressure, Al side fracture was constituted of shaping of dimple fracture form; Mg side fracture belonged to typical brittle cleavage form and had a small plastic fracture features. It is related with Mg heat brittleness. At the same time, a large of pores produced on Mg side fracture and welding nearby Mg side fusion, which was a reason lead to fracture, strength and toughness reduce.

3.5 Concluding remarks

(1) Micro structure of Mg/Al alloy diffused welding joint interface under pressure showed that obvious columnar crystal structure appeared nearby Mg side fusion zone and vertically with Mg substrate and extending grown to welding line. Welding zone was constituted of small strip equated organization and black substrate. Fusion zone was constituted of molten and semi-molten crystal zone. Molten crystal zone was mainly constituted of coarse columnar grains and equated dendrite.

(2) Fracture analysis showed that joint Al side fracture was constitute of shaping of dimple fracture form; Mg side fracture belong to typical brittle cleavage form and a small plastic fracture features. At the same time, a large of pores produced on Mg side fracture and welding nearby Mg side fusion, it was a reason lead to fracture, strength and the reducing of toughness.

(3) XRD analysis showed that a large of alloy phases $Mg_{17}Al_{12}$. But a certain degree MgO and Al_2O_3 oxidation and brittle phase formed in welding line and fusion zone because Mg and Al were easy to be oxidized, so that was unfavorable for the organizational performance of the joint.

References

[1] U. Suhuddin, V. Fischer, J. Santos. The thermal cycle during the dissimilar friction spot welding of aluminum and magnesium alloy. Scr. Mater. 2013, **68**, 87–90.

[2] M. Mofid, A. Abdollah-Zadeh, F. Malek Ghaini. The effect of water cooling during dissimilar friction stir welding of Al alloy to Mg alloy. Mater. Des. 2012, **36**, 161–167.

[3] W. Chang, S. Rajesh, C. Chun, H. Kim. Microstructure and mechanical properties of hybrid laser-friction stir welding between AA6061-T6 Al alloy and AZ31 Mg alloy. J. Mater. Sci. Technol. 2011, **27**, 199–204.

[4] D. Choia, B. Ahna, C. Leec, Y. Yeon, K. Song, S. Jung. Formation of intermetallic compounds in Al and Mg alloy interface during friction stir spot welding. Intermetallics 2011, **19**, 125–130.

[5] Y. Kwon, I. Shigematsu, N. Saito. Dissimilar friction stir welding between magnesium and aluminum alloys. Mater. Lett. 2008, **62**, 3827–3829.

[6] P. Venkateswaran, A. Reynolds. Factors affecting the properties of Friction Stir Welds between aluminum and magnesium alloys. Mater. Sci. Eng. A 2012, **545**, 26–37.

[7] Y. Chen, K. Nakata. Friction stir lap joining aluminum and magnesium alloys. Scr. Mater. 2008, **58**, 433–436.

[8] S. Chowdhury, D. Chen, S. Bhole, X. Cao, P. Wanjara. Lap shear strength and fatigue life of friction stir spot welded AZ31 magnesium and 5754 aluminum alloys. Mater. Sci. Eng. A, 2012, **556**, 500–509.

[9] S. Chowdhury, D. Chen, S. Bhole, X. Cao, P. Wanjara. Lap shear strength and fatigue behavior of friction stir spot welded dissimilar magnesium-to-aluminum joints with adhesive. Mater. Sci. Eng. A 2013, **562**, 53–60.

[10] M. Fernandus, T. Senthilkumar, V. Balasubramanian, S. Rajakumar. Optimizing diffusion bonding parameters in AA6061-T6 aluminum and AZ80 magnesium alloy dissimilar joints. J. Mater. Eng. Perform. 2012, **21**, 2303–2315.

[11] J. Shang, K. Wang, Q. Zhou, D. Zhang, J. Huang, J. Ge. Effect of joining temperature on microstructure and properties of diffusion bonded Mg/Al joints. Trans. Nonferrous Met. Soc. China 2012, **22**, 1961–1966.

[12] D. Dietrich, D. Nickel, M. Krause, T. Lampke, M. Coleman, V. Randle. Formation of intermetallic phases in diffusion-welded joints of aluminium and magnesium alloys. J. Mater. Sci. 2011, **46**, 357–364.

[13] L. Liu, J. Tan, X. Liu. Reactive brazing of Al alloy to Mg alloy using zinc-based brazing alloy. Mater. Lett. 2007, **61**, 2373–2377.

[14] L. Liu, J. Tan, L. Zhao, X. Liu. The relationship between microstructure and properties of Mg/Al brazed joints using Zn filler metal. Mater. Charact. 2008, **59**, 479–483.

[15] L. Liu, L. Zhao, R. Xu. Effect of interlayer composition on the microstructure and strength of diffusion bonded Mg/Al joint. Mater Des, 2009, **30**, 4548–4551.

[16] L. Zhao, Z. Zhang. Effect of Zn alloy interlayer on interface microstructure and strength of diffusion-bonded Mg-Al joints. Scr. Mater. 2008, **58**, 283–286.

[17] Z. Wang, H. Wang, L. Liu. Study on low temperature brazing of magnesium alloy to aluminum alloy using Sn-xZn solders. Mater. Des. 2012, **39**, 14–19.

[18] L. Liu, Z. Zhang, F. Liu, Z. Wang, H. Wang. Effect of addition of Ce in Sn-30Zn solder on the structure and properties of the Mg/Al-brazed joint. J. Mater. Sci. 2013, **48**, 2030–2037.

[19] Y. Wang, G. Luo, J. Zhang, Q. Shen, L. Zhang. Microstructure and

mechanical properties of diffusion-bonded Mg-Al joints using silver film as interlayer. Mater. Sci. Eng. A 2013, **559**, 868–874.

[20] J. Zhang, G. Luo, Y. Wang, Q. Shen, L. Zhang. An investigation on diffusion bonding of aluminum and magnesium using a Ni interlayer. Mater. Lett. 2012, **83**, 189–191.

[21] R. Borrisutthekul, Y. Miyashita, Y. Mutoh. Dissimilar material laser welding between magnesium alloy AZ31B and aluminum alloy A5052-O. Sci. Technol. Adv. Mater. 2005, **6**, 199–204.

[22] J. Shang, K. Wang, Q. Zhou, D. Zhang, J. Huang, G. Li. Microstructure characteristics and mechanical properties of cold metal transfer welding Mg-Al dissimilar metals. Mater Des, 2012, **34**, 559–565.

[23] J. Wang, J. Feng, Y. Wang. Microstructure of Al-Mg dissimilar weld made by cold metal transfer MIG welding. Mater. Sci. Tech. Lond. 2008, **24**, 827–831.

[24] I. Bhamji, M. Preuss, R. Moat, P. Threadgill, A. Addison. Linear friction welding of aluminium to magnesium. Sci. Technol. Weld. Join. 2012, **17**, 368–374.

[25] H. Zhang, J. Song. Microstructural evolution of aluminum magnesium lap joints welded using MIG process with zinc foil as an interlayer. Mater. Lett. 2011, **65**, 3292–3294.

[26] F. Scherm, J. Bezold, U. Glatzel. Laser welding of Mg alloy MgAl3Zn1 (AZ31) to Al alloy AlMg3 (AA5754) using ZnAl filler material. Sci. Technol. Weld. Join. 2012, **17**, 364–367.

[27] F. Liu, Z. Zhang, L. Liu. Microstructure evolution of Al/Mg butt joints welded by gas tungsten arc with Zn filler metal. Mater. Charact.2012, **69**, 84–89.

Chapter 4 Organizational characteristics and interface strength on diffusion bonding of Mg-AZ31/Al-6061 under no pressure

4.1 Introduction

The joint easy to oxidize and produce cracks, pores and thermal stress because Mg has greater heat brittleness when welding Mg and Al dissimilar metal, which produced high hardness brittle phase in joint area easy to cause deform. It is necessary to controlled melting on both sides of weld joints simultaneously because physical properties of two kinds of difficult materials bonded are different, such as melting temperature and thermal expansion coefficients. Even if the criterion is met, it may not be possible to have an appropriate bonding when the two materials are incompatible [1]. Which may lead to a weld zone and heat affected zone microstructure without adequate mechanical strength. By means of diffusion bonding, it is possible to bond all the materials whose chemical and metallurgical properties are appropriate. In particular, the bonding of advanced materials is not possible to use classical welding methods because unexpected phase propagation at the bond interface [2]. Hence, diffusion bonding introduced convenience to the bonding of materials, which are not possible to bond by conventional welding methods. Furthermore, diffusion bonding is preferred for the materials, in which brittle phase formation is unavoidable.

Differs from welding joint, dissimilar metals diffused joint had different organizational structure and performance on interface transition zone [3]. The organizational structure directly affected the weight of diffused welding joint and the formation depended on element diffused distribution nearby diffused

interface, in which the organizational performance was comprehensive reflection of microstructure in transition zone [4]. With popularize application of electron microscopy and electron microprobe techniques, the study on organizational performance and reacted diffusion nearby interface became more thorough.

The paper adopted electronic universal testing machine and homemade fixture to detect tensile strength on Mg-AZ31/Al-6061 diffused welding joint interface under no pressure. SEM observation was used to observe and analyze microstructure of tensile fracture. According to the analysis from the fracture and tensile strength, Mg-AZ31/Al-6061 alloy fracture mechanism on welding interface was discussed under no pressure. The organizational structure and bonding state of Mg-AZ31/Al-6061 under no pressure were observed and analyzed; it was proposed that Mg-AZ31/Al-6061 could be divided according to the organization on alloy diffused interface area by SEM observation. EPMA and TEM were adopted to analyze diffused distribution of elements Mg and Al on the transition and to find the intrinsically relation between the change of organizational performance and distribution of concentration. Through control process parameter to obtain good organization and performance Mg-AZ31/Al-6061 alloy diffused welding joint and provide importance theories basis.

4.2 Organizational characteristics of the diffusion bonding interface

4.2.1 Division of diffusion interface on transition zone

Microstructure nearby the transition zone of diffusion bonding surface can reflect forming and structure, the experiment cut out bonded sample of Mg/Al dissimilar metals and prepared metallographic phase. Microstructure nearby the transition zone of diffusion bonding surface was taken by scanning electron microscopy (SEM) as shown in figure 4.1. Diffusion bonding surface of Mg/Al has obvious diffusion characteristics and the white brilliant and strip diffusion zone of new phase compound was formed between base metal of Mg and Al, in which organizational characteristics is different with both sides of the base metal [5]. It is indicated that new phase compound diffusion zone was formed with sloppy structure in the side of Mg interface transition zone, in the opposite, the new phase compound appear dense structure. Mg/Al intermetallic compound formed under the condition of heating temperature.

The forming for the transition zone of Mg-AZ31/Al-6061 diffusion bonding surface is because of occurring reaction and generating the new phase compound after solute atoms nearby phase interface reaches a certain concentration [6]. The structure is compose of independent new phase layer and includes that transition layer of the Mg side, the middle of the diffusion layer and transition layer of the near Al side. The new phase in transition layer of the Mg side had the phenomenon grow to the interface of Mg-based, while the white crystal boundary educts had also connective phenomenon with the transition layer of Mg side.

Elements Mg and Al exist nearby interface zone in diffused welding process, according to diffused welding process, Mg/Al dissimilar metals transition zone constituted of intermetallic compounds formed by diffusion.

Interface transition from left to right had different organizational form zones by three kinds of elements bonded [7]. After Mg and Al vacuum welding, micro zones were as the middle of diffused layer nearby connect interface; feature zones of the middle diffused layer, Mg and Al was transition layer closed the both sides of welding material. The bonding between the transition layer closed Al substrate and the middle diffused layer was poor and there was micro-pores. The transition zone of Mg-AZ31/Al-6061 alloy diffused welding interface was divided as shown in Fig. 4.2.
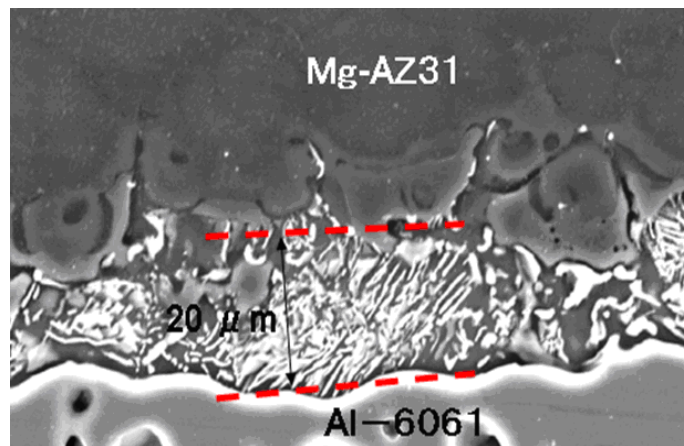
Fig.4.1 SEM image on diffused bonding transition zone
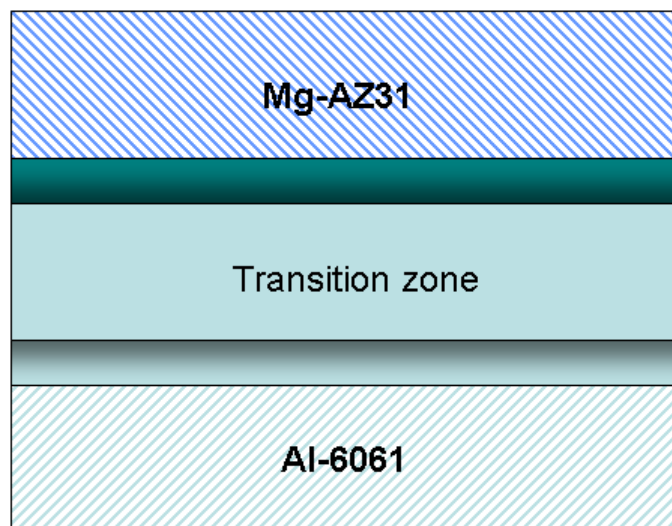
Fig. 4.2 Divided schematic diagram on diffused welding interface zone

4.2.2 XRD phase structure of diffusion interface on transition zone

In order to accurately judge the phase's structure in each diffused layers, XRD analysis was conducted for tiny part of diffused layers. Detected position as was shown in Fig. 4.3. It is results that Mg/Al intermetallic compound formed nearby transition zone of Mg/Al dissimilar metals after diffusing, namely $Mg_{17}Al_{12}$ phase. The forming of $Mg_{17}Al_{12}$ is near the one side of Mg base metal and due to Al element neared Mg base metal accompanied empty seats and replacement diffusion mechanism, so that $Mg_{17}Al_{12}$ was formed.
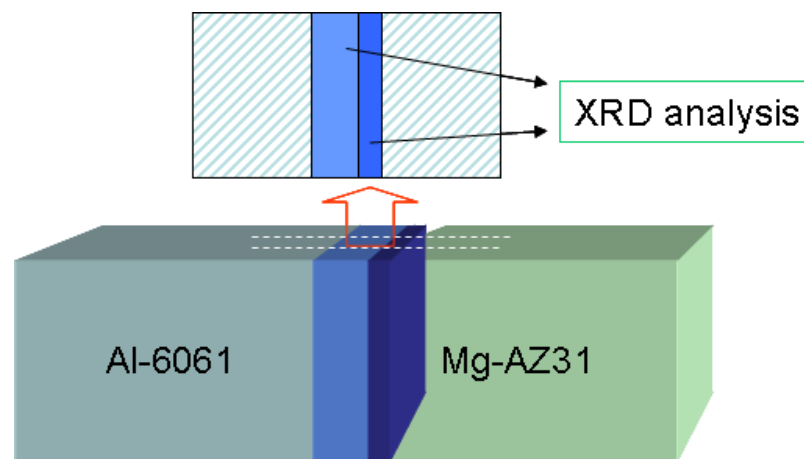
Fig. 4.3 XRD detected position of middle transited layers
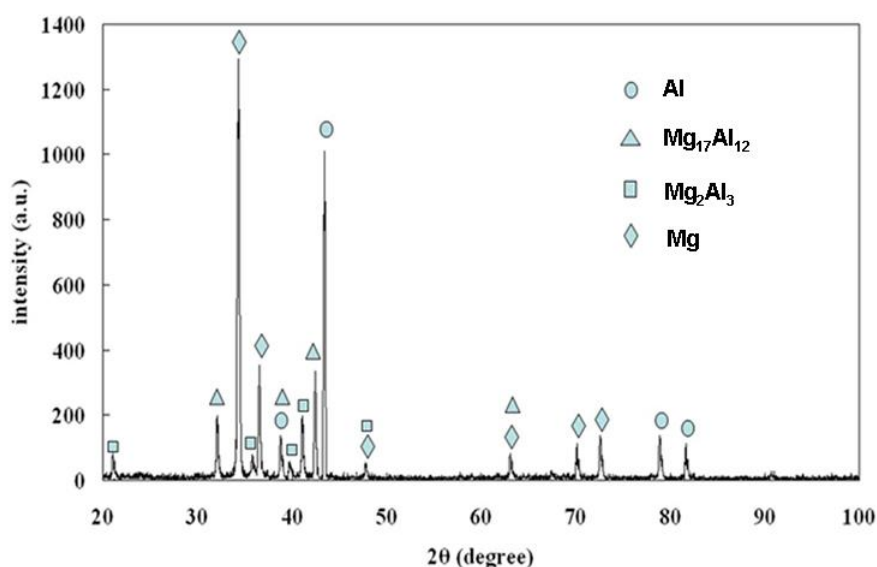
Fig. 4.4 XRD pattern of bonding interface

X-ray diffraction results showed that the transited zone phase structures were Mg_2Al_3 and $Mg_{17}Al_{12}$ phase layers in turn from joint interface Al side to Mg side. $Mg_{17}Al_{12}$ and Mg_2Al_3 belong to high hardness brittle phases. It consistence with micro hardness analysis result; the both of high hardness phases wide was narrow than Mg_2Al_3 phase layer. Mg_2Al_3 phase belong to solid-state reaction and formed the middle phase, in which the hardness and $Mg_{17}Al_{12}$ and Mg_2Al_3 phases were lower, so that helped to improve the bonding strength of Mg/Al diffused welding interface.

4.2.3 Microstructure of diffusion interface on transition zone

(1) SEM images of Mg-AZ31/Al-6061 bonding interface

Micro organizational form reflected the formation and organizational structure of the transition zone, as shown in Fig.4.5; the structure was composed of independent new phase layer included b and c transition layers of the Al-6061 side and a transition layer of the near Mg-AZ31 side. The broader region of b and c zones exists near Al-6061 side and a thinner region of a zone was observed near Mg-AZ31 side because the reaction was conducted and the new compound phase in transition layer of the Mg-AZ31 side grow to b zone of Al-6061 side and that of Al-6061 side grow to a zone of Mg-AZ31 side in the diffused process [8]. The regular strip structure was observed in a zone and the crystal structure is more density because Mg/Al/Zn alloy phase generated. In the middle of b zone, the dendrite structure is obvious, the diffusion to each other formed intermetallic compound $Mg_{17}Al_{12}$ and Mg_2Al_3 alloys phase between the both sides of Mg-AZ31/Al-6061.

The interface transition zone of Mg-AZ31/Al-6061 alloy diffused joint included that two kinds of bases atoms produced macro Migration each other under high temperature and solute atoms reach to a certain degree concentration to react generate a new phase [9]. According to driving force principle of diffused reaction, there was not coexistence region of both phases

in the binary diffused layers. Therefore, Mg-AZ31/Al-6061 alloy diffused welding interface transition was constituted of the new phase layer had independent organizational structure namely Mg side transition layer, the middle diffused layer and Al side transition layer.
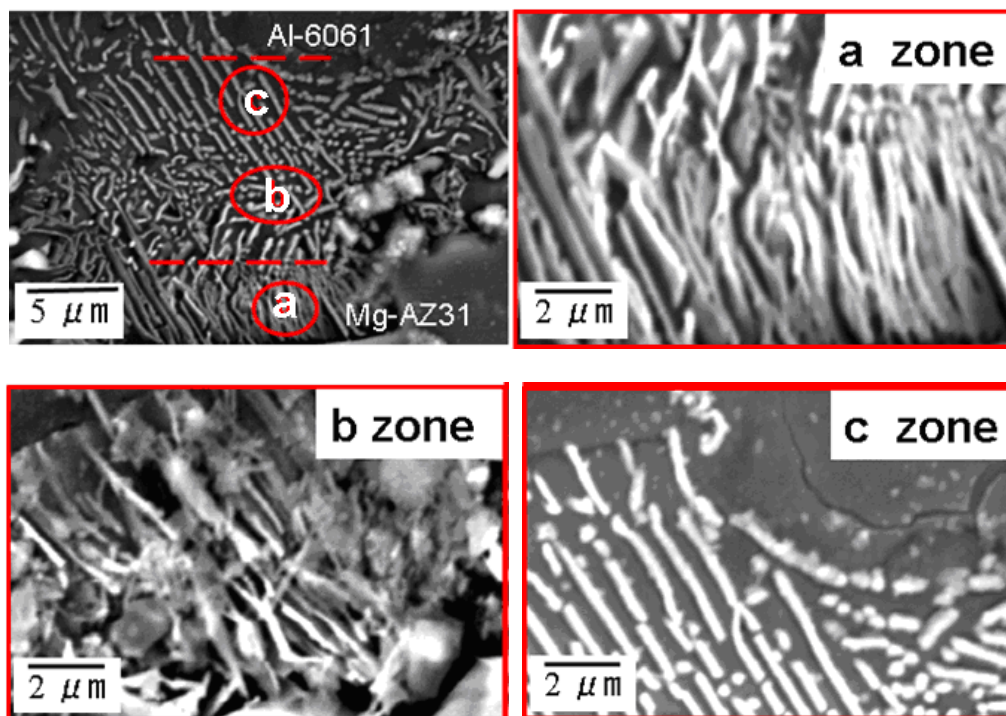
Fig. 4.5 SEM image of Mg-AZ31/Al-6061 bonding interface

(2) EPMA element distribution and EDS analyze of Mg-AZ31/Al-6061 bonding interface

The diffusion bonding interface of MgAZ31/Al6061 has obvious diffusion characteristics and the new phase compound was formed between base metal of MgAZ31 and Al6061, in which organizational characteristic is obviously on both sides of the base metal. It is indicated that a broader region of zone (I) existed near Al6061 side and a thinner region of zone (II) was observed near MgAZ31 side. Finally, the new compound phase formed nearby the both side of MgAZ31 and Al6061. The transition zone of MgAZ31/Al6061 diffused bonding layer was formed because the reaction was carried out and the new compound phase generated [10]. The structure is composed of transition layer

of the Al6061 side (I) and transition layer of the near MgAZ31 side (II). According to the microstructure observation, the density bonding structure formed due to the new phases in zone (I) in transition layer of the Al6061 side diffused to zone (II) of MgAZ31 side. It is indicated that Mg/Al intermetallic compound was obtained and what generated phases were proved by a wide range elemental mapping of EPMA and the composition analysis of EDS.

Through analyzing to the elements of areas can obtain elementary composition in the transition zone of diffusion interface. The elemental mapping in the transition zone of diffusion interface is as shown in the Figure 4.6(a). It is indicated that Mg and Al elements are mainly distributed in the transition layer and elements are clearly visible. According to the elements distribution of Mg, the content of Zn and Cu element is less and accompanies with Si. In the whole process, the element composition of Mg side contained aggregation and segregation. The transition zone of 20μm exists between Mg element and Al element [11]. The mutual diffused effect formed the transition zone. The elemental mapping shows the thicker zone easy to form Mg_2Al_3 phase because the amount of Al element is more than that of Mg nearby area (1) in Al6061 side and $Mg_{17}Al_{12}$ phase also easy to form in the thinner zone nearby area (2) in MgAZ31 side because Mg element is more. The line scan of element distribution was observed based on the elemental mapping. As shown in Figure 4.6(b), the transition layer of Mg element and Al element was clearly distinguished; the thicker zone of Mg_2Al_3 reach 16μm and the thinner zone of $Mg_{17}Al_{12}$ only is 4μm; the results consistent with elemental line scan. The Mg/Al diffused interface transition zone were formed due to the solid state diffused reaction that the atom nearby interface were excited and generated diffused migration due to the atom nearby diffused interface under lowers than the melting point temperature of the base material and the both has different diffused constants. The formation of Mg_2Al_3 and $Mg_{17}Al_{12}$ was further proved by EDS analysis that the certain ranges (3) and (4) in the thicker zone and the thinner zone were selected.
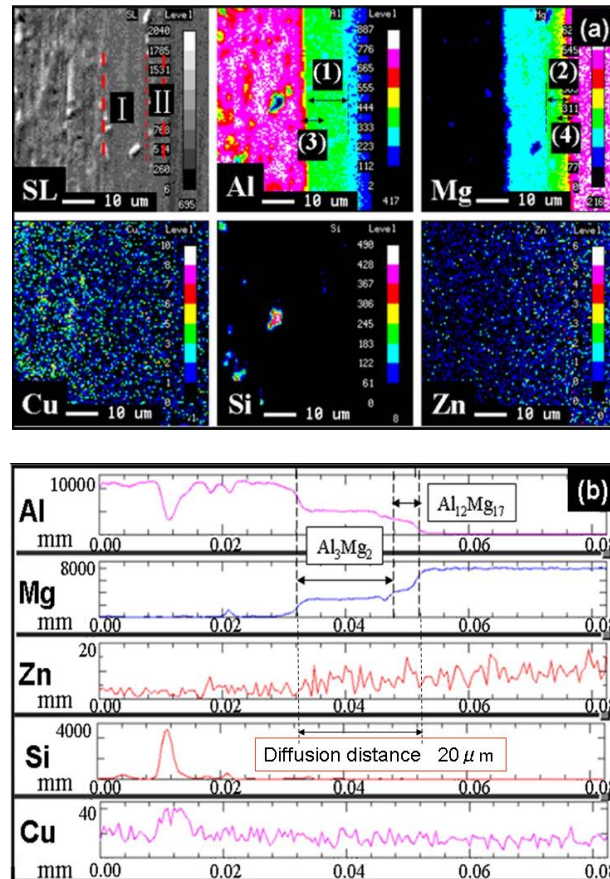
Fig.4.6 EPMA analysis for Al6061 and MgAZ31 bonding interface: elemental mapping; (b) elemental line scan.

In order to discuss diffused distance of bonding interface, EDS analysis to interface transited zone as shown in Figure 4.7, the diffused transition layers were observed by EDS analysis. It is indicated that mutually diffusion was formed. Figure 4.7(a) is the EDS analysis on the certain ranges (3) in the thicker zone from Figure 4.6(a) were determined and analyzed. Mg-Al distributed uniform in the middle of the bonding interface to achieve a better diffused effect. In the bonding layer, Mg and Al elements distributed alternately and became trading off and taking turns, so that fully spread for each other and the average mass ratio of Mg was 32% and that of Al was 55%. The distribution of Al element was uniform and the concentration was relatively higher than that of Mg element [12]. The organizational Mg_2Al_3 phase could be judged in reaction layer by the analysis of XRD. Figure 4.7(b) is the EDS

analysis on the certain ranges (4) in the thinner zone from Figure 4.6a were determined and analyzed. Mg-Al distributed uniform on the right side of the bonding interface. The average mass ratio of Mg was 48% and that of Al was 38%. The distribution of Mg element was uniform and the concentration was relatively higher than that of Al element. The organizational $Mg_{17}Al_{12}$ phase could be judged in reaction layer by the analysis of XRD and TEM. In the determined area, the mass percentage of Mg_2Al_3 and $Mg_{17}Al_{12}$ was shown in the red area and the actual value consistent with the theoretical value. The diffusion improves tenacity of binding layer, so that improved mechanical strength; high bonding dense can be achieved under no add any materials between MgAZ31and Al6061.
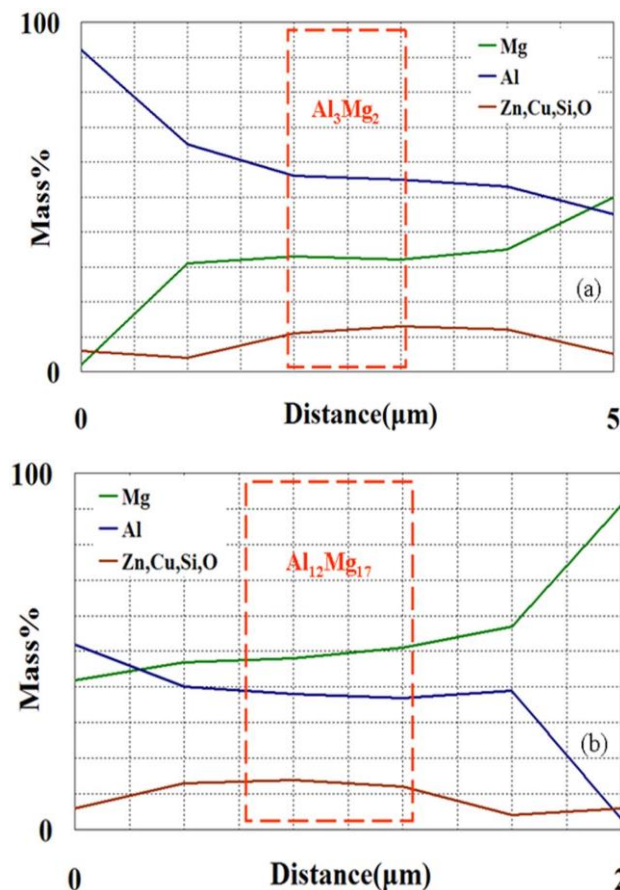
Fig. 4.7 EDS analysis of interface generated phase: (a) Mg_2Al_3 in the thicker zone; (b) $Mg_{17}Al_{12}$ in the thinner zone.

4.3 TEM observation of diffused interface on transition zone

For further study the phase structure formed in Mg/Al diffused welding interface transited zone, except adopting X-ray diffraction to qualitative analysis, transmission electron microscopy(TEM) for micro structure and the orientation relation between phase structures in Mg/Al transited zone was discussed [13]. Wire cutting form Mg side and Al side transited layers of diffused joint separately cut series sheet specimen, then the sheet was cut reduce to 50μm. By ion thinning method, the specimen was prepared and to analyze tiny structure in Mg side and Al side transited layers of Mg/Al diffused welding interface by H-800 transmission electron microscopy and constituency's electron diffraction technique.

4.3.1 Refined structure of the transition layer in magnesium side

In order to further study phase structure of the Mg-AZ31/Al-6061 transition interface zone, the fine structure near diffusion interface and position orientation relationship between phase structures was observed by TEM. The constituency's electron diffraction image and the determination about interplanar spacing of Mg/Al diffused welding joint Mg base as shown in Fig. 4.8. Mg side of diffused welding interface transited zone was mainly constituted of Mg crystal structure. the crystal face index of the hexagonal close-packed (hcp) of Mg phase structure is (102) by calibrating diffraction spots corresponding, crystal plane spacing is 0.191 nm, which close to the result of XRD standard PDF card. A large part of Mg crystal shape was rregular, but some Mg crystal grains appeared irregular organizational structure due to the affects from diffused welding craft.
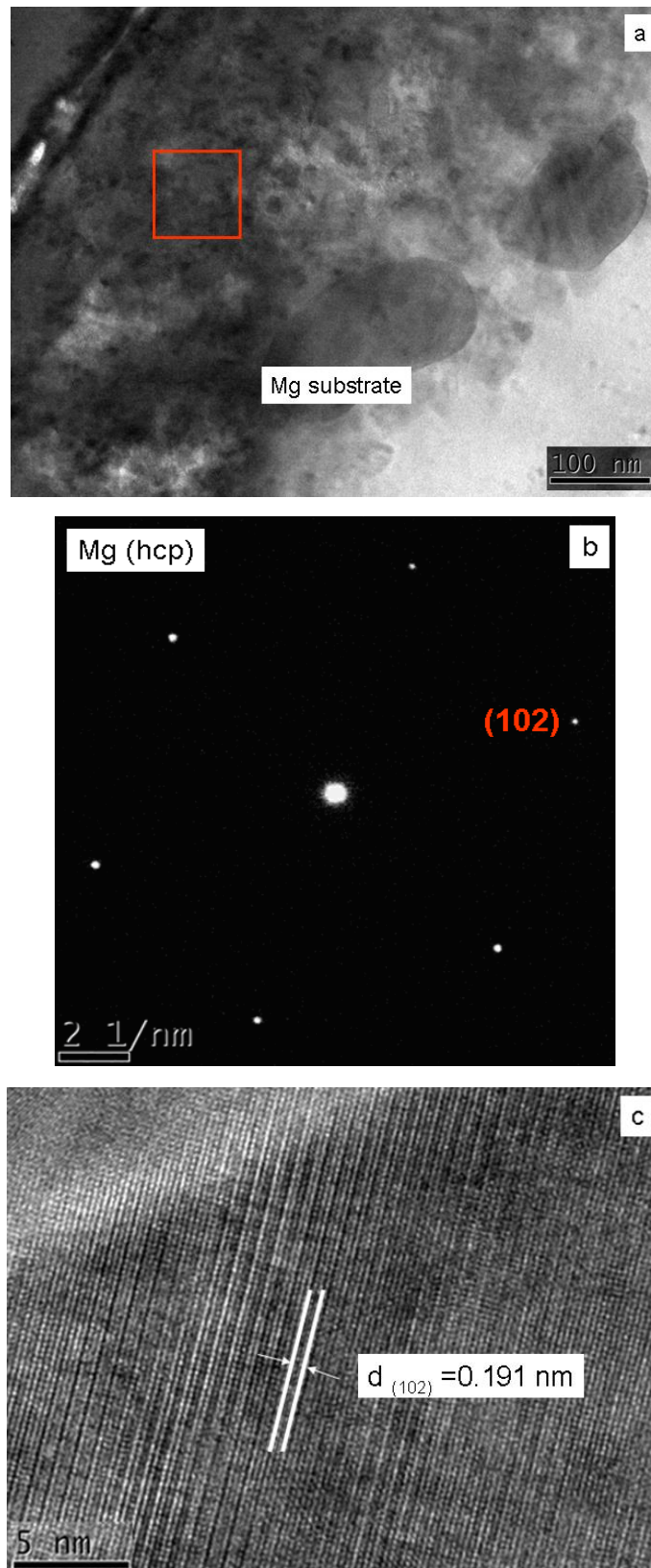
Fig.4.8 Feature of the fine structure near the Mg transition layer in the Mg/Al

diffusion bonding interface.

X-ray diffraction analysis showed that $Mg_{17}Al_{12}$ intermetallic compounds were generated in Mg side transited layer of Mg/Al diffused welding interface. Figure 4.9 showed $Mg_{17}Al_{12}$ TEM form, electron diffraction pattern and the crystal spacing determination in Mg base in Mg/Al diffused joint.

Mg transition side region is the electron diffraction diagram and the index standardization result of $Mg_{17}Al_{12}$ as shown in Fig.4.9. $Mg_{17}Al_{12}$ compounds existed near crystal boundary of Mg in form of clumps, crystal face index of the body centered cubic (bcc) of $Mg_{17}Al_{12}$ phase structure is (332) by calibrating diffraction spots, crystal plane spacing is 0.224 nm, which close to the result of XRD standard PDF card, thus further proves that $Mg_{17}Al_{12}$ presence on Mg side crystal. $Mg_{17}Al_{12}$ exists in the boundary of crystal boundary, it is indicated that Al element diffused near Mg crystal boundary to gather together and bonded with precipitation Mg in the diffusion of boundary element [14]. The result is accordance to the bonding density of Mg side in Mg/Al diffused interface on SEM image. $Mg_{17}Al_{12}$ diffusion formed intermetallic phase is closely combined with the Mg-based. A certain enhancement effect produced in the region. It dispersed distribute on Mg crystal in granular second phase because $Mg_{17}Al_{12}$ phase formed in bulk form existence near Mg crystal boundary. And it plays a role of pinning for Mg side transition layer, but also to improve the bonding strength of the diffusion interface.

4.3.2 Refined structure of the transition layer in Aluminum side

TEM observed was conducted nearby Al side transited layer for Mg/Al diffused welding. Al side transited layer structure was mainly in form of fcc structure Al substrate existing in Fig. 4.10(a), electron diffraction pattern of Al substrate as shown in Fig. 4.10(b), interplanar spacing was 0.202nm. The organization of Al substrate was fcc crystal structure, Al crystal structure produced change nearby Al side transited layers because it was affected by element diffusion.
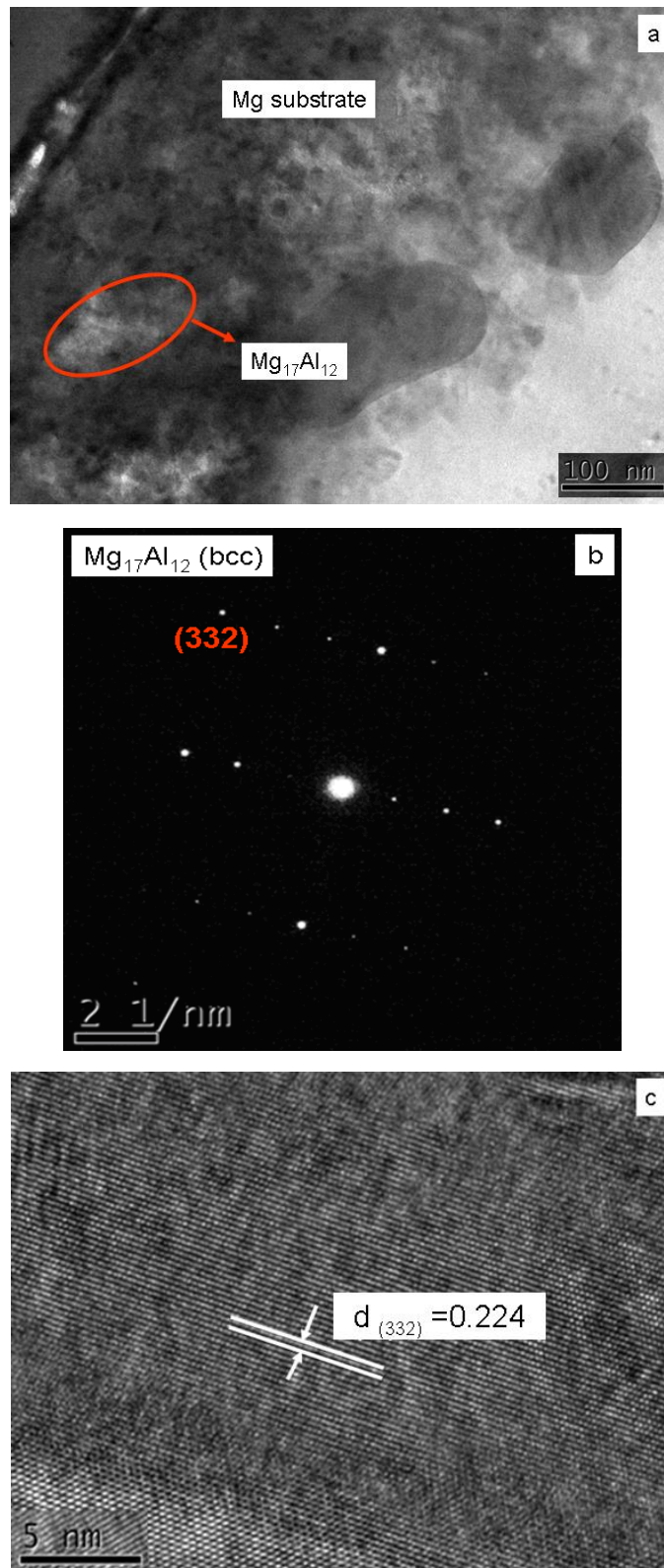
Fig.4.9 Feature of the fine structure near the Mg transition layer ($Mg_{17}Al_{12}$

phase) in the Mg/Al diffused bonding interface.
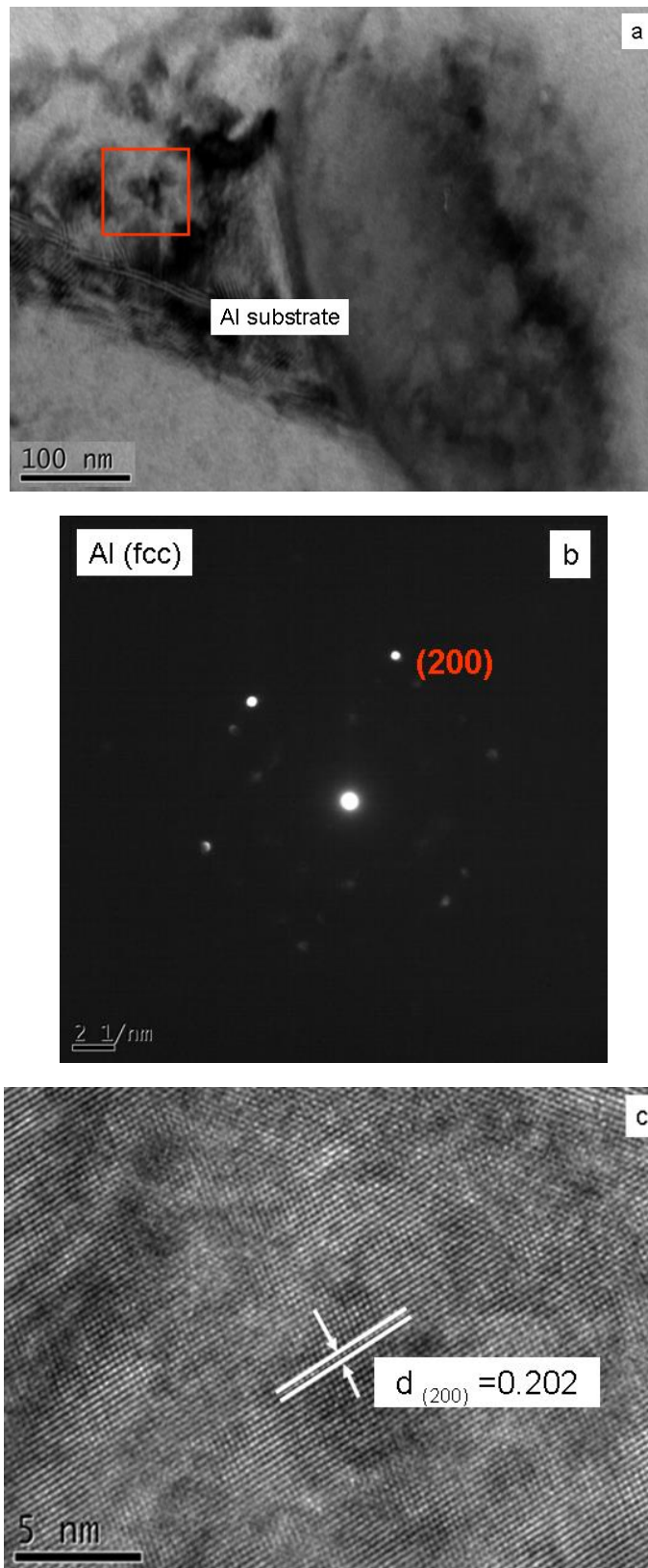
Fig.4.10 Feature of the fine structure near the Al transition layer in the Mg/Al diffused bonding interface.

Fig.4.11 shows that TEM electron diffraction figure and index of phase calibration results of Mg_2Al_3 educts in Al side transition layer. There are granular body centered cubic (fcc) of the structure of the Mg_2Al_3 precipitation phase in this area, in which crystal index are （113）. Interplanar spacing crystal interface（113）is 0.213nm. Mg_2Al_3 precipitated phase mainly distribute Al-based, compound of precipitate out was formed in diffused heating process.
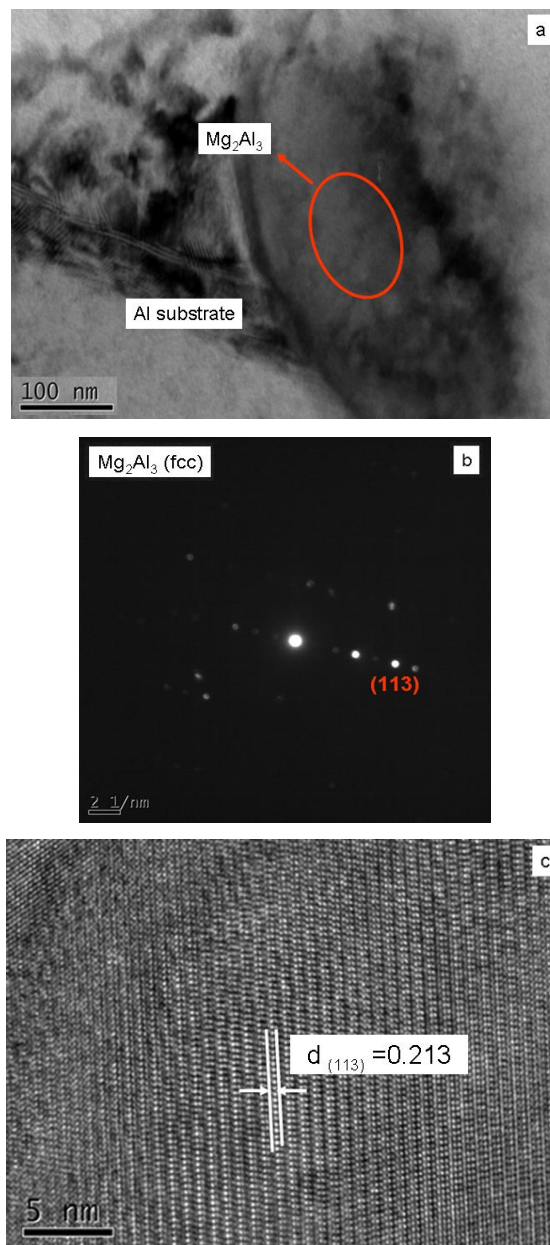
Fig.4.11 Feature of the fine structure near the Al transition layer (Mg_2Al_3 phase) in the Mg/Al diffused bonding interface.

4.4 Analysis of optimized conditions on diffusion layer between magnesium AZ31 and aluminum 6061 alloys

4.4.1 Effect of bonding temperature on microstructure of welding interface and diffused layer hardness

With bonding temperature increasing, the microstructure on interface would change obviously. As shown in Fig.4.12, it is sufficient evident that the microstructure produced change on the interface and the size of intermetallic compound increases with bonding temperature increasing. As shown in Fig. 4.12(a), Mg_2Al_3 alloy phase in diffused layer was loose at 430°C, in which a small $Mg_{17}Al_{12}$ intermetallic compound phase formed close to Mg side due to insufficient thermal excitation and lead to diffuse was no sufficient. Eutectic temperature was not reached at low temperature [15]. The flow ability of metal was brought out. The base materials still remain respective features, which leads to an incomplete coalescence of the bonding interfaces. Moreover, the grain boundary surface tension and grain boundary mobility are less at low temperatures which controls the initial movement of interface grain boundaries.

When temperature reaches to 440°C, Mg_2Al_3 alloy phase became more density in diffused layer and an amount of $Mg_{17}Al_{12}$ intermetallic compound phase generated as shown in Fig. 4.12(c). In particular, the size of $Mg_{17}Al_{12}$ intermetallic compound increased obviously. Higher temperature improves the contact ratio because the atom diffused ability is higher with higher temperature, so that leads to effective bonding. The hardness of the joint decreases with heating temperature increasing, which leads to larger interfacial deformation and hence the atom diffusivity increases, so that resulting in easy to diffuse and chemical bonding was speeded up.

The temperature was up to 450°C leads to the alloy phase in diffused layer

became coarse as shown in Fig. 4.12(e), the size of $Mg_{17}Al_{12}$ intermetallic compound increased obviously and formed brittleness phase layer in Mg side because increasing temperature generally promoted mass transfer of alloy elements diffused to the interface, volume fraction of the reaction products as embrittlement phase causes joints become embrittle. However, plastic deformation of the bonding interface asperities leads to intimate contact, which counter balances the embrittlement phenomena due to intermetallic phases. Diffused coefficient causes large amount of intermetallic compound, which leads to increasing of brittleness on the joint and did not help to obtain good joint.

The hardness distributions of diffusion bonded with different heating temperature were shown in Fig. 4.12(b,d,f), it reveals the effect of bonding temperature on interface hardness of diffusion bonded Mg-Al dissimilar joints. According to hardness distribute on interface, the following inferences can be obtained: hardness value was increasing with bonding temperature; the hardness in middle diffused layer was higher far and away the both sides of basal body. The highest hardness in the intrmetallic compounds layer was 250 Hv at a bonding temperature of 450°C. Hardness could be increased long with bonding temperature due to the formation of intermetallic compounds on the interface. The intermetallic compounds once connect and thickness grows, the hardness was changed into brittleness. So, the plasticity and strength of joints will be decreased obviously. Because the diffused rate for Al atoms is much higher than that of Mg atoms at high temperature, excess Al atoms diffuses across the interface into the magnesium side and forms high hardness brittleness layer, so that cause the performance of the joint reduced. Therefore, bonding temperature affected the organization and hardness on interface, it is necessary that the control for bonding temperature to improve the performance of the joint. The most optimized bonding temperature was 440°C.
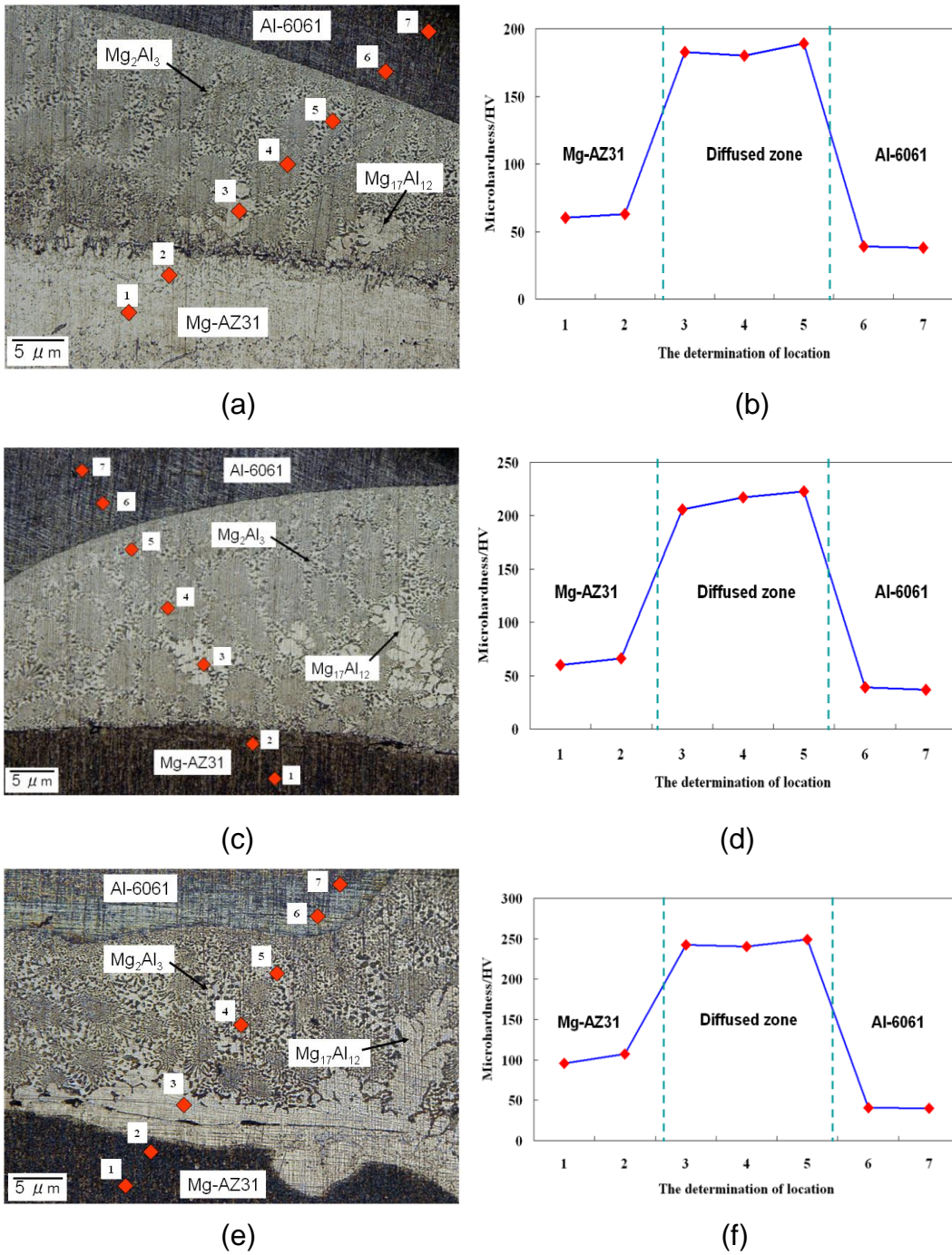
Fig.4.12. Microstructure and hardness on interface under different bonding temperature: (a) Microstructure on interface at 430°C; (b) Hardness on interface at 430°C; (c) Microstructure on interface at 440°C; (d) Hardness on interface at 440°C; (e) Microstructure on interface at 450°C; (f) Hardness on interface at 450°C.

4.4.2 Effect of holding time on intermetallic compound layer

After confirming optimum bonding temperature was 440°C, effect of holding time on intermetallic compound diffused layer was discussed and the most suitable holding time was confirmed by elemental distribution and diffused distance on bonding interface under different holding time of 20min, 60min and 90min.

The obvious transited zone produced on diffused welding joint interface of Mg-AZ31/Al-6061 alloy. As shown in Fig. 4.13(a), the face and line composition distribution of Mg-AZ31/Al-6061 was observed after the holding time was 20min. Surface elementary distribution in the transition zone is shown that elements Mg and Al are mainly distributed in the diffused layer. The line analysis is shown that the diffused distance was 5μm. The diffusion of element Mg and Al could be observed and was distributed each other separately between Mg side and Al side [16]. Whose strength on joint was about 44MPa due to the holding time was short lead to the diffusion was not fully and bonding strength was not high.

Elemental face and line analysis about diffused welding interface of Mg-AZ31/Al-6061 were conducted under the condition that the holding time was 60min. As shown in Fig. 4.14(b). The mutual diffused effect formed the transition zone. The elemental surface analysis showed the thicker zone easy to form Mg_2Al_3 phase because the amount of Al element is more than that of Mg nearby area (1) in Al6061 side and $Mg_{17}Al_{12}$ phase also easy to form in the thinner zone nearby area (2) in MgAZ31 side because Mg element is more. The line scan of element distribution was observed based on the elemental face analysis. Mg/Al diffused interface were formed due to the solid state diffused reaction that the atoms nearby interface were excited and generated diffused migration due to the atom nearby diffused interface under lowers than the melting point temperature of the base material and the both has different diffused constants. The appropriate holding time was conducive to improve the

strength of the joint. The strength reached maximum value about 110MPa under holding time 60min.

Elemental surface and line analysis of Mg-AZ31/Al-6061diffused bonding interface was conducted under holding time 90min. As shown in Fig. 4.15(c), Surface elementary distribution shown that Mg and Al elementary are mainly distributed in interface zone and transition layer. Line distribution showed that the transition zone of 30μm exists between elements Mg element and Al because the holding time was too long and element diffusion was fully, so that caused diffused interface was not uniform and generated more widely brittleness phases alloy layers. Which affected joint strength reduces to about 62MPa.
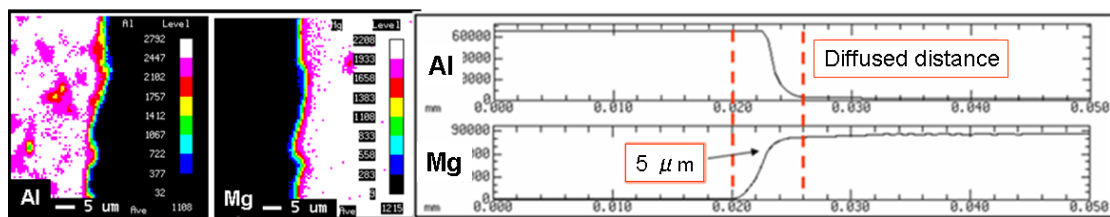
(a)
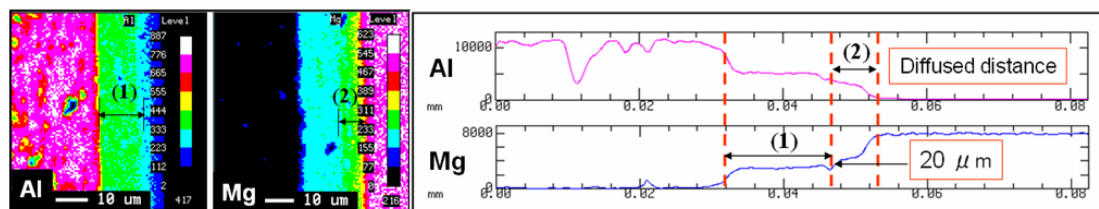
(b)
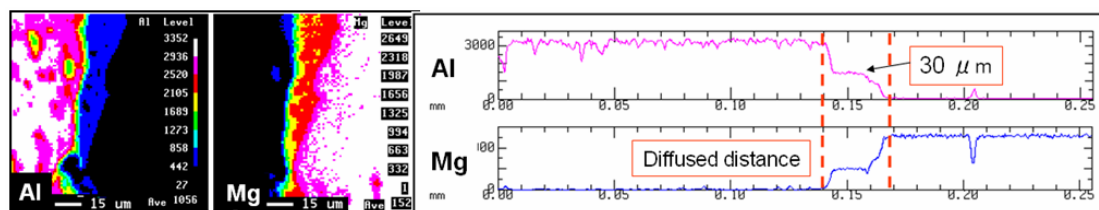
(c)

Fig.4.15. Elemental distribution and diffused distance of intermetallic compound layer under different holding time: (a) Holding time for 20min; (b) Holding time for 60min; (c) Holding time for 90min.

4.5 Diffusion bonding strength of the Mg-AZ31/Al-6061 joint

4.5.1 Tensile strength of diffusion joint under no pressure

Welding process parameter directly affected bonding features of diffused interface, so that bonding strength, fracture position and fracture form were confirmed on diffused interface. In order to research bonding strength on diffused welding interface, CMTS150 micro-controlled electronic universal testing tensile machine was adopted to get tensile strength of Mg-AZ31/Al-6061 alloy diffused interface by using different process parameters. The size of tensile specimen is as shown in Fig. 4.16.
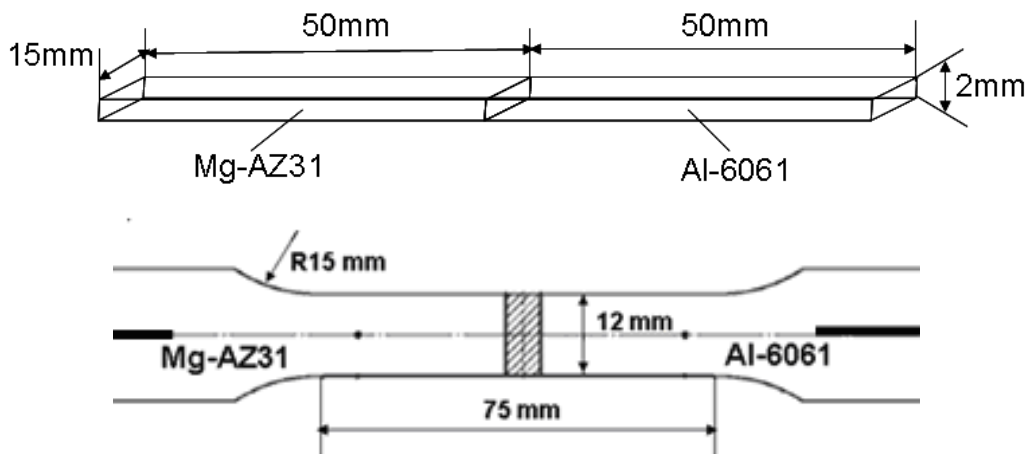
Fig.4.16 Size of tensile specimen.

The joint of Mg-AZ31/Al-6061 alloy diffused welding was obtained under different process parameters, according to ISO6898-2 standard; the specimen was processed to ultimate tensile strength of standard size in Fig. 4.16. (Tensile strength of each process parameters got an average of 3 specimens as standard). The tensile strength and calculated results on diffused welding interface under no pressure are as shown in table 4.1.

Table 4.1 Experimental and calculation results on the tensile strength of Mg/Al diffusion bonding interface.

Number	Bonding temperature	Holding time	strength	Average strength
No.1	420°C	60 min	40MPa	44MPa
No.2			48MPa	
No.3	430 °C	60 min	59MPa	68MPa
No.4			77MPa	
No.5	440 °C	60 min	120MPa	110MPa
No.6			100MPa	
No.7	450 °C	60 min	82MPa	75MPa
No.8			68MPa	

A large number of experiments indicated above eutectic temperature 440°C as experimental connected temperature was most suitable. As shown in Fig. 4.17, the connected temperature was 440°C and the holding time was 60min, under different cooling rate, the different change strength of Mg-AZ31/Al-6061 alloy with no pressure was formed. As shown in Fig. 4.17, the tensile strength at the interface is 110 MPa under the temperature heated up to 440°C and the holding time is 60 minutes, the cooling rate was 10°C/min. Under the same heating condition, the different cooling rate was set to conduct cooling by air cooling and water cooling. The tensile experiment showed the results of tensile strength respectively were 66MPa and 47MPa by two kinds of cooling methods. The results less than the tensile strength under constant rate cooling at 10°C/min. The air cooling rate was uneven lead to the specimen uneven heated under cooling process and easy to cause produce holes, so that the strength was low. When water cooling was used, the bonding specimen easy produced embitterment and reduced the bonding strength due

to the rapid cooling. It is shown that holding constant cooling rate played an important role for obtaining the high strength joint.
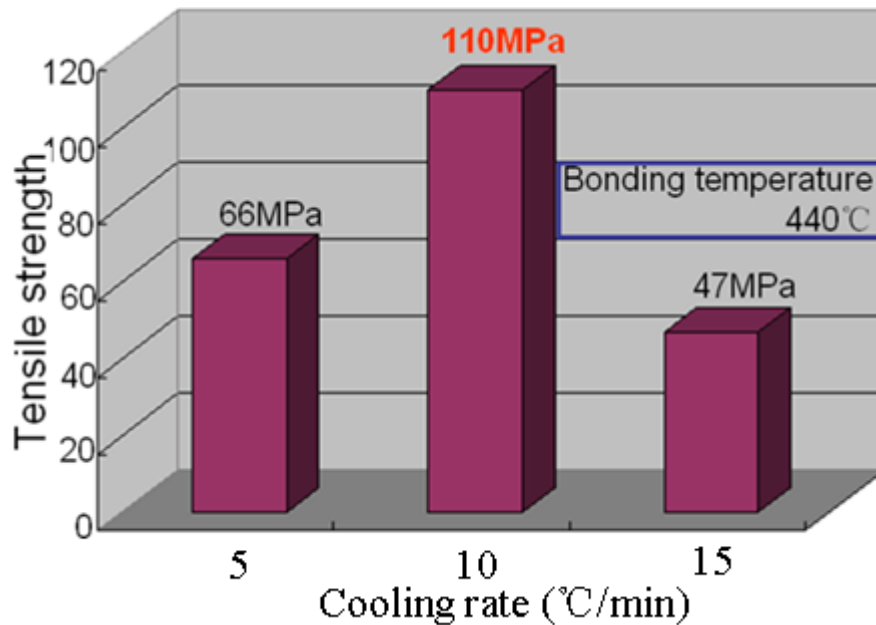
Fig 4.17 Tensile strength under cooling rate.

4.5.2 Influences on different process parameters to joint strength

(1) Effect of Bonding Temperature on Shear Strength and Bonding Strength

Surface conditions also change with temperature. The asperities deform at higher temperature providing yielding. It is evident from Fig.4.18 that bonding strength is increasing with increasing bonding temperature. At a low temperature of 400°C, the shear strength and bond strength of the diffusion-bonded joint are low. This is due to poor contact of the bonded surface and insufficient thermal excitation. The flow ability of metal is substantial at low temperature, yet yields strength of the base materials still remains high, which leads to an incomplete coalescence of the mating surfaces. Moreover, the grain boundary surface tension and grain boundary mobility are less at low temperatures which controls the initial movement of interface grain boundaries.

When temperature reaches to 420°C, it results in a considerable

improvement in bonding strength. Higher temperature improves the contact ratio, because the atom diffusion is higher with higher temperature leads to effective bonding. At a bonding temperature of 460°C, maximum shear strength of 49 MPa and a bonding strength of 69 MPa are obtained. With increase in temperature, the yield strength of the joint decreases, which leads to larger interfacial deformation and hence the atom diffusivity increases, resulting in easier and speeder chemical bonding. As in the initial stages of bonding at high temperatures, migration of interface grain boundaries was involved as above, the higher rate of grain growth would lead to rapid removal of evidence of the bond line and increases the strength nearer to the pare

nt metal.

Table 4.2 Experimental and calculation results on the tensile strength of Mg/Al diffusion bonding interface.

Number	Bonding temperature	Holding time	Strength	Average strength
No.1			40MPa	
	420°C	60 min		44MPa
No.2			48MPa	
No.3			59MPa	
	430°C	60 min		68MPa
No.4			77MPa	
No.5			120MPa	
	440°C	60 min		110MPa
No.6			100MPa	
No.7			82MPa	
	450°C	60 min		75MPa
No.8			68MPa	

Further increase in temperature to 480°C leads to reduction in strength, because increase in temperature generally promotes mass transfer of alloying elements across the interface, which is responsible for the increase in volume fraction of the reaction products Mg_2Al_3 cause more embrittlement of joints.

However, plastic collapse of the mating surface asperities leads to intimate contact, which counter balances the embrittlement phenomena due to intermetallic phases. Higher rate of diffusion causes higher amount of intermetallic compound formation, which leads to increase in brittleness of the joint and decrease in joint strength.

(2) Effect of Holding Time on Bonding Strength

From Fig. 4.18 it can be observed that the bonding strength of the joints was increasing with increase in holding time, irrespective of temperature and pressure. High bonding strength is obtained at a holding time of 70 min. This is mainly because the holding time has an effect on the creep of the protrusions and the quantity of atomic diffusion. The strength is increasing more rapidly with increase in holding time from 10 to 70 min and then it decreases sharply. Longer holding times show a continuing grain growth accompanied by a small increase in specific strength. At 90 min of holding time, a sharp decrease in strength was attributed due to the growth of intermetallic compounds. The thickness of the intermetallic compound increases remarkably with holding time and the strength of the bond decreases. Lower shear strength and bonding strength of 31 and 51 MPa are obtained at a holding time of 10 min. It is evident that the lower holding time led to the weak bonds and this may be due to insufficient time allowed for the diffusion of atoms across the bond interface from the mating surfaces.

It is generally considered that a sound bond has been obtained when there is no metallographic evidence of the bond line in the interface. However, contamination in surfaces to be joined is often unavoidable in real bonding situations. Therefore, neither an interface-free bond nor the strength of the bond is problematic. It is known that the bond quality was basically dependent on the extent of removal of the initial bond interface. The mechanism(s) by which the bond interfaces eliminated is that recrystallization which was initiated in the bond region caused the elimination of the bond interface and led

to high bond strengths. Increase in bonding temperature will speed up grain boundary re-crystallization and grain growth. The elimination of bond interface based on the temperature, time dependent, grain growth, and on the bond microstructures, it is reasonable to conclude that grain growth is an important process in the removal of the initial bond interface leading to full bonding.
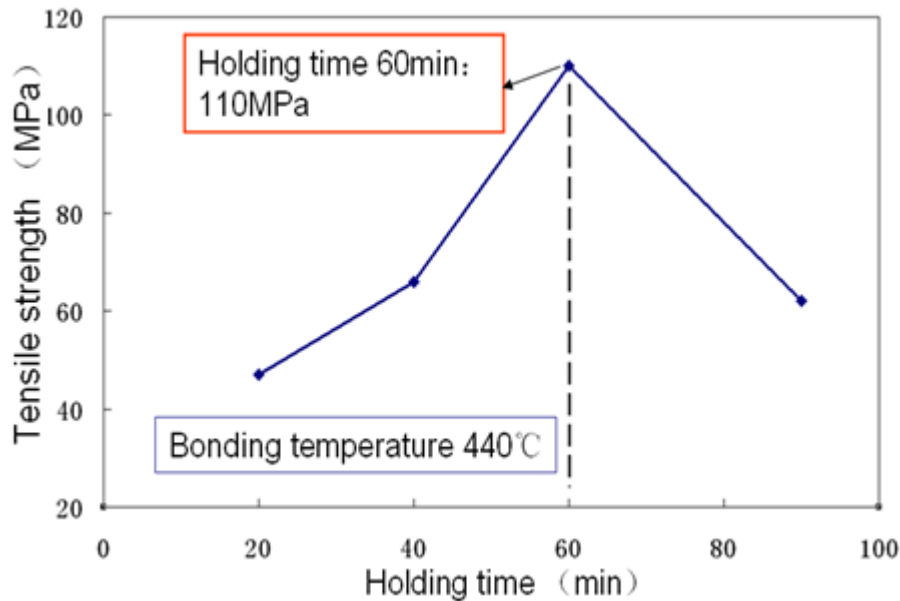
Fig. 4.18 Related curves of holding time and bonding strength.

The tensile strength on Mg-AZ31/Al-6061 alloy diffused welding interface showed that the temperature range from 400°C to 460°C, holding time 20-90min under no pressure and no macroscopic deformation the tightly bonding and high bonding strength joint was obtained. With heating temperature, the tensile strength appeared tend to increase and then to reduce. When constant temperature was held, the shear strength on joint was also increased with expanding time. Therefore, appropriate diffused process parameter could get the joint that the bonding strength meets the need of Mg-AZ31/Al-6061 alloy welding joint.

4.6 Mg-AZ31/Al-6061 diffusion joint fracture and fracture analysis

4.6.1 SEM analysis of the joint fracture

After Mg-AZ31/Al-6061 was welded, diffused zone was formed on joint interface due to atoms Mg and Al inter-diffused lead to a key effect on the bonding state and fracture form for the joint performance produced. Through scanning electron SEM observed for shear fracture. Fracture form of Mg-AZ31/Al-6061 alloy diffused joint as shown in Fig. 4.19 and Fig. 4.20. Macro-fracture of diffused welding joint on Mg-AZ31 and Al-6061 was mainly to emerge white and accompanied dark gray area. Silver section is tissue residue of interface zone which appeared fine texture dendrites' structure; the dark gray areas were fracture organization of interface diffused bonding area on Mg-AZ31 and Al-6061 sides.

Mg heat brittleness had greater effects on fracture form diffused behavior to the joint nearby Mg side fracture. Intergranular crack existed in Mg side fracture. As shown in Fig. 4.19(a), the cracks appear obvious cracking form due to Mg heat brittleness in the diffused welding heating. Intergranular cracks had obvious layer distribution, under welding conditions; the joint fracture appeared quasi-cleavage cracks and intergranular cracks because Mg side was affected by element diffusion, dislocation and base material heat brittleness. As shown in Fig. 4.19(b), Mg side fracture not easy to produce quasi-cleavage feature, the scattered distribution intermetallic compounds was convex state which had a certain layer or stepped shape quasi-cleavage form on the fracture surface under diffused welding condition. The second cracks produced between layer convex, and some tiny expanding cracks appeared around the main cracks and the phenomenon not conducive to improve bonding performance on joint.
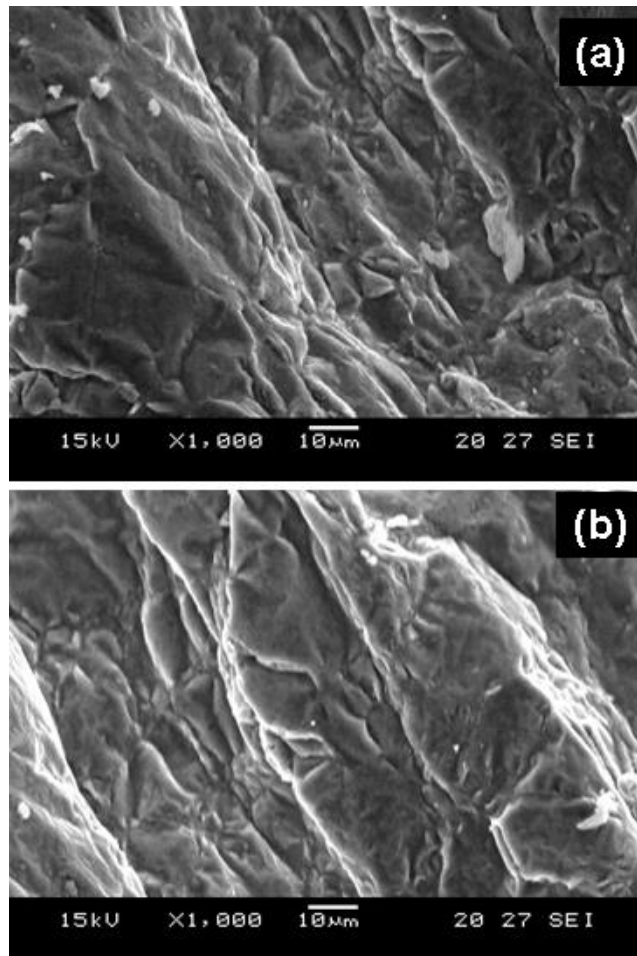
Fig.4.19. SEM microstructure at the edge fracture of the bonding of Mg-AZ31 and Al-6061(Mg) side: (a) Fracture of a long grain boundary (b) Secondary crack.

Fracture form on Mg-AZ31/Al-6061 alloy diffused joint was as shown in Fig. 4.20, due to ductility and toughness of Al surpassed to Mg and there was not heat brittleness. Mg-AZ31/Al-6061 alloy diffused welding heating temperature was lower and Al belong to face-centered cubic(fcc) material, therefore, Al side fracture produced low temperature cleavage form. As shown in Fig. 4.20(a), white convex substance appeared nearby mixed fracture zone. It is possibly that organizational constitute of interface zone formed by diffusing element. Typical cleavage fracture form as shown in Fig. 4.20, a small of

plastic zones on interchange of cleavage stages; plastic fracture zone and cleavage formed certain layer topography. Observation and analysis of Al side fracture indicated that Al side fracture was the fracture foam had small plastic pit and mixed fracture form due to cleavage.
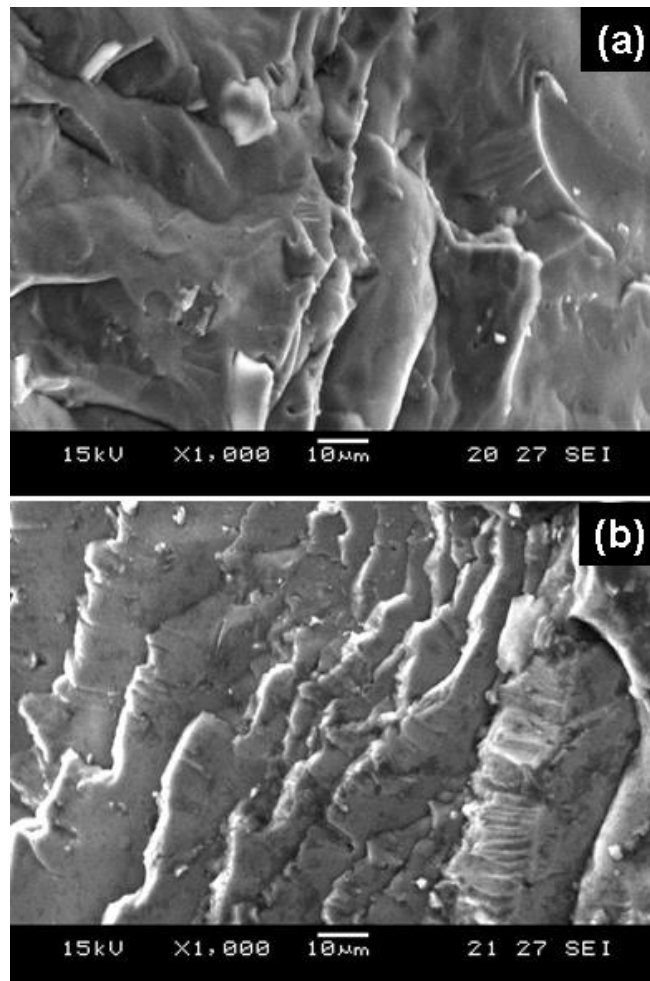
Fig.4.20. SEM microstructure at the edge fracture of the bonding of Mg-AZ31 and Al-6061 (Al side): (a) mixed fracture zone; (b) cleavage fracture zone.

4.6.2 Fracture analysis on diffused interface

The fracture mechanism Mg-AZ31/Al-6061 alloy diffused welding joint was complex due to which was affected by various factors. For example, residual inclusions hinted atomic diffusion in welding process because the surface had

not been thoroughly treated before welding and Mg and Al easy to be oxidized caused the atoms diffusion was hinted, so that diffusion was not fully and formed mechanical bonding in any zones. It is mainly reason lead joint to fracture. But tensile test result about diffused joint showed that the fracture position of Mg-AZ31/Al-6061 alloy should be confirm nearby diffused zone.

Fracture nearby interface diffused zone, the particles distributed nearby the fracture expressed laminar fracture characteristics and the growth direction of micro cracks in particles interior and fracture direction were perpendicular. The phenomenon significantly inhibited effect for expansion of secondary cracks from the distribution direction of micro cracks. It is indicated that the produce and expansion micro cracks with itself whether produce the related structure defects. With the increase of the load, the tensile stress in the precipitation particles is gradually increased. When the concentration degree of the precipitation phase and the stress on the substrate interface exceeded can withstand tensile stress of the precipitation phase particles, the fracture produce and the cracks rapidly expand to the internal of the particles and rapidly throughout the whole grain. The micro cracks not only could form separately, but also the several could be formed at same time; the fracture characteristics can provide more channels for the crack; Mg-Al alloy phase in the form of a small early-phase was precipitated on the surface of interface. The defects in the internal structure were corresponding reduced. In addition, the part of stress state was simple in the stretching process could be approximated to bear only two-dimensional tensile stress. According to Griffith's theory, Mg-Al eutectic phase can withstand tensile stress and as shown in follows:

$$\sigma_f = (\frac{2E\gamma}{\pi C})^{\frac{1}{2}} \qquad (4\text{-}1)$$

The γ is surface fracture energy; E is modulus of elasticity; C is the length of micro-cracks in particles. It is shown that the eutectic phase particles existence internal defects could withstand tensile stress was low compare with no defect eutectic phase. Therefore, the kind of eutectic phase particles preferentially fracture under the same external force. To sum up, the fracture of the eutectic phase particles in the alloy not only had relation with the morphology, the size and distribution, but also depending on whether exists the structural defect within the particles.

The inner of the tensile specimens only produced perpendicular to the transverse cracks in the stress direction. Under the case that did not contact with other brittle phase, the cracks were resulted in the accumulation and passivity on the interface after the cracks extended to interface with the substrate because the hindered substrate had high plasticity. With tensile stress further increasing, the cracks extended along the grain boundaries and growing and continues to grow up connected together, so that Mg-Al alloy phase to fracture and peel off from the substrate eventually.

4.6.3 Fracture process of diffused interface

Tensile fracture of Mg-AZ31/Al-6061 alloy diffused welding interface as shown in Fig. 4.21, Figure 4.21(a) showed that organizational state in interface zone without conducted tensile test, some micro-pores and cracks produced nearby Al side, when tensile stress start, internal crystal boundaries produced tensile deformation in microstructure the middle of position. So deformed stages formed and produced void coalescence.

As shown in Fig. 4.21(c), when the phenomenon gathered to a certain degree, the crack source formed due to the affect from tensile movement and gradually expansion. At the same time, interface diffused zone original micro-cracks nearby Al side extended into the middle of diffused zone and made the cracks mainly gathered in diffused zone nearby Al side. With tensile

stress increase, relative displacement between crystals boundaries became large, void coalescence was more obviously and dislocation accumulation was more. It caused the cracks extended to base material long to crystal boundaries, phase boundaries and impurities had still cracks and micro- pores formed with Al side extended and connected to produce separate nearby Al side, so that formed micro interval. With tensile stress continuing increase, the cracks constantly extended and micro interval wide increase, finally, diffused welding interface produced cracking.
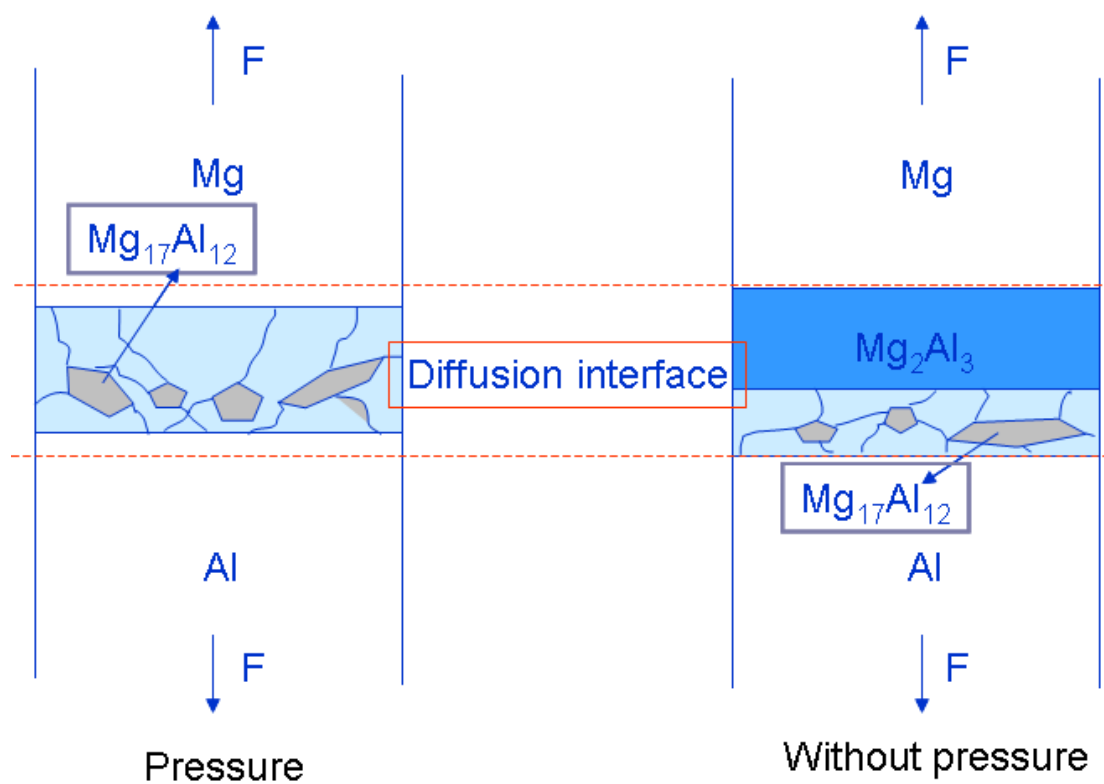
Fig. 4.21 Schematic diagram of Mg-AZ31/Al-6061 alloy diffused welding interface fracture process.

4.7 Comparing Mg/Al diffused bonding under pressure and no pressure

The joint formed process existed an obvious different due to Mg/Al alloy adopted different equipment under pressure and not pressure. Therefore, the organizational performance and phase structure of joint welding zone had also greater different.

(l) Bonding craft.

When Mg/Al alloy diffused welding, the meet for the joint about surface finish was high. In order to obtain interface diffused fully joint, oxide film was required to get rid from the surface of base material. After assembling, setting craft parameters were used to conduct welding. Under vacuum and no pressure conditions, Mg and Al base materials kept solid status could avoid heating uneven phenomenon, so that diffused welding joint interface bonding was very rules and beautiful. Adjusting heating temperature and pressure reduced the temperature interregional from Mg heat brittleness under pressure condition. But the joint strength was not high due to the pressure role caused interface organization product deform.

(2) Organizational performance in welding zone

Formed interface transited zone by Mg and Al atom diffused and reacted each other on joint interface when Mg/Al was welded under no pressure. It was constituted of Mg side transited layer, middle diffused layer and Al side transited layer. Base materials micro organization did appear obviously change after welding between both sides of interface transited zone and there was not fusion phenomenon. The joints depend on Mg and Al atom diffused to conduct effectively connection. Under pressure condition, the bonding interface was affected by pressure; diffused zone from molten crystal zone and semi-molten crystal zone was composed.

(3) Welding zone phase structure

$Mg_{17}Al_{12}$ phase existed in interface transited zone under no pressure due to based materials as Mg and Al element composition and no adding middle alloy layers. Under no pressure condition, the boundary between each phase was more clearly with the change of elemental concentration had certain regularity. While the change of diffused craft parameters to the effect of each phase diffused distance in joint interface transited zone was obviously.

To sum up, well bonding could be obtained through adopting vacuum diffused welding craft to Mg/Al alloy. Therefore, diffused bonding under no pressure was more suitable for developing Mg/Al alloy welding.

4.8 Concluding remarks

(1) The result of diffused welding interface tensile strength indicated that the maximum shear strength was 110MPa under 440℃. Holding time and cooling rate process parameters from bonding strength produced affects.

(2) EPMA analysis results of Mg/Al dissimilar metals on diffused interface transited zone indicated that relatively independent concentration distributed zone generated on diffused welding interface transited zone. With diffused temperature increasing, the wide was generally increasing and the interface distribution was not uniform under long holding time.

(3) X-ray diffraction showed that $Mg_{17}Al_{12}$ and Mg_2Al_3 alloy phases formed the diffusion of elements Mg and Al nearby Mg/Al diffused welding interface. Interface transited zone phase structure from Mg side to Al side was constituted of $Mg_{17}Al_{12}$ and Mg_2Al_3 in turn.

(4) The change of crystal grain growth was analyzed by microstructure observation and the optimum diffused distance was 20μm; it is showed that the hardness of diffused alloy phase changed from 250HV to 180HV. The maximum value reached 110MPa.

References

[1] J. Grum and J.M. Slabe, The Use of Factorial Design and Response Surface Methodology for Fast Determination of Optimal Heat Treatment Conditions of Different Ni–Co–Mo Surfaced Layers, J. Mater. Process. Technol, 2004, **155–156**, 2026–2032.

[2] V. Gunaraj and N. Murugan, Application of Response Surface Methodology for Predicting Weld Bead Quality in Submerged Arc Welding of Pipes, J. Mater. Process. Technol, 1999, **88**, 266–275.

[3] K. Manonmani, N. Murugan, and G. Buvanasekaran, Effect of Process Parameters on the Weld Bead Geometry of Laser Beam Welded Stainless Steel Sheets, Int. J. Join. Mater, 2005, **17**(4), 103–109.

[4] G. Cochran, M. Cox, Experimental Design, 2nd ed., Asia Publishing House, New Delhi, 1962.

[5] M. Balasubramanian, V. Jayabalan, and V. Balasubramanian, A Mathematical Model to Predict Impact Toughness of Pulsed Current Gas Tungsten Arc Welded Titanium Alloy, Int. J. Adv. Manuf. Technol, 2008, **35**(9–10), 852–858.

[6] S. Kumar, P. Kumar, and H.S. Shan, Effect of Evaporative Casting Process Parameters on the Surface Roughness of Al-7% Si Alloy Castings, J. Mater. Process. Technol, 2007, **182**, 615–623.

[7] G. Mahendran, V. Balasubramanian, T. Senthilvelan. Developing Diffusion Bonding Windows for Joining AZ31B Magnesium–AA2024 Aluminium Alloys, J. Mater Des, 2009, **30**(4), 1240–1244.

[8] G. Mahendran, V. Balasubramanian, T. Senthilvelan, Developing Diffusion Bonding Windows for Joining AZ31B Magnesium–Copper Dissimilar Joints, Int. J. Adv. Manuf. Technol., 2009, **42**(7–8), 689– 695.

[9] D.C. Montgomery, Design and Analysis of Experiments, 3rd ed.,Wiley,New York, 2001.

[10] T. Hou, C. Su, W. Liu. Parameters Optimization of a Nano-Particle Wet Milling Process Using the Taguchi Method Response Surface Method and Genetic Algorithm, Powder. Technol, 2007, **173**, 153–162.

[11] J. Pilling, N. Rediely. Solid State Bonding of Superplastic AA7475, Mater. Sci. Technol., 1987, **3**, 353–359.

[12] S. Kundu, M. Ghosh, A. Laik, K. Bhanumurthy, G.B. Kale, and S. Chatterjee, Diffusion Bonding of Commercially Pure Titanium to 304 SS Using Copper Interlayer, Mater. Sci. Eng. A, 2005, **407**, 154–160.

[13] Y. Huang, N. Ridley, F. Humphreys, J. Cui. Diffusion Bonding of Superplastic 7075 Aluminium Alloy, Mater. Sci. Eng. A, 1999, **266**, 295–302.

[14] P. He, J. Feng, B. Zhang, Y. Qian. Micro Structure and Strength of Diffusion-Bonded Joints of Ti-Al Base Alloy to Steel, Mater. Charact. 2002, **48**, 401–406.

[15] N. Orhan, T. Khan, M. Eroglu. Diffusion Bonding of a Micro Duplex Stainless Steel to Ti–6Al–4V, Scr. Mater, 2001, **45**, 441–446.

[16] M. Muratoglu, O. Yilmaz, M. Aksoy. Investigation on Diffusion Bonding Characteristics of Aluminum Metal Matrix Composites (Al/SiCp) with Pure Aluminum for Different Heat Treatments, J. Mater. Process. Technol., 2006, **178**(1–3), 211–217.

Chapter 5 Discussion on bonding mechanism and simulation of bonding process

5.1 Introduction

Microstructure properties of transition zone of dissimilar metals on bonding interface mainly depend on the elemental diffusion. In the diffused process, under the roles of the heating temperature, holding time and cooling time, the alloy elements nearby the interface conducted different degree of diffusion; when reached to a certain concentration, the diffused reaction produced [1]. The recrystallization, the formation of intermetallic compound and transition zone played an important role for interface, so that affected the mechanical properties of diffused welding joint.

Elemental diffused power of Mg/Al dissimilar metals depended on the concentration gradient, diffused coefficient and interface conditions from elemental Mg and Al (including that crystal structure, contact condition and crystal defects of the material welded). The elemental coefficient depended on heating temperature and activation energy [2]. But between different reacted layers of Mg/Al dissimilar metals diffused welding interface, the different microstructure layers formed because the differences from elemental concentration [3]. Therefore, the elemental diffused coefficient was not a fixed value on diffused interface in formed process, but it was constantly changing constant with diffused process [4]. The determination for the diffused coefficient was a key to research diffused distribution, the formation and growth of reacted layers and the width changed transition zone.

This paper for the element nearby Mg/Al diffused interface conducted value analysis through establish the related equation of the diffused coefficient (D) and the concentration (C) in each phase layer of interface transition; the

diffused coefficient and activation of each phase layer of Mg/Al diffused interface was calculated and forming mechanism of phase microstructure in interface transition zone was stated further, so that established the constitutive relation between Mg/Al welding joint. The simulation for stress field on bonding interface under different process parameters laid the theoretical foundation for the formation mechanism Mg/Al dissimilar metals diffused welding and the atomic dynamic on interface in metal diffused process.

5.2 Mg/Al interface elements analysis of the theory of diffusion

Diffusion is the material that touches each other through thermal motion to produce mutual penetration; the direction is to the position of decreased material concentration and makes the atom in the occupied space distribute uniform, in which it may be itself atom diffusion or heterogeneity from external substances [5]. The mainly parameters in diffusion were diffused coefficient D and diffused activation energy Q. diffused coefficient D is average particle number across a certain plane in per unit time [6]. Diffused activation energy Q is minimum energy from a position jump to another position in order to overcome force of around atoms. Diffused coefficient, diffused activation energy and the temperature meet Arrhenius index relation as shown in follows:

$$D = D_0 \exp(-Q/RT) \tag{5-1}$$

D_0: Diffusion factors / $m^2.s^{-1}$; Q: Activity energy/$J.mol^{-1}$; R: $8.314 J.mol^{-1}.K^{-1}$; T: K;

Table 5.1 Diffusion factors (D_0) and activity energy (Q) of Mg and Al.

Element	Diffusion factors (D_0)/ $m^2.s^{-1}$	Activity energy (Q)/$J.mol^{-1}$
Al	1.7×10^{-4}	1.42×10^5
Mg	1.5×10^{-4}	1.36×10^5
Mg in Al	6.3×10^{-6}	1.13×10^5
Al in Mg	1.2×10^{-3}	1.44×10^5

According to Arrhenius equation, the diffused coefficient of element Mg and Al under different temperature was calculated. As shown in Fig. 5.1, self-diffusion coefficient of element Mg and Al was change with the temperature. As shown in Fig. 5.2, the diffused coefficient of Mg in Al substance and Al in Mg substance was change with temperature.

D is diffused coefficient; Q is diffused activation energy; D_0 is Boltzmann constant and T is heating temperature. According to formula (5-1) Arrhenius, the diffused coefficient of Mg and Al under different temperature was calculated. As shown in Table 5.2, the self-diffusion of element Mg and Al and diffused coefficient calculated value in mutual diffusion [7]. It is known that self-diffusion coefficient of element Mg and Al gradually became larger with heating temperature was increasing. So the heating temperature was higher, it is in favors of conducing elemental diffusion.

Under same temperature conditions, self-diffusion of element Mg was greater than that of element Al, that is to say the diffused rate of Mg atoms was greater than that of Al atoms [8]. With heating temperature, the diffused coefficients of Al in Mg basal body and Mg in Al basal body were also gradually increase. But the diffused coefficient of Al in Mg basal body was greater than that of Mg in Al basal body [9]. It is shown that the effect of heating temperature on the diffusion of Al in Mg basal body was more obvious. In the diffused process between Mg and Al dissimilar metals, the diffusion of element Al nearby the interface was faster and sufficient.

Table 5.2 Calculation of diffused coefficient under different temperature.

	20℃	120℃	220℃	320℃	420℃
Al（D/ mm^2.s^{-1}）	0.671×10^{-9}	2.292×10^{-9}	1.465×10^{-9}	5.071×10^{-9}	3.364×10^{-9}
	430℃	440℃	450℃	520℃	580℃
	4.778×10^{-9}	6.713×10^{-9}	9.356×10^{-9}	7.364×10^{-9}	7.452×10^{-9}
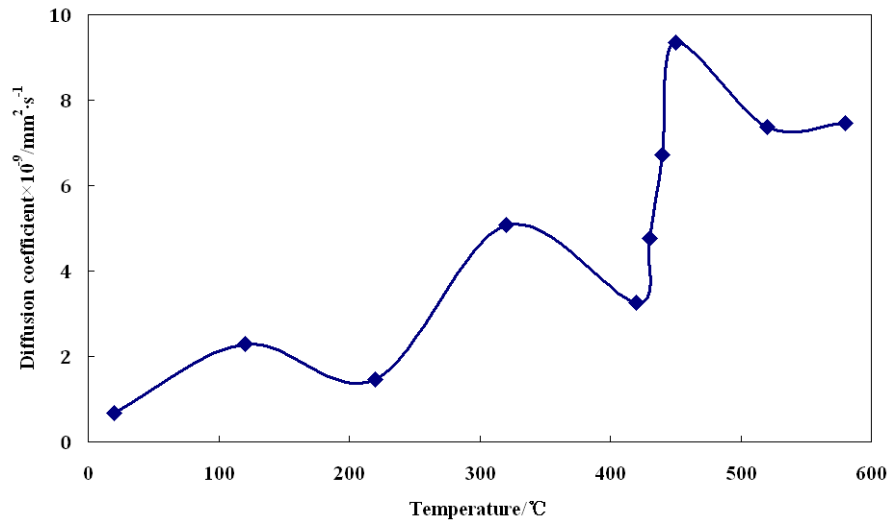
Fig. 5.1 Relation between self-diffusion coefficient D and temperature T of Al.

	20℃	120℃	220℃	320℃	420℃
	1.235×10^{-9}	4.621×10^{-9}	3.521×10^{-9}	10.15×10^{-9}	8.412×10^{-9}
Mg（D/ mm^2.s^{-1}）	430℃	440℃	450℃	520℃	580℃
	11.76×10^{-9}	16.31×10^{-9}	22.40×10^{-9}	14.58×10^{-9}	14.26×10^{-9}
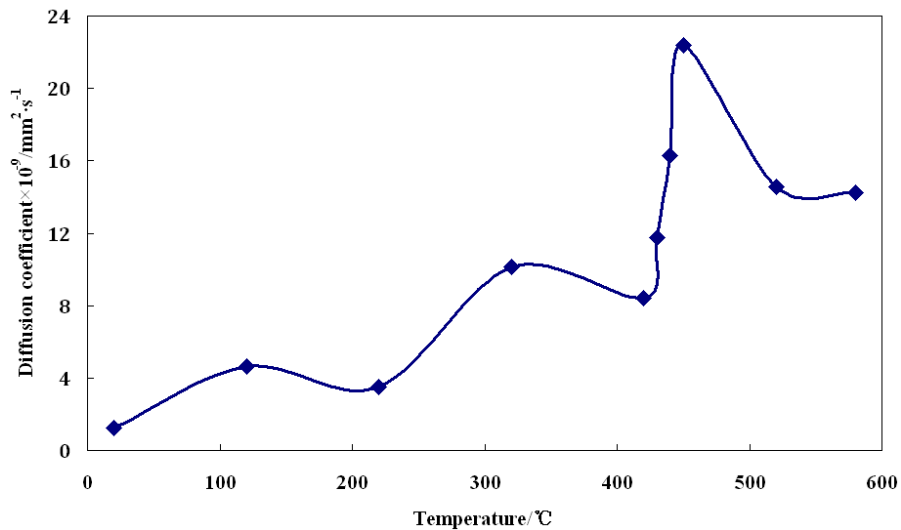
Fig.5.2 Relation between self-diffusion coefficient D and temperature T of Mg.

	20℃	120℃	220℃	320℃	420℃
Al in Mg（D/ mm^2.s^{-1}）	0.255×10^{-8}	0.915×10^{-8}	1.035×10^{-8}	1.358×10^{-8}	1.912×10^{-8}
	430℃	440℃	450℃	520℃	580℃
	2.502×10^{-8}	3.383×10^{-8}	4.734×10^{-8}	5.194×10^{-8}	5.103×10^{-8}
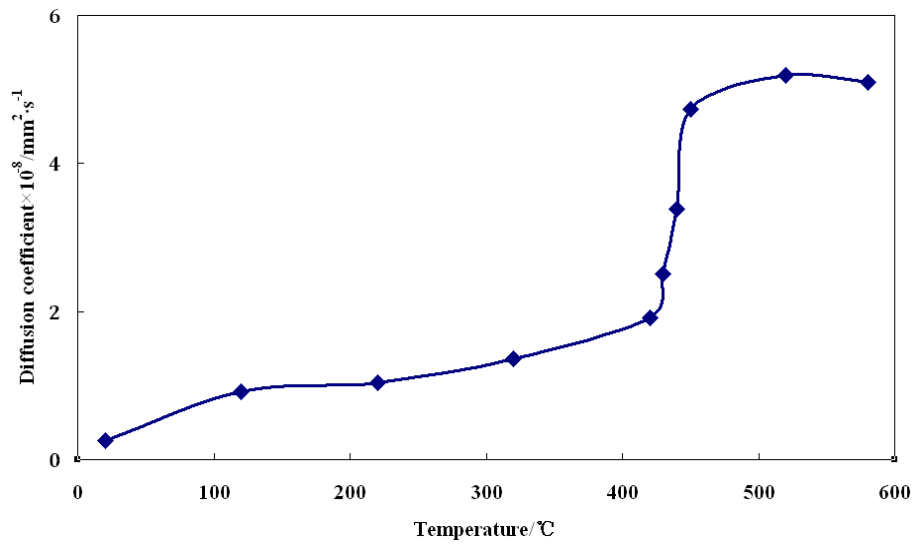
Fig.5.3 Relation between self-diffusion coefficient D and temperature T of Al in Mg substrate.

	20℃	120℃	220℃	320℃	420℃
Mg in Al $(D/ mm^2.s^{-1})$	0.185×10^{-8}	0.815×10^{-8}	0.956×10^{-8}	1.258×10^{-8}	1.678×10^{-8}
	430℃	440℃	450℃	520℃	580℃
	2.394×10^{-8}	3.118×10^{-8}	4.316×10^{-8}	4.942×10^{-8}	4.830×10^{-8}
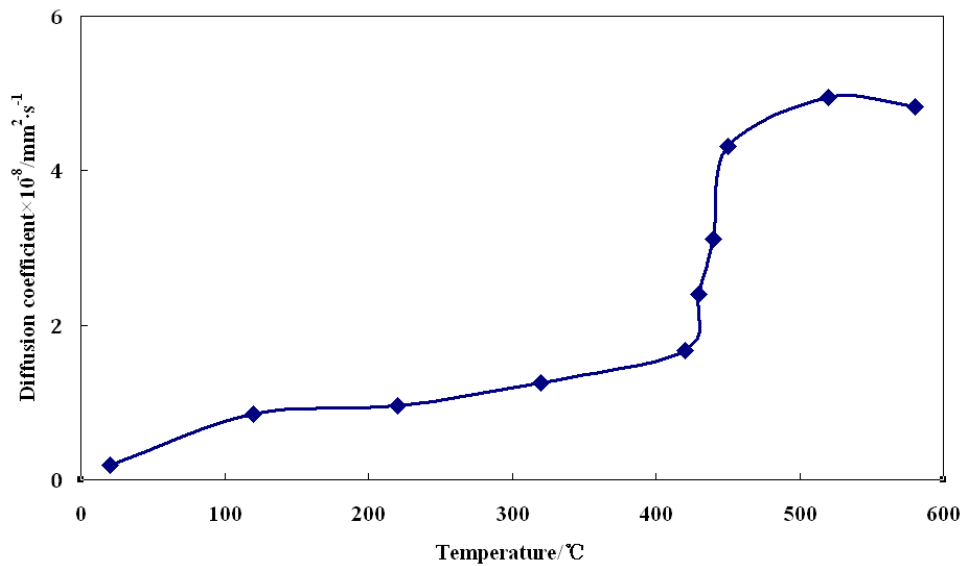
Fig.5.4 Relation between self-diffusion coefficient D and temperature T of Mg in Al substrate.

In Mg/Al diffused welding process, the role of atom diffused nearby interface made elemental concentration gradient changed with distance and time. Base- material Mg/Al thickness was 3mm. The sufficient diffused atoms

were provided relative to the atomic diffusion in diffused welding process [10]. Therefore, Mg and Al metal was regarded as infinite substance. In addition, there is great concentration between Mg and Al sides; the atom could diffuse from one side to another side and conformed one-dimensional diffusion regularity [11]. Therefore, Mg and Al atom diffusion could adopt unsteady diffused equation in one-dimensional infinite medium conducted solve.

$$C(x,t) = C_0(x > 0), 0(x < 0) \tag{5-2}$$

$$C(x,t) = \frac{C_0}{2\sqrt{\pi Dt}} \int_{x_1}^{x_2} e^{\frac{(\xi - x)^2}{4Dt}} d\xi \tag{5-3}$$

If $\eta = \dfrac{x - \xi}{\sqrt{4Dt}}$, then $C(x,t) = -\dfrac{C_0}{\sqrt{\pi}} \int_{\frac{x - x_1}{\sqrt{4Dt}}}^{\frac{x_1 - x_2}{\sqrt{4Dt}}} \exp(-\eta^2) d\eta$ \hfill (5-4)

$$erf(Z) = -\frac{2}{\sqrt{\pi}} \int_0^Z \exp(-\eta^2) d\eta,$$

$$C(x,t) = -\frac{C_0}{2} \left[\frac{2}{\sqrt{\pi}} \int_0^{\frac{x - x_2}{\sqrt{4Dt}}} \exp(-\eta^2) d\eta - \frac{2}{\sqrt{\pi}} \int_0^{\frac{x - x_2}{\sqrt{4Dt}}} \exp(-\eta^2) d\eta \right] \tag{5-5}$$

If x1=0, x2→∞, then

$$C(x,t) = -\frac{C_0}{2} \left[1 + erf\left(\frac{x}{\sqrt{4Dt}} \right) \right] \tag{5-6}$$

$$C(x,t) = C_0 = C_2(x > 0), 0(x < 0) \tag{5-7}$$

$$C(x,t) = \frac{C_0}{2} \left[1 + erf\left(\frac{x}{\sqrt{4Dt}} \right) \right] \tag{5-8}$$

$$C(x,t) = 0(x > 0), C_0 = C_1(x < 0) \tag{5-9}$$

$$C(x,t) = \frac{C_0}{2}\left[1 - erf\left(\frac{x}{\sqrt{4Dt}}\right)\right]$$ (5-10)

In value analysis of elemental concentration distribution nearby Mg/Al diffused welding interface, the parametric of directly reaction elemental concentration distribution were mainly diffused coefficient D, diffused behavior of diffused distance x and holding time t, element Mg and Al was calculated by theory value [12]. The effect of diffused welding heating temperature and holding time on elemental distribution and diffused distance was discussed. The heating temperature and holding time on diffusion of element Mg and Al meet the relation of concentration and distance. When heating temperature became constant, concentration distribution of element Mg and Al was more trended to moderate with the increasing of holding time. Therefore, to increase holding time more conducive to sufficient diffusion between element Mg and Al and made elemental concentration nearby interface became more uniform. Under different heating temperature, the elemental diffused distance nearby interface was affected obviously. With heating temperature and holding temperature to increase, the diffused distance of element Mg and Al also gradually increased.

5.3 Reaction kinetics of Mg/Al diffusion welding interface

The mutual diffusion of Mg and Al atoms was the main reason to form joint nearby Mg/Al diffused zone. The diffusion directly caused the formation of Mg-Al intermetallic compound that affected the properties of the joint [13]. The structure diagram of formed phase on diffused welding interface as shown in Fig. 5.5.
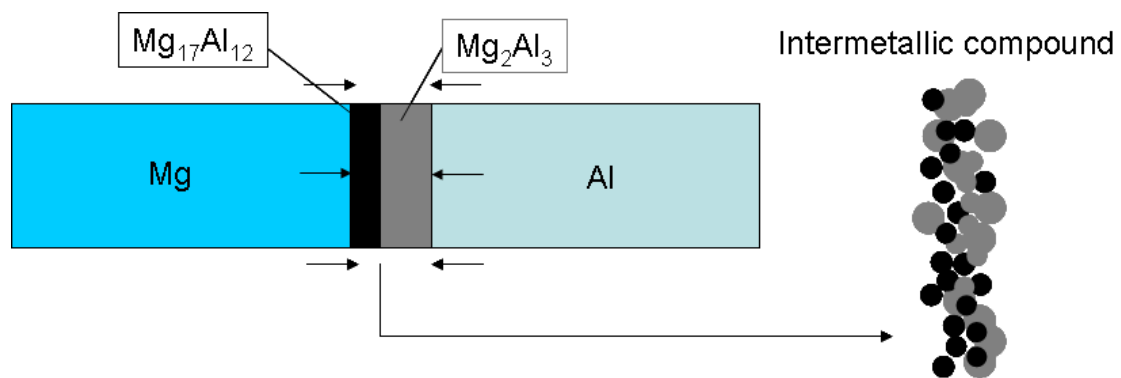
Fig.5.5 Bonding mechanism image of bonding process

In Mg/Al vacuum diffused welding process, no pressure bonding was adopted to descript the growth process of intermetallic compound between binary pure metal that can be described by parabolic diffused rate constant. On the other hand, bonding diffused coefficient D_{int} could be introduced when a narrow homogeneous phase zone was formed in solid state reaction, so that the diffused redistribution of element in reaction zone was described [14]. The diffused coefficient of the material D in a certain phase through bonding homogeneous phase was limited between N' and N'' (mole fraction of component i). D_{int} as shown in equation (5-11, 5-12):

$$D_{\text{int}} = \int_{N''}^{N'} D\, dN \tag{5-11}$$

$$D_{\text{int}} = N_A \cdot N_B \cdot N_P, \quad K_P = \frac{(\Delta x)^2}{2t} \tag{5-12}$$

Mg$_2$Al$_3$、Mg$_{17}$Al$_{12}$ alloy phases formed in Mg/Al diffused interface, to Mg$_2$Al$_3$ as an example, bonding diffused coefficient D_{int} in the growth process had relation with parabolic rate constant.

$$D_{int}\left(Mg_2Al_3\right)= N_{Al} \cdot N_{Mg} \cdot K_P = \frac{6}{25} K_p \qquad (5\text{-}13)$$

The formed rate of the generation in diffused interface for the formation of transition zone was very important. It made element calculate the reaction rate of binary metallic phase in diffused interface by the effect in multiphase reaction zone. For binary diffusion of metal A/B, the calculated equation of the reaction rate of intermetallic compound in interface as shown in equation (5-14).

$$v = \frac{V_B\left(\dfrac{D_A}{D_B}\right)-1}{V_M\left[\dfrac{V_B}{V_A}\dfrac{D_A}{D_B}\right]N_B + N_A}\left(\frac{D_{int}}{\Delta x}\right) \qquad (5\text{-}14)$$

Δx -Each phase layer of interface transition zone width; N-Reaction component mole fraction of the I; V_A, V_B, V_M-Reaction of partial molar volume of the component; D_A, D_B-Diffusion coefficient

In order to facilitate calculation, it assumes that there is no other elemental affect and partial molar volume of composition was equal. The growth equation of reaction rate could be simplified to equation (5-15).

$$v_{MgAl} = \frac{\dfrac{D_{Al}}{D_{Mg}}-1}{\dfrac{D_{Al}}{D_{Mg}}N_{Mg} + N_{Al}}\left(\frac{D_{int}}{\Delta x}\right) \qquad (5\text{-}15)$$

It is shown that sequence from the growth rate of each phase layer and the formation of generated phase was consistent when the heating temperatures

were 430°C and 440°C. With increasing heating temperature, the growth rate of Mg_2Al_3 and $Mg_{17}Al_{12}$ phases also gradually increased. When the heating temperature was 450°C, effect of the heating temperature on Mg/Al diffused interface became obviously. With increasing heating temperature, the elemental diffusion nearby transition layer closed the both sides of base-materials was improved obviously, so that the growth rate of the generated phases in the both side transition zone gradually increased.

5.4 Thermomechanical behavior of Mg-AZ31/Al-6061 diffused process

Mg-Al bonding material has a certain strength and abundant ductility. Therefore, not only high bonding strength can be get application, but also it can be applied in complex machining. At the same time, the brittle destruction was caused [15]. It is also a reason of Mg-Al bonding material has been widely applied. For bonding material, base metal was affected by rolling, forging cutting lead to produce the plastically deformation of the metal, so that the strength and ductility of products will change with plastically deformation to cause the reducing of used life. It is an important for the deformed principle of bonding material and some drawbacks in using can be avoided.

5.4.1 Elastoplastic constitutive equation

In this paper, elastic deformation and plastic deformation of bonding material will be discussed at first. The actual experiment was conducted from the stress and strain. According to the plastic deformation of the material and stress distribution, the study analyzed mechanical properties and mechanical strength. Through stated to displace deformation theory, the strength of the material and deformation process was discussed in detail while crystal grain strengthening, dispersion strengthening, solid solution and precipitation

strengthening of various means of various   strengthening means and principles equation were optimized by strengthening for displacement.

For the general space problems of elastic-plastic mechanics, stress state of a point could be represented by nine stress components, such as the stress and strain from a point in Cartesian coordinate system could be represented was shown in below:
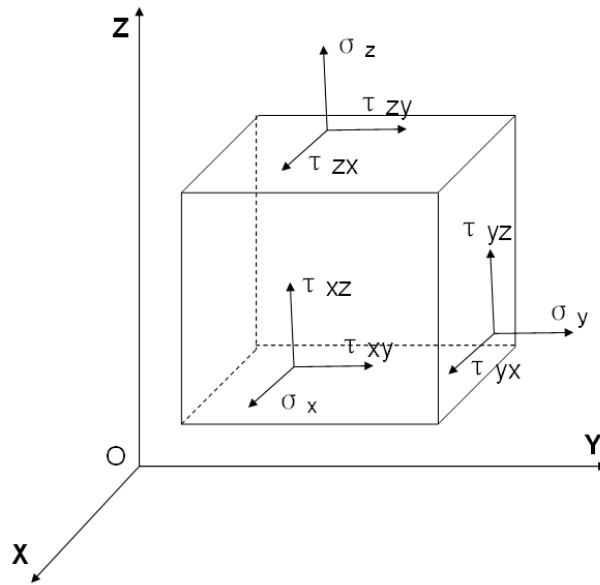
Fig. 5.6 Schematic of tiny part in internal of the material

Relationships of stress and strain in occurrence elastic deformation process as shown in bellow. According to linear elastic theory (Hooke's law)

$$\sigma_{ij} = C_{ijkl}\varepsilon_{kl} \tag{5-16}$$

$$
\begin{Bmatrix}
\sigma_{xx} \\
\sigma_{yy} \\
\sigma_{zz} \\
\tau_{xy} \\
\tau_{yx} \\
\tau_{yz} \\
\tau_{zy} \\
\tau_{zx} \\
\tau_{xz}
\end{Bmatrix}
=
\begin{bmatrix}
C_{xxxx} & C_{xxyy} & C_{xxzz} & C_{xxxy} & C_{xxyx} & \cdots & C_{xxzx} & C_{xxxz} \\
C_{yyxx} & C_{yyyy} & C_{yyzz} & C_{yyxy} & C_{yyyx} & \cdots & C_{yyzx} & C_{yyxz} \\
\cdots & \cdots & \cdots & \cdots & & & & \\
C_{xyxx} & C_{xyyy} & C_{xyzz} & C_{xyxy} & C_{xyyx} & \cdots & C_{xyzx} & C_{xyxz} \\
& & & & & & & \\
& & & & & & & \\
& & \cdots & \cdots & \cdots & \cdots & & \\
& & & & & & & \\
C_{xzxx} & C_{xzyy} & C_{xzzz} & C_{xzxy} & C_{xzyx} & \cdots & C_{xzzx} & C_{xzxz}
\end{bmatrix}
\begin{Bmatrix}
\varepsilon_{xx} \\
\varepsilon_{yy} \\
\varepsilon_{zz} \\
\gamma_{xy} \\
\gamma_{yx} \\
\gamma_{yz} \\
\gamma_{zy} \\
\gamma_{zx} \\
\gamma_{xz}
\end{Bmatrix}
\tag{5-17}
$$
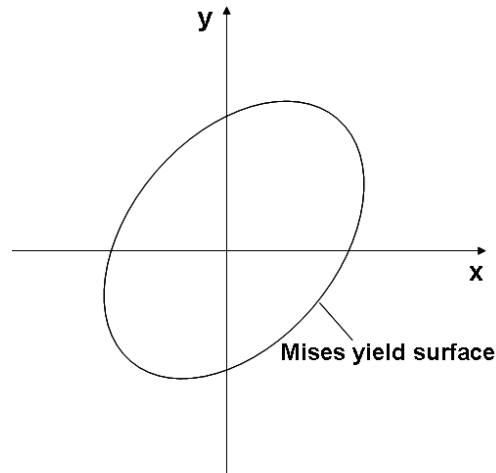
Fig.5.7 Schematic of Mises yield surface

In plastic deferment, plastic strain increments $d\varepsilon_{ij}$ can be divided into two parts after the material produce plastic deformation.

$$d\varepsilon_{ij} = d\varepsilon_{ij}^e + d\varepsilon_{ij}^p \qquad (5\text{-}18)$$

$$d\varepsilon_{ij}^e = \frac{d\sigma_{ij}}{2G} - \frac{3\upsilon}{E}d\sigma\delta_{ij} \quad \text{Or} \quad d\varepsilon_{ij}^e = \frac{1}{2G}ds_{ij} \qquad (5\text{-}19)$$

Plastic strain increments $d\varepsilon_{ij}$ satisfies the following equation:

$$d\varepsilon_{ij}^p = dm\frac{\partial f}{\partial \sigma_{ij}} \qquad (5\text{-}20)$$

For an ideal plastic material $\varphi = f$, f is the yield function, m is proportionality coefficient. We can create incremental relationship between stress and strain and establish related rule with Mises yield condition because the law is different when loading and unloading.

According to Mises yield condition,

$$f = J_2' - \tau_s^2 = 0, \text{ then } d\varepsilon_{ij}^p = dm\frac{\partial f}{\partial \sigma_{ij}} = dm\frac{\partial J_2'}{\partial \sigma_{ij}} = dms_{ij}$$

$$de_{ij} = \frac{1}{2G} ds_{ij} + dms_{ij} \left.\right\} \quad d\varepsilon_{kk} = \frac{1-2\upsilon}{E} d\sigma_{kk}$$ (5-21)

It is considered that plastic strain did not produced under elasticity and unloading states, dλ=0.

$$d\varepsilon_{ij} = dms_{ij}$$ (5-22)

For reinforced materials, when the smooth loading surface $\varphi = 0$, there is relationship between the plastic strain increment.

$$d\varepsilon_{ij}^{p} = dm \frac{\partial \varphi}{\partial \sigma_{ij}}$$ (5-23)

The loading was conducted under $d\varphi = \frac{\partial \varphi}{\partial \sigma_{ij}} d\sigma_{ij} > 0$ and $d\lambda > 0$ while Neutral variable load（$d\varphi = 0$）and uninstall（$d\varphi < 0$）, $d\lambda = 0$ was obtained. Therefore, the equation was set as $d\lambda = hd\varphi$. In which h is strengthening modulus.

$$d\varepsilon_{ij}^{p} = hd\varphi \frac{\partial \varphi}{\partial \sigma_{ij}}$$ (5-24)

In Mises and so on strengthening modulus, the equation become as following according to make $h = 1/\varphi'$

$$d\varepsilon_{ij}^{p} = \frac{3}{2\varphi'} \frac{d\overline{\sigma}}{\overline{\sigma}} s_{ij}$$ (5-25)

φ' can be confirmed by the stretching curve. $\varphi' = \frac{d\sigma}{d\varepsilon^{p}}$ is slope from $\sigma = \sigma(\varepsilon^{p})$. When linear strengthen was conducted, φ' is constant.

5.4.2 Thermal mechanical stresses analysis

In the bonding process, the thermal stress and elastic modulus *E,* thermal expansion coefficient α and temperature change ΔT are proportional. In the initial situation, *E* and α can be ignored with the change of the temperature; the thermal stress of the structure increased with the change of the temperature. During the analysis, three aspects of physics, geometry and balance were included. It is the condition need to meet that thermo elasticity problem was analyzed. In which physical relationship not only included linear elastic Hooke's law, but also included the deformation was caused by the change of the temperature. The temperature and the time under two-dimensional non-steady state meet the following functional.

$$T = T(x, y, t) \tag{5-26}$$

The general conduct heat differential equations

$$\frac{\partial T}{\partial t} - \frac{\lambda}{C_P \rho} \left(\frac{\partial^2 T}{\partial x^2} + \frac{\partial^2 T}{\partial y^2} + \frac{\partial^2 T}{\partial z^2} \right) = \frac{Q}{C_P \rho} \tag{5-27}$$

Two-dimensional non-steady conduct heat equation as shown in following:

$$\frac{\partial T}{\partial t} = \frac{k}{C_p \rho} \left(\frac{\partial^2 T}{\partial x^2} + \frac{\partial^2 T}{\partial y^2} \right) \tag{5-28}$$

Variable temperature of each point is T in elastic body, each point tiny length of elastic body produced strain αT, αis linear thermal expansion, deformation component of each point in elastic body as bellows:

$$u_{xx} = v_{yy} = w_{zz} = \alpha T, \quad \gamma_{yz} = \gamma_{zx} = \gamma_{xy} = 0 \tag{5-29}$$

Under the role of temperature field, deformation component of each point in elastic body as shown in bellow equation:

$$\dot{\varepsilon}_{ij}^{T} = \alpha \Delta T \delta_{ij} \qquad (5\text{-}30)$$

The total strain rate $\dot{\varepsilon}_{ij}$ can be decomposed as:

$$\dot{\varepsilon}_{ij}^{T} = \dot{\varepsilon}_{ij}^{Te} + \dot{\varepsilon}_{ij}^{Tp} \qquad (5\text{-}31)$$

Where $\dot{\varepsilon}_{ij}^{Te}$, $\dot{\varepsilon}_{ij}^{Tp}$ are elastic, viscoplastic and thermal strain rate respectively. The elastic strain rate could be induced from the Hook's law with Young's modulus and Poisson's ratio,

$$\dot{\varepsilon}_{ij}^{e} = \frac{1+v}{E}\dot{\sigma}_{ij} + \frac{\partial}{\partial T}\left(\frac{1+v}{E}\right)\dot{T}\sigma_{ij} - \frac{v}{E}\dot{\sigma}_{kk}\delta_{ij} - \frac{\partial}{\partial \theta}\left(\frac{v}{E}\right)\dot{T}\sigma_{kk}\delta_{ij} \qquad (5\text{-}32)$$

According to the constitutive law, the stress is related to strains by:

$$\dot{\sigma}_{ij} = E(T)\dot{\varepsilon}_{ij}^{Te} \qquad (5\text{-}33)$$

Where $E(T)$ is the temperature dependent Young's modulus of elasticity. According to the definition of the elastic modulus, the equation can be calculated out:

$$E = \frac{A}{r^{N}} \qquad (5\text{-}34)$$

Where A, N are constants, elastic modulus with atomic spacing change, because the atomic spacing generally increases with increasing temperature, so the E decreases with increasing temperature. The above equation is arranged by differentiator.

$$\frac{1}{E}\frac{dE}{dT}+\left(\frac{1}{r}\frac{dr}{dT}\right)N=0 \qquad (5\text{-}35)$$

$\eta=\dfrac{1}{E}\dfrac{dE}{dT}$, $\alpha=\dfrac{1}{r}\dfrac{dr}{dT}$ according to above equation $\dfrac{\alpha}{\eta}=-\dfrac{1}{N}=const$, in which

the ratio of $\dfrac{\alpha}{\eta}$ is 4×10^{-2}, $\eta=-25\alpha$, $\eta=\dfrac{1}{E}\dfrac{dE}{dT}$ was deformed by integration.

$$\int_{T_0}^{T}-25\alpha dT=\int_{T_0}^{T}\frac{dE}{E} \qquad (5\text{-}36)$$

α at higher temperatures approximate to a constant, and the magnitude is small. For above integration, $e^{x}\approx1+x$ was used to obtain:

$$E=E_0\left(1-25\alpha T\right) \qquad (5\text{-}37)$$

E_0- elasticitity modulus under room temperature. α- temperature coefficient of elasticity modulus.

Viscoplastic is given by Anand constitutive model and Perzyna's model. The specific functional form for the flow equation of Anand model was selected as Eq. (5-37)

$$\dot{\varepsilon}_{ij}^{Tp}=A\exp\left(-\frac{Q}{RT}\right)\left[\sinh\left(\xi\frac{\sigma_{ij}^{T}}{s}\right)\right]^{1/m} \qquad (5\text{-}38)$$

The four material parameters in this constitutive function are A, Q, m and ξ. In the temperature and strain rate range of interest here, all these material parameters were taken to be temperature independent. However, for a large temperature range this assumption is not suitable and some of the parameters will be temperature dependent. This will be discussed later. The parameter A is called the preexponeetial factor, Q is called the activation energy, m is called

the strain rate sensitivity, ξ is a dimensionless multiplier of stress. R is the gas constant.

The form of evolution equation for the internal variable s was adopted to represent the hardening behavior of a material is:

$$\dot{s}_{ij} = \left\{ h_0 \left| \left(1 - \frac{s_{ij}}{s^*} \right) \right|^a sign \left(1 - \frac{s_{ij}}{s^*} \right) \right\} \dot{\varepsilon}_{ij}^{Tp}; \quad a > 1 \tag{5-39}$$

With

$$s^* = \tilde{s} \left[\frac{\dot{\varepsilon}_{ij}^{Tp}}{A} \exp \left(\frac{Q}{RT} \right) \right]^n \tag{5-40}$$

The material parameters in this constitutive function are h_0, a, $\tilde{s}$, and n, h_0 represents a constant rate of a thermal hardening, a is strain rate sensitivity of hardening or softening, $\tilde{s}$ is dimensionless coefficient for deformation resistance saturation value, a represents strain rate sensitivity of saturation (deformation resistance) value, s^* represent a saturation value of s associated with a given temperature/strain rate pair. The nine parameters of Anand constitutive model A, $A, T, \xi, m, h_0, \tilde{s}, n, a$ and S_0 can be obtained from compression tests.

Table5.5 Anand model parameters of Mg-AZ31

Parameter	S_0	Q	R	A	ξ	m	h_0	$\tilde{s}$	n	a
Units	MPa	J/mole	J/(mole.K)	1/s	-	-	MPa	MPa	-	-
Value	35	161000	8.31	1.5E9	6.1	0.35	4038	110	0.032	1.07

The Perzyna's model assumes that the inelastic strain is produced as

$$\dot{\varepsilon}_{ij}^{T'p} = \Lambda < \psi(F) > \frac{\partial F}{\partial \sigma_{ij}} \tag{5-41}$$

Λ denoted a viscosity constant of the material, and $\psi(F)$ is a function of the static yield function in stress space.

$$\dot{\varepsilon}_{ij}^{T'p} = \frac{1}{2\mu} <1 - \frac{\sigma_y}{(3J_2)^{1/2}}> S_{ij} \qquad (5\text{-}42)$$

$$\dot{\varepsilon}_{ij}^{T'p} = \frac{1}{3\mu} (|\sigma| - \sigma_s) \frac{\sigma}{|\sigma|} \qquad (5\text{-}43)$$

$$\mu = a \cdot e^{-b\dot{\varepsilon}} \qquad (5\text{-}44)$$

Where Mises yield condition: $J_2 = \left\{ \frac{3}{2} \sigma_{ij}' \sigma_{ij}' \right\}^{1/2}$, a, b are undetermined coefficient. From the experimental casting tests, the temperature gradient and strain rate could be induced. Based on the method proposed above, the parameter a, b for representing the viscosity coefficient could be obtained. By assuming the viscosity coefficient is linear related to temperature, the viscosity coefficient surface with temperature and strain rate could be identified as given in follow section.

Table5.6 Perzyna's model parameters of Al-6061

Parameter	Viscosity coefficient for inelastic model	Expansion coefficient	Potion ratio	Young's Modulus	Yield strength
Units	MPa.s	K^{-1}	-	GPa	MPa
Value	$a = 0.006T^2 - 2.7514T + 2022.4$ $b = -0.0005T^2 - 0.4705T + 40.752$	25.6 $\times 10^{-6}$	0.3	73.9	75.459

5.4.3 Finite element model of thermal elastic-plastic analysis

For welding materials, Von Mises is more conform with the actual situation, so Von Mises can be used to determine the criteria in the elastic-plastic analysis of welding materials.

Effect force expression of Von Mises as shown in:

$$\bar{\sigma} = \frac{1}{\sqrt{2}}\left[\left(\sigma_x - \sigma_y\right)^2 + \left(\sigma_y - \sigma_z\right)^2 + \left(\sigma_z - \sigma_x\right)^2 + 6\left(\tau_{xy}^2 + \tau_{yz}^2 + \tau_{zx}^2\right)\right]^{\frac{1}{2}} \qquad （5-45）$$

When the equivalent stress exceeds the yield stress of the material, plastic deformation will be occurred.

For complex loading conditions, flow rule of incremental form which the increment ε_{ij} of the total strain equal to the incremental sum of elastic strain ε_{ij}^E and plastic strain ε_{ij}^P.

$$d\varepsilon_{ij} = d\varepsilon_{ij}^E + d\varepsilon_{ij}^P \qquad （5-46）$$

$$d\varepsilon_{ij} = d\varepsilon_{ij}^E + d\varepsilon_{ij}^T + d\varepsilon_{ij}^P \qquad （5-47）$$

When considering the relationship of the mechanical properties and the stress-strain related with temperature, full strain increment in the elastic region can be expressed as:

$$\{d\varepsilon\} = \{d\varepsilon\}_e + \{d\varepsilon\}_T \qquad （5-48）$$

$\{d\varepsilon\}_e$ Satisfies the compatibility conditions to generate elastic strain increment. When reach stress state $\{\sigma\}$, because the elastic matrix $[D]_e$ change with the temperature, the equation could be obtained:

$$\{d\varepsilon\}_e = d\left[[D]_e^{-1}\{\sigma\}\right] = [D]_e^{-1}\{d\sigma\} + \frac{\partial [D]_e^{-1}}{\partial T}\{\sigma\}dT \qquad (5-49)$$

Thermal strain increment $\{d\varepsilon\}_T$ is Incremental differential $\{\alpha_0 T\}$, so:

$$\{d\varepsilon\}_T = \left\{\alpha_0 + \frac{\partial \alpha_0}{\partial T}T\right\}dT = \{\alpha\}dT \qquad (5-50)$$

$\{\alpha\}$ is a Valid value of thermal expansion coefficient.

$$\{d\sigma\} = [D]_e\{d\varepsilon\} - \{C\}_e \, dT \tag{5-51}$$

$$\{C\}_e = [D]_e\left(\{\alpha\} + \frac{\partial[D]_e^{-1}}{\partial T}\{\sigma\}\right) \tag{5-52}$$

In the plastic zone, the material yield function is set as $f(\sigma_x, \sigma_y, \cdots)$, the value reach $f_0(\sigma_s, T, K)$ under the temperature and the strain hardening index, the material starts to yield.

$$f = f_0\left[\sigma_s(T), K(\varepsilon_p), \cdots\right] \tag{5-53}$$

Differential form as shown in below

$$\left\{\frac{\partial f}{\partial \sigma}\right\}\{d\sigma\} = \left(\frac{\partial f_0}{\partial \varepsilon_p}\right)\left\{\frac{\partial K}{\partial \varepsilon_P}\right\}^T \{d\varepsilon_p\} + \frac{\partial f_0}{\partial T} \, dT \tag{5-54}$$

In the plastic region, the whole strain increment is decomposed into:

$$\{d\varepsilon\} = \{d\varepsilon\}_p + \{d\varepsilon\}_e + \{d\varepsilon\}_T \tag{5-55}$$

$\{d\varepsilon\}_p$ is plastic strain increment. According to flow rule, the follow equation is obtained:

$$\{d\varepsilon\}_p = \lambda\left\{\frac{\partial f}{\partial \sigma}\right\} \tag{5-56}$$

$$\lambda = \left[\left\{\frac{\partial f}{\partial \sigma}\right\}[D]_e\{d\varepsilon\} - \left\{\frac{\partial f}{\partial \sigma}\right\}[D]_e\left(\{\alpha\} + \frac{\partial[D]_e^{-1}}{\partial T}\{\sigma\}\right)dT - \frac{\partial f_0}{\partial T} \, dT\right] / S \tag{5-57}$$

Where,

$$S = \left\{\frac{\partial f}{\partial \sigma}\right\}[D]_e\left\{\frac{\partial f}{\partial \sigma}\right\} + \left(\frac{\partial f_0}{\partial K}\right)\left\{\frac{\partial K}{\partial \varepsilon_P}\right\}^T\left\{\frac{\partial f}{\partial \sigma}\right\} \tag{5-58}$$

Stress-strain relationship in the plastic zone can be expressed as following forms.

$$\{d\sigma\} = [D]_{ep}\{d\varepsilon\} - \{C\}_{ep}\,dT \tag{5-59}$$

Where,

$$\{C\}_{ep} = \left\{ [D]_{ep}\{\alpha\} + [D]_{ep}\frac{\partial [D]_e^{-1}}{\partial T}\{\sigma\} - [D]_e\left\{\frac{\partial f}{\partial \sigma}\right\}\left\{\frac{\partial f_0}{\partial T}\right\} / S \right\} \tag{5-60}$$

The loading and unloading in plastic zone was determined by λ in formula (5-49).

Uninstall is elastic behavior, the relation between the stress and the strain need to be transformed as formula (5-49).

Consider the material of plastic, the incremental form of the constitutive relation can be expressed as

$$d\sigma = (D - D_p)d\varepsilon \tag{5-61}$$

Where, D is elastic matrix, D_p is the plastic matrix.

$$\mathbf{D} = \begin{bmatrix} K+\dfrac{4}{3}G & K-\dfrac{2}{3}G & K-\dfrac{2}{3}G & 0 & 0 & 0 \\ K-\dfrac{2}{3}G & K+\dfrac{4}{3}G & K-\dfrac{2}{3}G & 0 & 0 & 0 \\ K-\dfrac{2}{3}G & K-\dfrac{2}{3}G & K+\dfrac{4}{3}G & 0 & 0 & 0 \\ 0 & 0 & 0 & G & 0 & 0 \\ 0 & 0 & 0 & 0 & G & 0 \\ 0 & 0 & 0 & 0 & 0 & G \end{bmatrix} \tag{5-62}$$

Where, The bulk modulus: $K = \dfrac{E}{3(1-2\mu)}$, Shear modulus: $G = \dfrac{E}{2(1+\mu)}$

In the strain space, plastic matrix can be expressed as

$$\mathbf{D_p} = \frac{1}{A}\mathbf{D}\frac{\partial f}{\partial \boldsymbol{\sigma}}(\mathbf{D}\frac{\partial f}{\partial \boldsymbol{\sigma}})^T \qquad (5\text{-}63)$$

Where, $A = (\frac{\partial f}{\partial \boldsymbol{\sigma}})^T\mathbf{D}\frac{\partial f}{\partial \boldsymbol{\sigma}} - (\frac{\partial f}{\partial \boldsymbol{\sigma}^p})^T\mathbf{D}\frac{\partial f}{\partial \boldsymbol{\sigma}} - B$, f is yield function, $\boldsymbol{\sigma}^p$ is the plastic

stress $\boldsymbol{\sigma}^p = \mathbf{D}\boldsymbol{\varepsilon}^p$.

Elastic-plastic matrix can be expressed as

$$\mathbf{D_{ep}} = \mathbf{D} - \mathbf{D_p} = \begin{bmatrix} p-m^2 & q-mn & q-ml & -\beta_1 S_{12}m & -\beta_1 S_{23}m & -\beta_1 S_{13}m \\ q-mn & p-n^2 & q-nl & -\beta_1 S_{12}n & -\beta_1 S_{23}n & -\beta_1 S_{13}n \\ q-ml & q-nl & p-l^2 & -\beta_1 S_{12}l & -\beta_1 S_{23}l & -\beta_1 S_{13}l \\ -\beta_1 S_{12}m & -\beta_1 S_{12}n & -\beta_1 S_{12}l & G-(\beta_1 S_{12})^2 & -\beta_1 S_{12}\cdot\beta_2 S_{23} & -\beta_1 S_{12}\cdot\beta_2 S_{13} \\ -\beta_1 S_{23}m & -\beta_1 S_{23}n & -\beta_1 S_{23}l & -\beta_1 S_{12}\cdot\beta_2 S_{23} & G-(\beta_1 S_{23})^2 & -\beta_1 S_{13}\cdot\beta_2 S_{23} \\ -\beta_1 S_{13}m & -\beta_1 S_{13}n & -\beta_1 S_{13}l & -\beta_1 S_{13}\cdot\beta_2 S_{12} & -\beta_1 S_{13}\cdot\beta_2 S_{23} & G-(\beta_1 S_{13})^2 \end{bmatrix}$$

Where, $p = K + \frac{4}{3}G$, $q = K - \frac{2}{3}G$, $\beta_1 = \dfrac{G}{\sqrt{(9K\alpha^2+G)J_2}}$, $\beta_2 = \dfrac{3Ka}{\sqrt{9K\alpha^2+G}}$,

$m = \beta_1 S_{11} + \beta_2$, $n = \beta_1 S_{22} + \beta_2$, $l = \beta_1 S_{33} + \beta_2$

Through the above analysis, stress-strain relationship of the incremental form relationship can be obtained as shown in following:

$$\{d\sigma\} = [D]\{d\varepsilon\} - \{C\}dT \qquad (5\text{-}64)$$

The elastic region: $[D] = [D]_e$ $\{C\} = \{C\}_e$

The plastic region: $[D] = [D]_{ep}$ $\{C\} = \{C\}_{ep}$

Where: $[D]_e$ is the elastic matrix. $\{C\}_e = [D]_e\left(\{a\} + \dfrac{\partial [D]_e^{-1}}{\partial T}\{\sigma\}\right)$

$$[D]_{ep} = [D]_e - [D]_e\left\{\frac{\partial f}{\partial \sigma}\right\}\left[\frac{\partial f}{\partial \sigma}\right]^T[D]_e / S \qquad (5\text{-}65)$$

$$\{C\}_{ep} = \left\{ [D]_{ep} \{\alpha\} + [D]_{ep} \frac{\partial[D]_e^{-1}}{\partial T} \{\sigma\} - [D]_e \left\{ \frac{\partial f}{\partial \sigma} \right\} \left\{ \frac{\partial f_0}{\partial T} \right\} / S \right\} \qquad (5\text{-}66)$$

Where,

$$S = \left\{ \frac{\partial f}{\partial \sigma} \right\} [D]_e \left\{ \frac{\partial f}{\partial \sigma} \right\} + \left(\frac{\partial f_0}{\partial K} \right) \left\{ \frac{\partial K}{\partial \varepsilon_P} \right\}^T \left\{ \frac{\partial f}{\partial \sigma} \right\} \qquad (5\text{-}67)$$

On a certain unit of objects, the node force at t time is to $\{F\}^e$, node displacement $\{\delta\}$, strain epsilon $\{\varepsilon\}$, stress $\{\sigma\}$. Virtual displacement principle is adopted at t+dt time.

$$\{d\delta\}^T \{F + dF\}^e = \iiint_v \{d\sigma\}^T [B]^T (\{\sigma\} + \{d\sigma\}) dV \qquad (5\text{-}68)$$

Where, $[B]$ is a unit the strain matrix.

Due to time t, the object is in equilibrium state and it:

$$\{F\}^e = \iiint_v [B]^T \{\sigma\} dV \qquad (5\text{-}69)$$

$$\{dF\}^e + \{dR\}^e = [K]^e \{d\delta\} \qquad (5\text{-}70)$$

Where, $\{dR\}^e$ is the initial strain equivalent nodal force, $[K]^e$ is the element stiffness matrix.

$$\{dR\}^e = \iiint_{\Delta V} [B]^T \{C\} dV \qquad (5\text{-}71)$$

$$[K]^e = \iiint_{\Delta V} [B]^T [D][B] dV \qquad (5\text{-}72)$$

According to the unit is in elastic or plastic condition, choose different $[D]$ and $\{C\}$ respectively. After the overall synthesis:

$$[K]\{d\delta\} = \{dF\} \qquad (5\text{-}73)$$

Where $[K] = \sum [K]^e$

$$\{dF\} = \sum \left(\{dF\}^e + \{dR\}^e \right) \qquad (5\text{-}74)$$

When a load produces at initially, the stress and strain generated in the internal of the object is elasticity, at this time; it is calculated by the elasticity theory. If the unit began to enter the yield, the way of incremental loading is necessary. As long as the load is appropriately small, the equation (4-33) can be approximately written as:

$$[K]_{i-1} \{\Delta\delta\}_i = \{\Delta F\}_i \qquad (5\text{-}75)$$

Where; $\{\Delta\delta\}_i$ is the first time I loaded the displacement increment.

$\{\Delta F\}_i$ is the first time load, and there are:

$$\{\Delta F\}_i = \frac{1}{n}\{F\} \qquad (5\text{-}76)$$

But n is a positive integer.

The plastic zone continues to expand because the gradual process of loading, making the plastic units to a neighboring part of units transforms to the transition zone units, it is an elastic state before Incremental, and after loading become plastic state units of the yield. For the units of the transition region, the stiffness matrix is obtained by using the weighted average method.

$$m = \frac{\sigma_s - \overline{\sigma}}{\Delta\overline{\sigma}} \qquad (5\text{-}77)$$

$$\left.\begin{array}{l} [\overline{D}]_{ep} = m[D]_e + (1-m)[D]_{ep} \\ \{\overline{C}\}_{ep} = m\{C\}_e + (1-m)\{C\}_{ep} \end{array}\right\} \qquad (5\text{-}78)$$

The unit stiffness matrix of transition region is to:

$$\left[\overline{K}\right]^{e} = \iiint_{\Delta V}[B]^{T}\left[\overline{D}\right]_{ep}[B]dV \tag{5-79}$$

As can be seen from equation (5-75), in the elastic region, m=1; in the plastic region, m=0; in the transition region, 0 〈 m 〈1. The equation (5-75) the size of the plastic strain in transition region is between Elastic domain and plastic domain, so that calculation accuracy is improved.

According to $E = E_0(1-25\alpha T)$ (5-37) elasticity modulus of Mg-Al alloys under different temperature was calculated.

Table5.7 calculated value of elasticity modulus of Mg-AZ31 under different temperature

	20℃	120℃	220℃	320℃	420℃
	44.55	40.98	37.40	33.83	30.25
Mg-AZ31(GPa)					
	430℃	440℃	450℃	520℃	580℃
	29.87	29.54	29.15	26.68	24.53
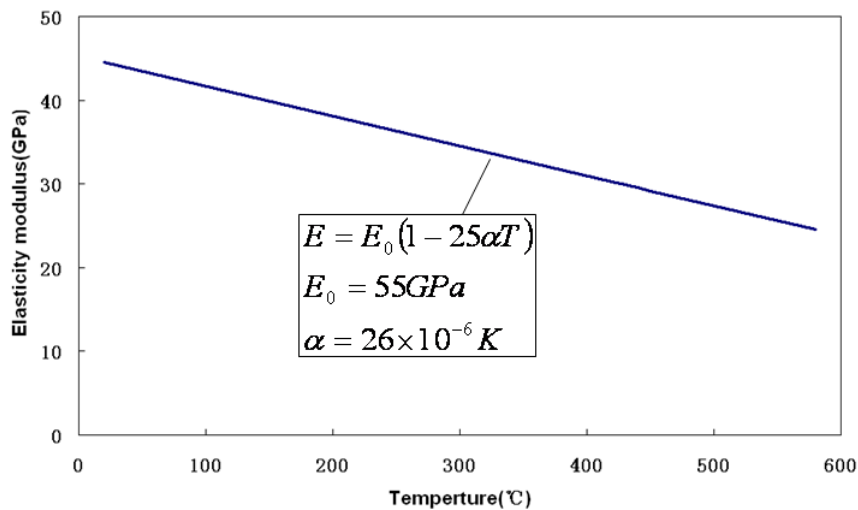
Fig. 5.8 Relation of Mg-AZ31 between elasticity modulus and temperature.

Table5.8 Calculated value of elasticity modulus of Al6061 under different temperature.

	20℃	120℃	220℃	320℃	420℃
	72.09	66.31	60.52	54.74	48.95
Al-6061(GPa)					
	430℃	440℃	450℃	520℃	580℃
	48.33	47.79	47.17	43.17	39.69
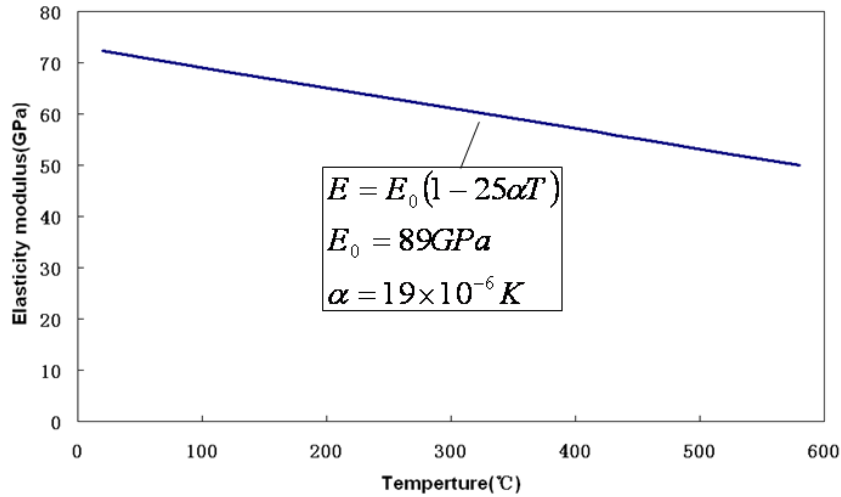
Fig.5.8 Relation of Al-6061 between elasticity modulus and temperature.

The yield strength under different temperature by the actual tensile experiment

Table5.9 Yield strength of Mg-AZ31 under different temperature.

	20℃	120℃	220℃	320℃	420℃
	162.35	140.98	127.40	73.83	23.25
Mg-AZ31(MPa)					
	430℃	440℃	450℃	520℃	580℃
	22.87	21.35	20.16	12.68	10.53
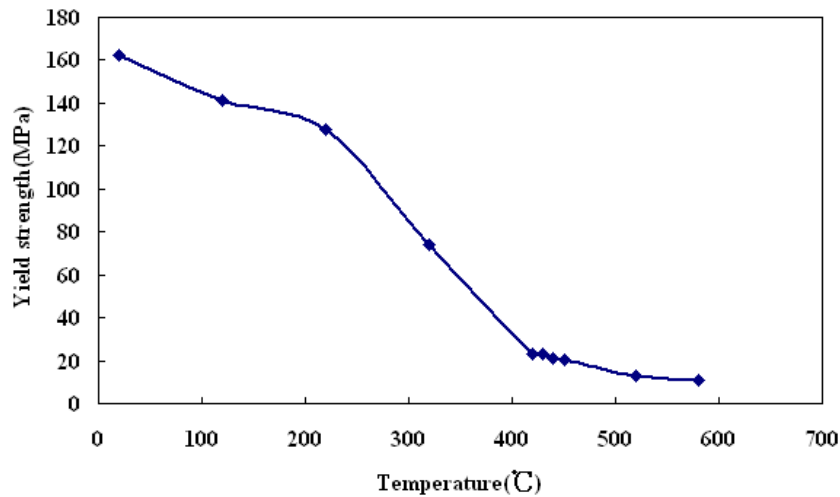
Fig.5.9 Relation of Mg-AZ31 between yield strength and temperature.

Table5.10 Yield strength of Al-6061 under different temperature.

	20℃	120℃	220℃	320℃	420℃
	75.35	70.82	64.08	36.35	13.44
Al-6061(MPa)					
	430℃	440℃	450℃	520℃	580℃
	12.66	11.24	10.12	6.33	5.26
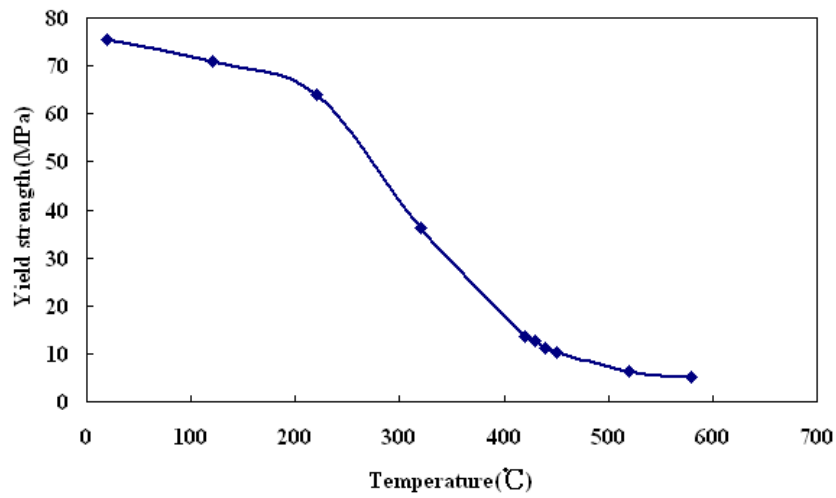
Fig.5.10 Relation of Al-6061 between yield strength and temperature.

Work hardening coefficient is the ratio of stress increment and the strain increment，Computation formula is as follows：

$$H'_T = \frac{\Delta\sigma_T}{\Delta\varepsilon_T}$$ (5-80)

Where，H'_T is hardening coefficient，$\Delta\sigma_T$ is stress increment $\Delta\varepsilon_T$ is strain increment
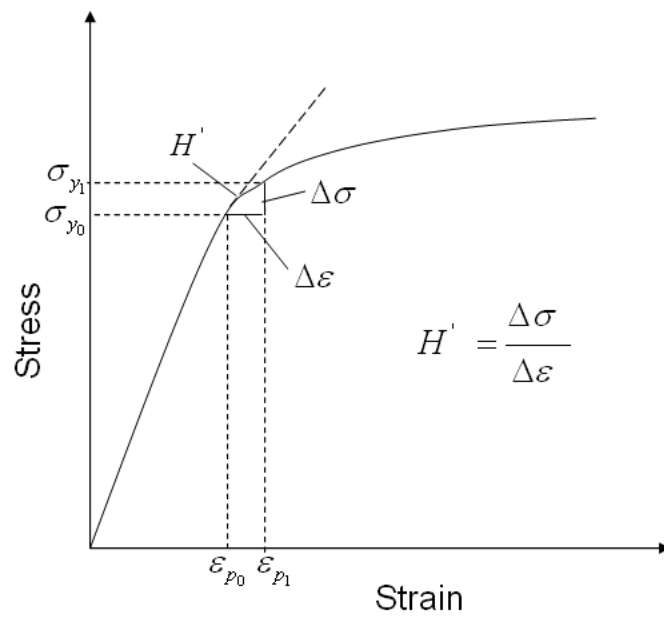
Fig.5.11 The curve of stress and strain relations

The "true strain" $\Delta\varepsilon_T$ must also be determined because as an object is stretched, the strain is distributed over a longer length of the object as opposed to being distributed over a shorter length when the object is compressed. The coefficient of strength is approximately equal to the true stress of a system when the true strain is equal to (5-80)

Table5.10 The hardening coefficient of Mg-AZ31 under different temperature.

Mg-AZ31	250℃	300℃	350℃	400℃	450℃
	316	223	166	76	8.3
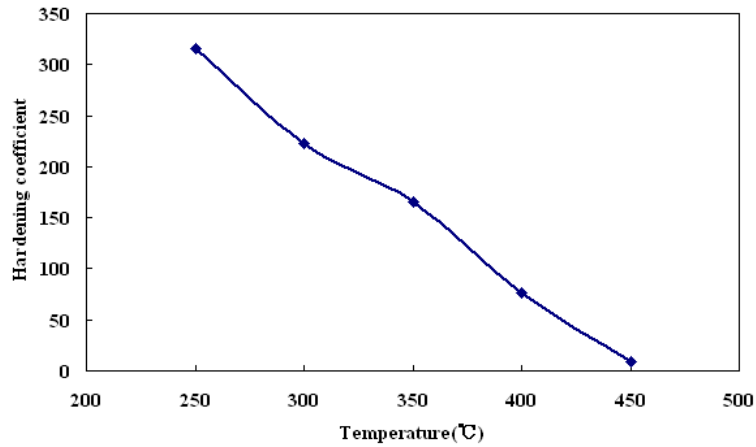
Fig.5.12 Relation of Mg-AZ31 between hardening coefficient and temperature.

Table5.11 The hardening coefficient of Al-6061 under different temperature.

Al-6061	250℃	300℃	350℃	400℃	450℃
	522	364	211	154	26
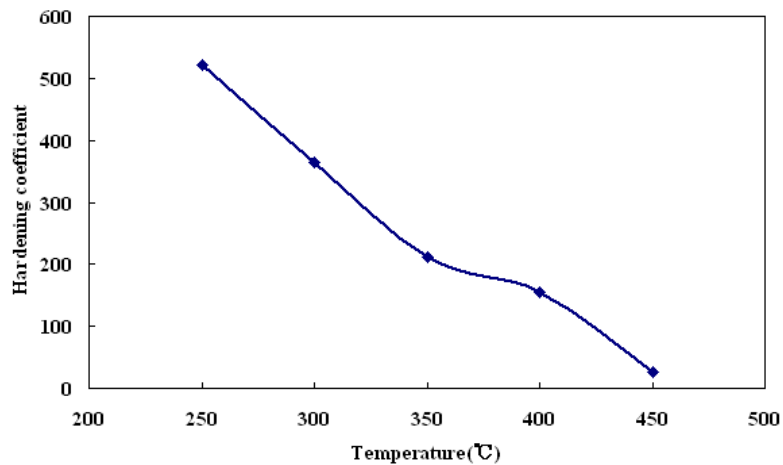
Fig.5.13 Relation of Al-6061 between hardening coefficient and temperature.

5.5 The joint interface stress field simulation under different cooling parameters

Since the test piece was constantly changing in the heating and cooling process with changing time, the mechanical properties was determined while distribution of internal stress under temperature to test piece was affected. By simulating calculation for the process of heating and cooling, we determine stress distribution under the temperature field [18]. The figure was the distribution of temperature field and stress from start to end. The left is Mg-AZ31; the right side is Al-6061. Due to the different heat capacity and thermal conductivity Mg / Al, distribution on both sides of temperature field was uneven.
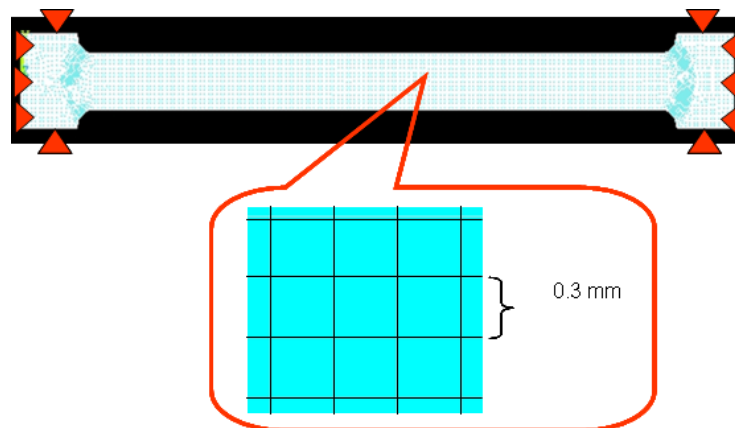
Fig.5.11 Meshing simulation diagram.
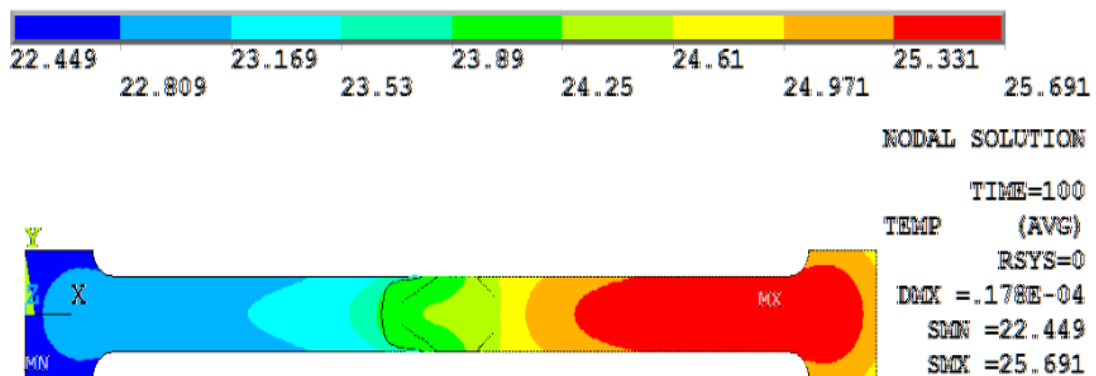
Fig. 5.12 Temperature field of Initial

Since the test piece was constantly changing in the heating and cooling process with changing time, the mechanical properties was determined while distribution of internal stress under temperature for test piece was affected. By simulating calculation for the process of heating and cooling, we determine distribution of the stress field. The study confirmed optimal cooling condition through stress distribution on X direction under simulating different cooling time (60min, 50min and 40min). Fig. 5.13(a) is the distribution of stress field at X direction when the temperature was up to 440°C.

Due to the specimen sheet was fixed in jig and all round was constrained, the whole bonding material has a large distribution of compressive stress under heating temperature caused expansion role [19]. In cooling process, Fig. 5.13(b) is middle layer stress distribution in cooling time 60min. It is found that compressive stress produced in the middle zone of bonding layer, but the position of up and down red zone was not conducive to improve the strength of the joint. When cooling time was 50min, under different cooling time to conduct simulation for stress field distribution at X direction of specimen sheet as shown in Fig. 5.13(c), the compressive stress produced in the whole bonding layer and the maximum value was reach to 277MPa.

When cooling time was reduced to 40min, the maximum compressive stress was 214MPa in middle bonding layer. As shown in Fig. 5.13(d), there are intermetallic phase generated in the middle layer, different effect intermetallic compound occurs under different cooling time. In the cooling time for 60 minutes, on the both sides of the specimen tensile stress, it was unfavorable for the joint. In the cooling time for 50 minutes, atom diffusion was moderate and compressive stress distributed on diffused interface was help to improve the strength of the joint.
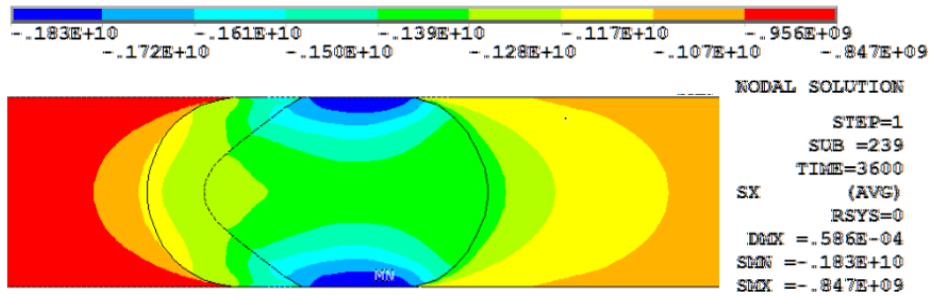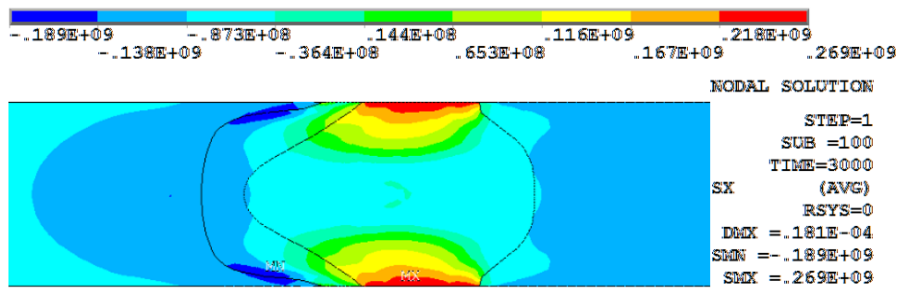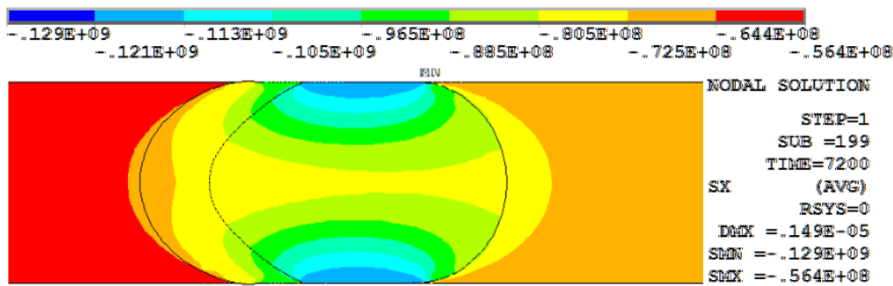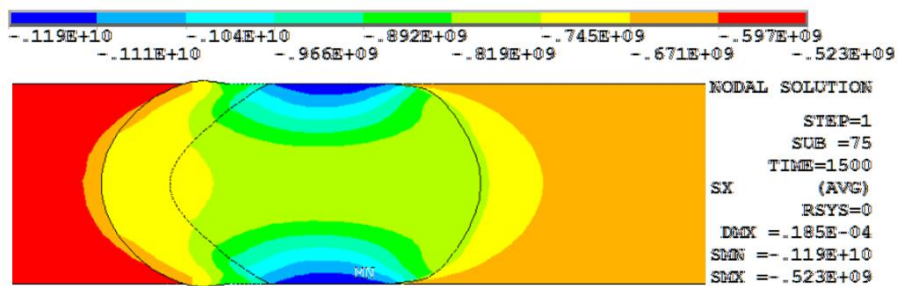
Fig.5.13 Simulated calculation of stress field on X direction of diffused bonding intermetallic compound: (a) Heating process; (b) Cooling time for 60min; (c) Cooling time for 50min; (d) Cooling time 40min.
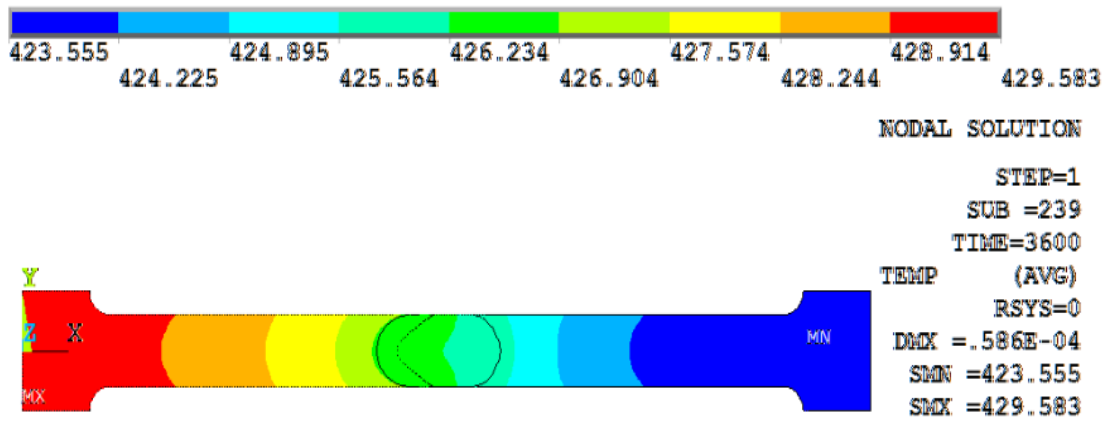
Fig. 5.14 Temperature field of finish.
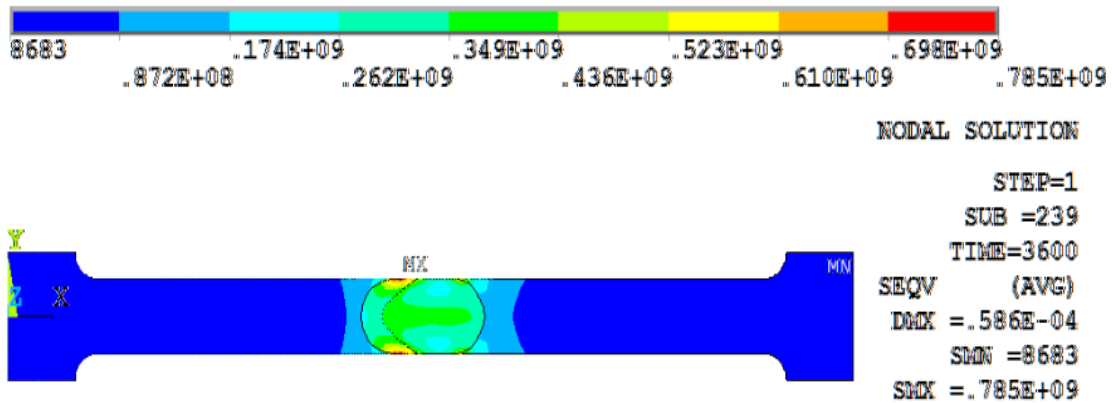
Fig. 5.15 Stress field of Initial.
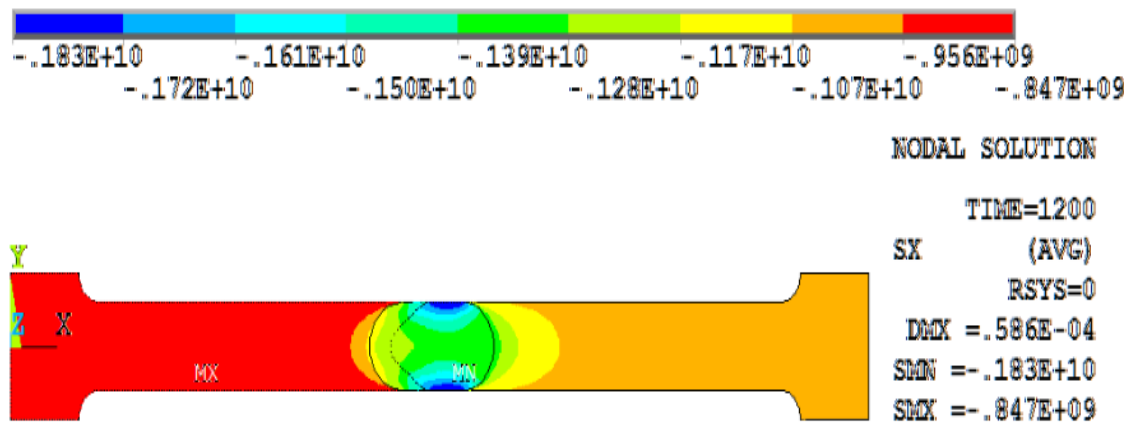
Fig. 5.16 Stress field of finish.

Stress distribution under start time 1s, middle time1800s and the end time 3600s as shown in Fig.5.19, a maximum concentration stress produced in middle layer at end of heating temperature due to intermetallic compound generated in heating temperature.
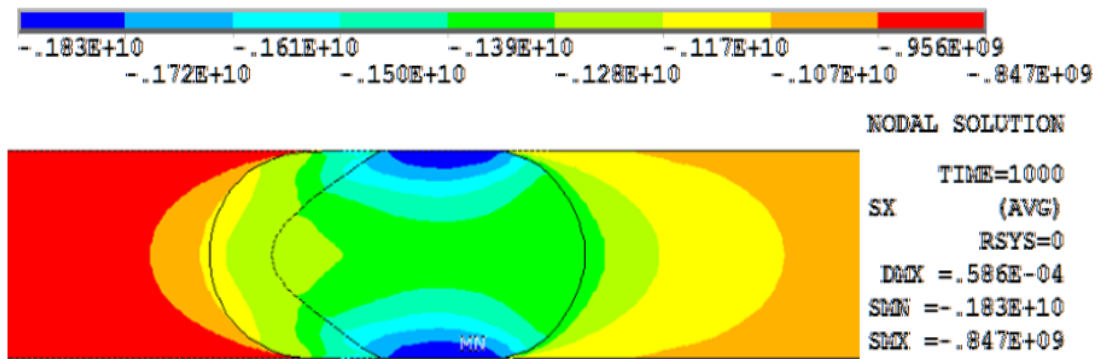
Fig.5.17 Stress field at each time point (1s).
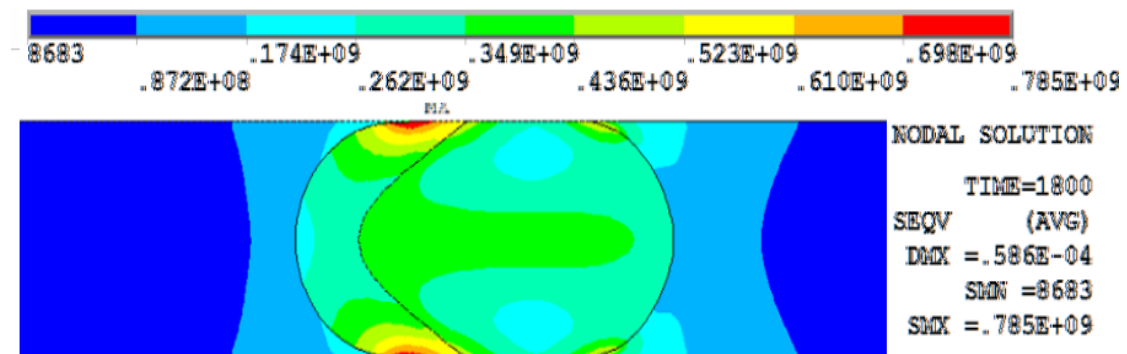
Fig.5.18 Stress field at each time point (1800s).
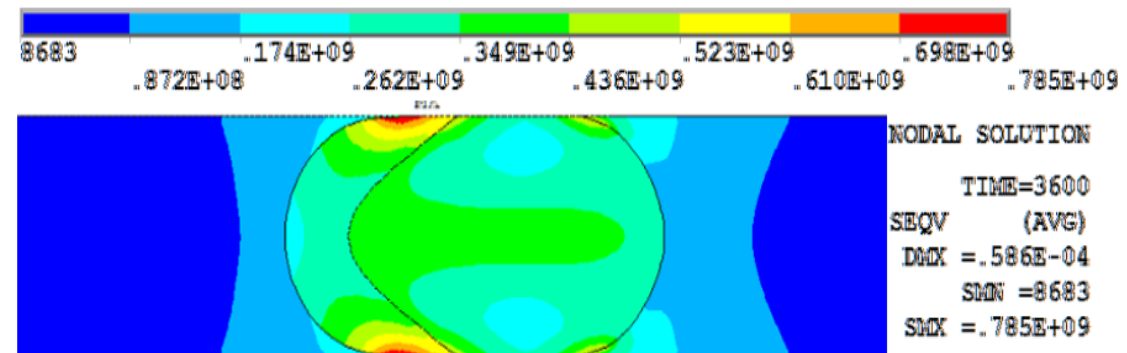
Fig.5.19 Stress field at each time point (3600s).

In cooling temperature process, temperature field and stress distributions as shown in figure, as the temperature dropped, the stress gathered produced change in bonding to transfer from Mg side to Al side. Finally, greater gathered offset to the middle layer of Al side. This result was also consistent with actually tensile to occurred fracture in Al.
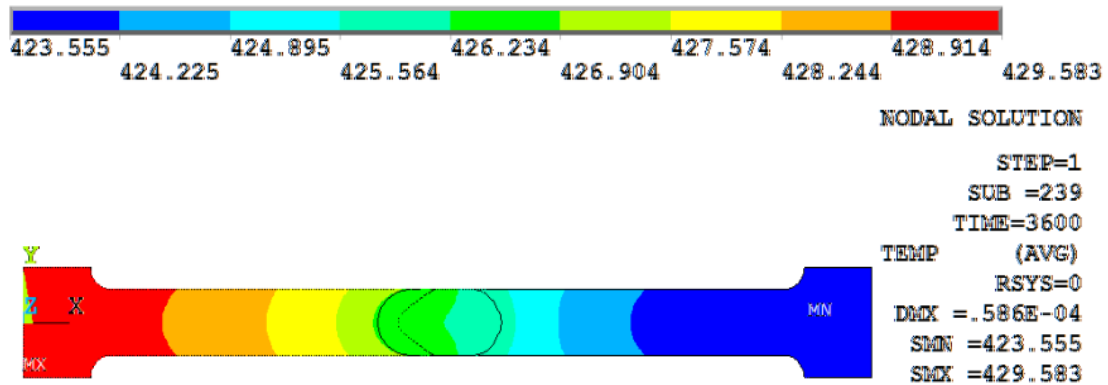
Fig.5.20 Temperature field of Initial.
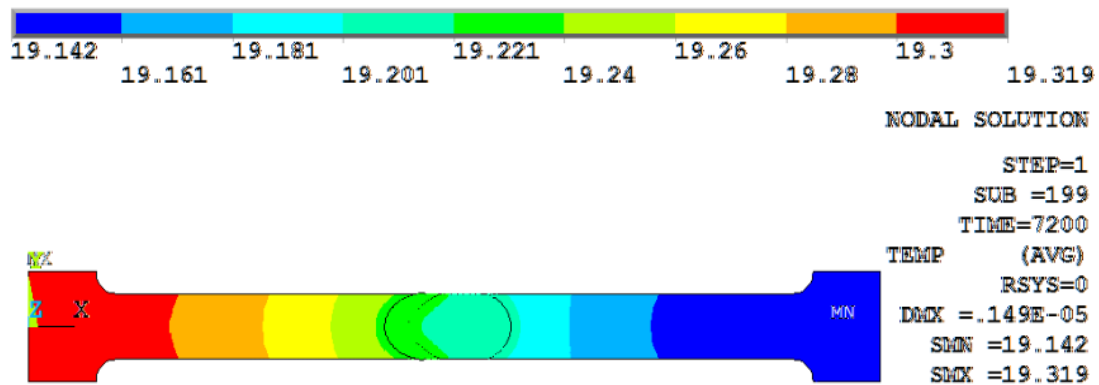
Fig.5.21 Temperature field of finish.
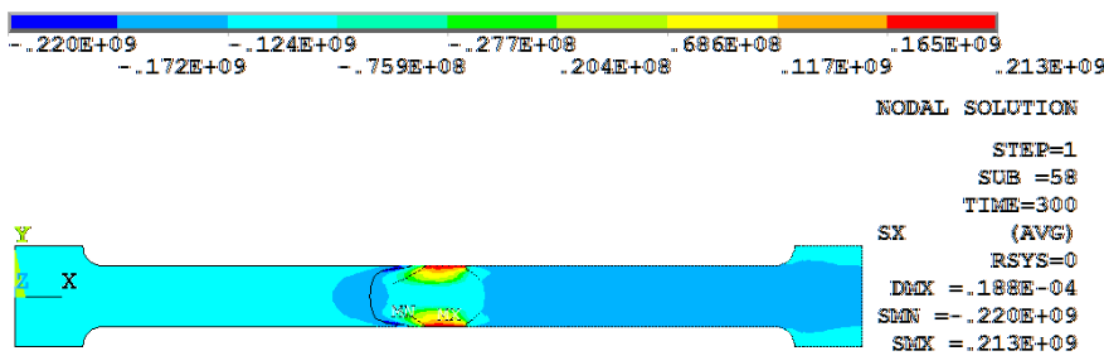
Fig. 5.22 Stress field of Initial.

The image is middle layer stress distribution in cooling time 60min. Animation as shown in below. The process clearly shows the changing trend of the stress in the cooling process, thermal stress deviated nearby Al side middle layer.
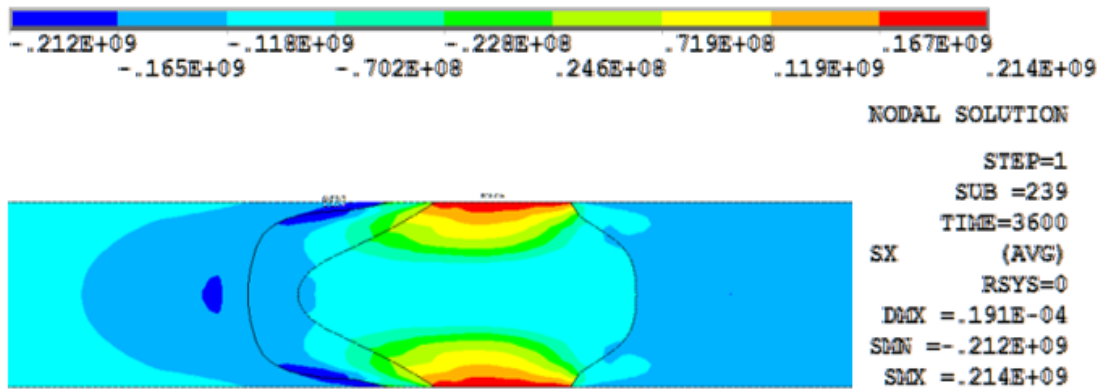
Fig.5.23 Stress field at each time point (1s).
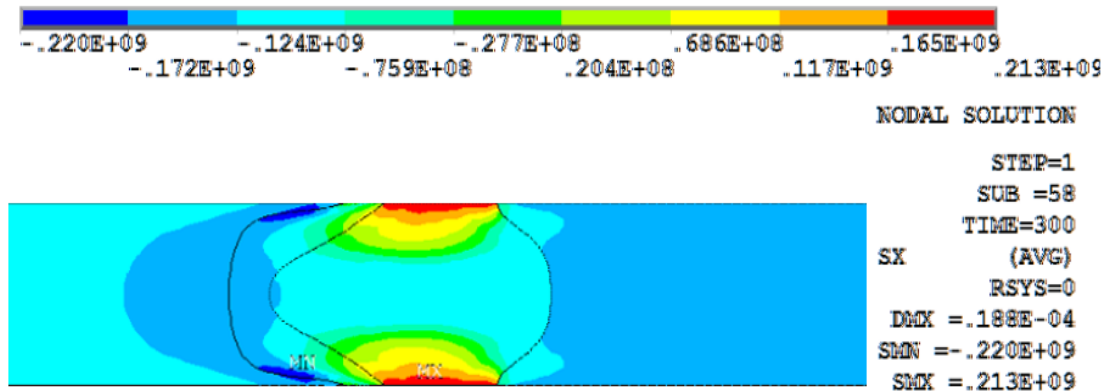
Fig.5.24 Stress field at each time point (1800s).
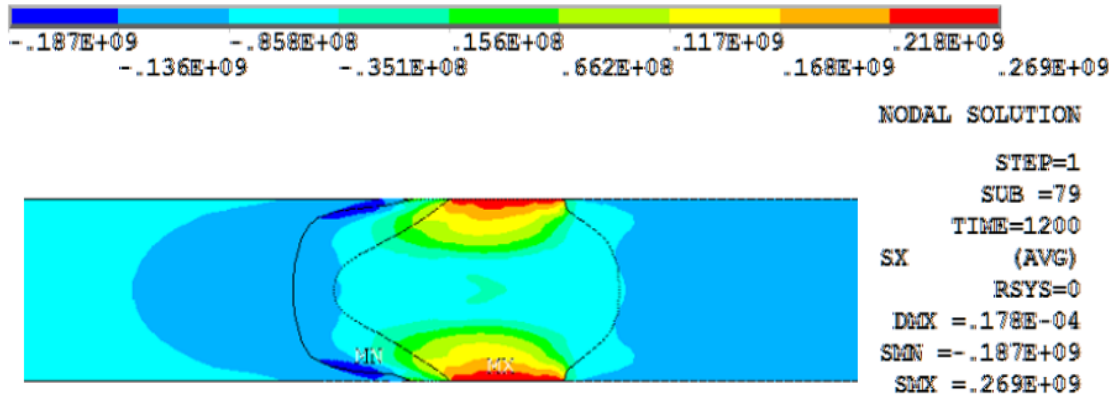
Fig.5.25 Stress field at each time point (3600s).

It is known form tensile strength for the joint under different tempering temperature, the tensile strength on the interface is 90 MPa under the tempering temperature was 200°C. Under the same heating condition, the tensile strength under tempering temperature for 300°C was 116MPa. When tempering temperature further heightens, the strength increasing gradually. It is shown that holding moderate tempering temperature played an important role for obtaining the high strength joint.
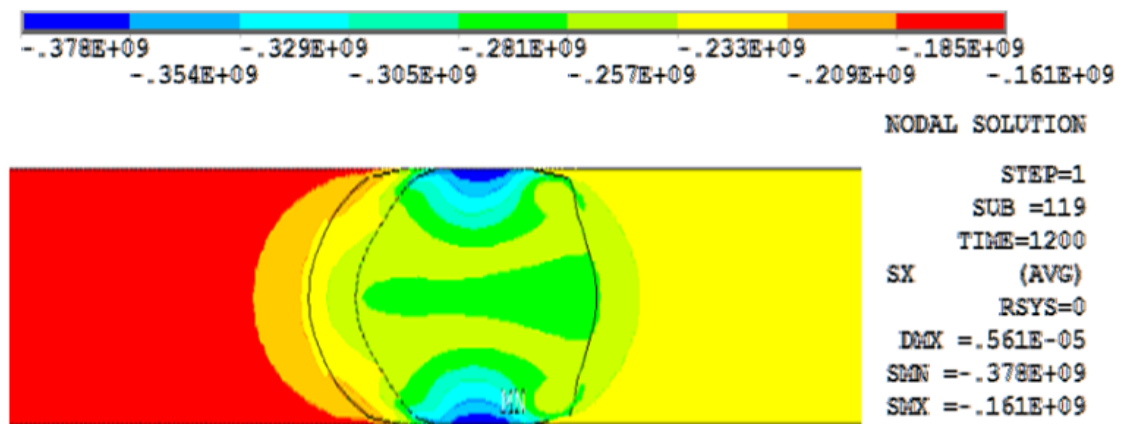
(a) Tempering temperature: 200°C
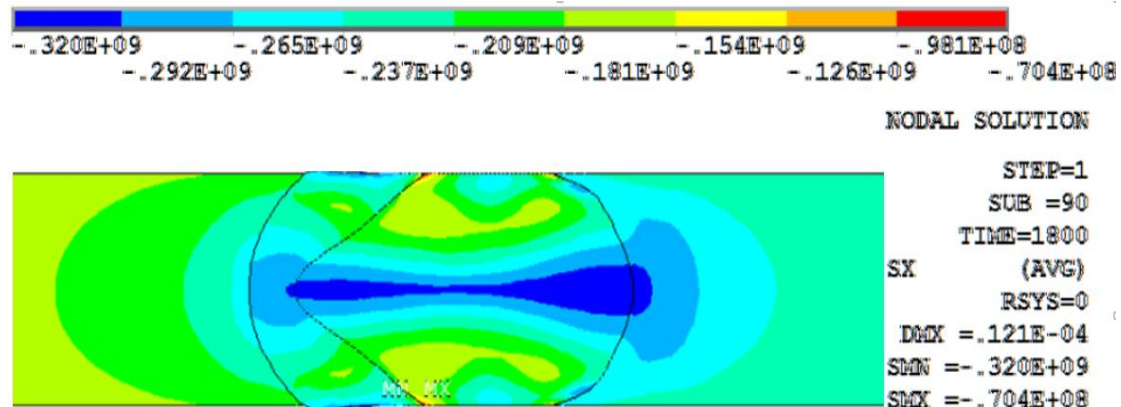
(b) Tempering temperature: 300°C

Fig.5.26 Simulated calculation of stress field on X direction of diffused bonding intermetallic compound under different tempering temperature.

5.6 Establishment of the joint mechanism and crystallization structure model

To discuss joint interface between Mg, Al, and $Mg_{17}Al_{12}$ and Mg_2Al_3 relations between the two kinds of alloy composition, structure and welding properties. First by XRD spectrum analysis of material composition, analyzes believed that $Mg_{17}Al_{12}$ as six-party heap structure, crystal indices (hkl) and interplanar spacing d $_{(hkl)}$ in accordance with formula (5-60), using the characteristic peak of (101) (110), d $_{(101)}$, and d $_{(110)}$, can be calculated for $Mg_{17}Al_{12}$ crystal cell parameters a and c value. Similarly, Mg_2Al_3 structure characteristics (105) (113) crystal surface and interplanar spacing relations, crystal cell parameters a and c values. By analyzing two kinds of structure of hexagonal system alloy, the grain boundary structure prone to twin, and found by calculation unit cell volume, the two find $V_{Mg17Al12}$, V_{Mg2Al3} meet $V_{Mg17Al12}$ = $1/2 V_{Mg2Al3}$ rule, namely to $Mg_{17}Al_{12}$ cell to be embedded into Mg_2Al_3 crystal cell provides a theoretical basis.

$$\frac{4}{3}\frac{(h^2+hk+k^2)}{a^2}+(\frac{l}{c})^2=\frac{1}{d_{hkl}^2}$$ （5-60）

In order to further understand the two kinds of alloy of material structure, combined with the above analysis, to close the six-party crystal structure of each element in the atomic radius is calculated, using the type as shown in the formula (5-61) to calculate: r_{Mg}=1.58A, r_{Al}=1.29A. Each element from the atomic radius size, Al is bigger than the atomic radius radius of Mg atoms, so according to the rules of coordination atoms, Al easy with Mg atoms to form six coordination, namely the Al atoms Mg atoms formed by the octahedral internal clearance, and stability in central $Mg_{17}Al_{12}$ crystal cell, form a stable crystalline structure of the alloy.

$$r_{sd} = -0.2436 + 0.4134e^{-0.45/n} + 7.163 \times 10^{-5}(n_{sd} - 8)^4 \qquad （5\text{-}61）$$

Calculate according to the crystal plane Angle formula (5-62), $Mg_{17}Al_{12}$ diffraction characteristics (101) (110) (021) crystal faces with Mg_2Al_3 diffraction characteristics (105) (113) crystal surface (106), the relationship between can calculate the position of twinning plane may be produced in the cell. Through calculation, the $Mg_{17}Al_{12}$ alloy structure (101) crystal surface and crystal (110) crystal plane of φ = 35.677 °, Mg_2Al_3 alloy structure (105) crystal surface and crystal (113) crystal plane of φ = 35.844 °. Due to the crystal plane Angle and orientation of the two crystals, known in Mg_2Al_3 and $Mg_{17}Al_{12}$ alloy (1011) (1123) crystal surface is easy to form the twin structure.

$$\cos\Phi = \frac{\dfrac{4}{3a^2}\left[hh' + kk' + \dfrac{1}{2}\left(hk' + kh'\right)\right] + \dfrac{ll'}{c^2}}{gg'} \qquad （5\text{-}62）$$

Based on hexagonal system general type, the twin matrix is calculated respectively born into twin crystal lattice constant a, c. And unit cell volume $V_{(1011)}$, $V_{(1123)}$. The calculation result, the twin crystal product is less than the original unit cell volume $V_{(1011)} < V_{Mg2Al3}$, before the results with the calculation results, so the form in (1011) crystal faces of twin assumptions. And crystal face (1123) formed by twin crystal cell volume were greater than the cell volume $V_{(1123)} > V_{Mg2Al3} > V_{Mg17Al12}$. This shows $Mg_{17}Al_{12}$ cell embedded in Mg_2Al_3 cell formed in the crystal cell volume increased. From this point can determine in the formation of (1123) crystal is feasible.
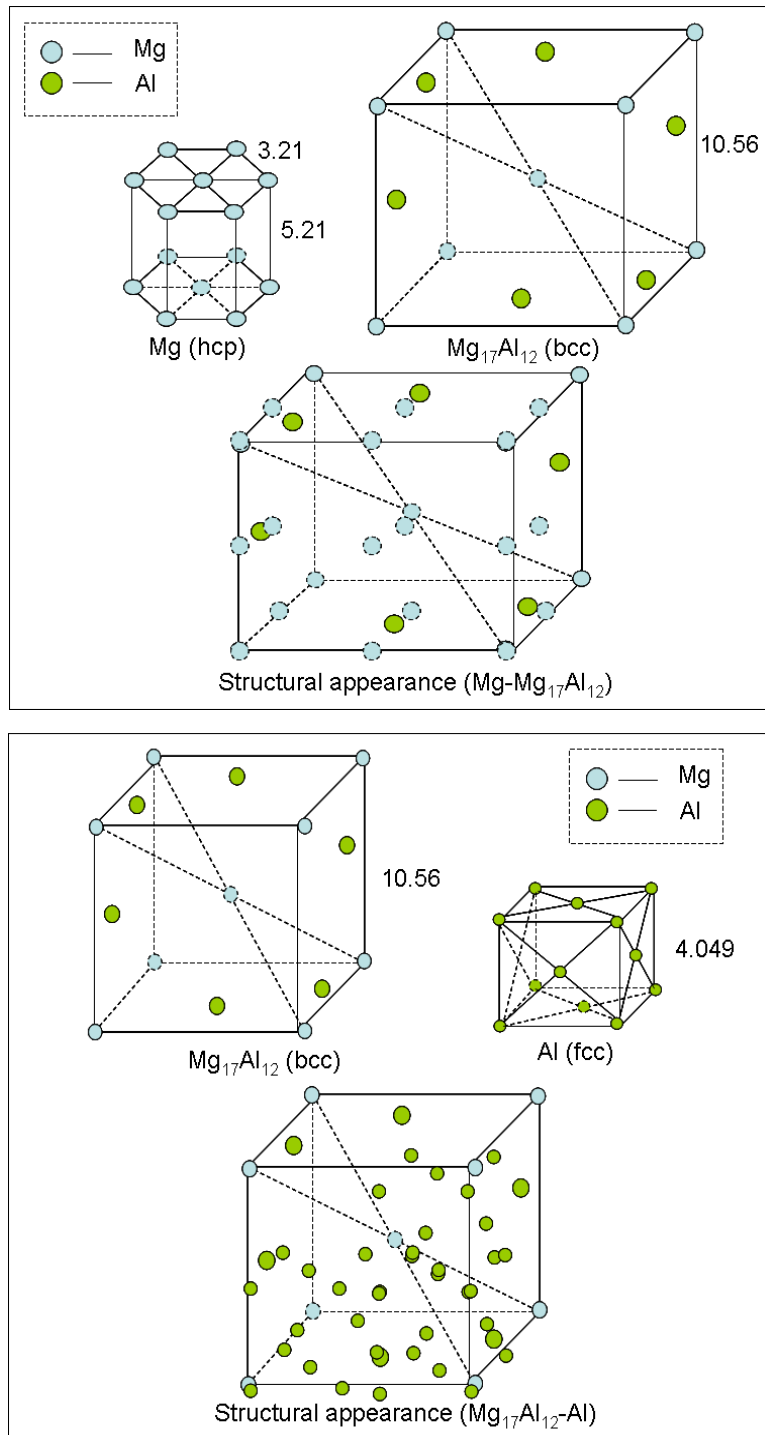
Fig.5.27 Establishment of crystallization structure model.

References

[1] Y. Sato, S. Hwan, C. Park, M. Michiuchi, H. Kokawa. Constitutional liquation during dissimilar friction stir welding of Al and Mg alloys. Scripta Mater 2004, **50**, 1233-1237.

[2] D. Singh, C. Suryanarayana, L. Mertus, R. Chen. Extended homogeneity range of intermetallic phases in mechanically alloyed Mg-Al alloys. Intermetallics 2003, **11**, 373-376.

[3] J. Cahoon. Discussion of microstructure and phase constituents in the interface zone of Mg/Al diffusion bonding. Metall Mater Trans B, 2007, **38B**, 109-112.

[4] K. Papis, B. Hallstedt, J. Loeffler, P. Uggowitzer. Interface formation in aluminium-aluminium compound casting. Acta Mate, 2008, **56**, 3036-3045.

[5] S. Ghosh, S. Chatterjee. On the direct diffusion bonding of titanium alloy to stainless steel. Mater Manu Process, 2010, **25**, 1317-1323.

[6] H. Shi, S. Qiao, R. Qiu, X. Zhang, H. Yu. Effect of welding time on the joining phenomena of diffusion welded joint between aluminum alloy and stainless steel. Mater Manu Process, 2012, **27**, 1366-1369.

[7] E. Hajjari, M. Divandari, S. Razavi, S. Emami, T. Homma, S. Kamado. Dissimilar joining of Al/Mg light metals by compound casting process. J Mater Sci, 2011, **46**, 6491-6499.

[8] X. Liu, R. Huang, H. Wang. Improvement of TIG lap weldability of dissimilar metals of Al and Mg. Sci Technol Weld Join, 2007, **12**, 258-260.

[9] A. Ben-Aartzy, A. Munitz, G. Kohn. Joining of light hybrid construetions made of magnesium and aluminum alloys. Magn Tech Seactle, 2002 295-302.

[10] W. Takehiko, S. Yoshitaka. Resistance spot welding of a magnesium alloy AZ31B plate to a 1050 aliminum plate using Ag insert metal. J Japan Inst Light Metals, 2004, **54**, 293-297.

[11] M. Harhash, S. Ataya, M. Hady, N. Mahallawy. Microstructural characterization and kinetics of diffusion bonded AZ31/Al by hot press cladding. Mater Werk, 2014, **45**, 15–20.

[12] M. Fernandus, T. Senthilkumar, V. Balasubramanian. Developing Temperature–Time and Pressure–Time diagrams for diffusion bonding AZ80 magnesium and AA6061 aluminium alloys. Mater Des, 2011, **32**, 1651-1656.

[13] Y. Jin, T. Khan. Effect of bonding time on microstructure and mechanical properties of transient liquid phase bonded magnesium AZ31 alloy. Mater Des, 2012, **38**, 32-37.

[14] L. Liu, D. Ren. A novel weld-bonding hybrid process for joining Mg alloy and Al alloy. Mater Des, 2011, **32**, 3730-3735.

[15] J. Shang, K. Wang, Q. Zhou, D. Zhang, J. Huang, G. Li. Microstructure characteristics and mechanical properties of cold metal transfer welding Mg-Al dissimilar metals. Mater Des, 2012, **34**, 559–565.

[16] I. Bhamji, M. Preuss, R. Moat, Threadgill PL, Addison AC. Linear friction welding of aluminium to magnesium. Sci Technol Weld Join, 2012, **17**, 368–374.

[17] A. Kumar, S. Sundarrajan. Selection of welding process parameters for the optimum butt-joint strength of an aluminum alloy. Mater Manu Process, 2006, **21**, 779-782.

[18] Q. Chen. Laser beam welding of AZ31 magnesium alloy with filler strip. Mater Manu Process, 2010, **25**, 1227-1232.

[19] A. Hassan, T. Qasim, A. Ghaithan. Effect of pin profile on friction stir welded aluminum matrix composites. Mater Manu Process, 2012, **27**, 1397-1401.

Chapter 6 Conclusions and recommendation

6.1 Conclusion

Empirical relationships were developed to predict the lap shear strength and bonding strength of diffusion bonded joints of Al-6061 and Mg-AZ31, incorporating diffusion bonding parameters such as bonding temperature, bonding pressure, holding time and surface roughness of the materials. The relationships between the optimum process parameters and the percentage of aluminum and zinc in magnesium alloys were established. The optimum process parameters can be evaluated by varying the percentage of aluminum in magnesium alloys. The effect of process parameters such as bonding temperature, bonding pressure, holding time and surface roughness on shear strength, bonding strength, diffusion layer thickness were analyzed. Scanning electron microscopy, transmission electron microscopy, electron dispersive spectrum and X-ray diffraction techniques were used to characterize the joints.

The following conclusions are drawn from the series of experimental and theoretical studies:

(1) The result of diffused welding interface tensile strength indicated that the maximum shear strength was 110MPa under 440°C. Holding time and cooling rate process parameters were discussed according to the affects of bonding strength.

(2) Mg side mainly emerged quasi-cleavage and intergranular crack on Mg/Al alloy diffused welding interface fracture and Al side was mixed fracture morphology. The fracture of diffused welding joint was affected by base material and brittleness phase in diffused area and connected with formed cracks and micro-pores nearby Al side, finally, the fracture produced close to a side of base material.

(3) According to organizational features on interface diffused zone, interface transition zone was constituted of Al side transited layer, the middle diffused layer and Mg side transited layer. Boundary from three zones was more obvious. Compounds analysis of electron microprobe showed transited zone was constituted of elements Mg, Al and Zn and diffused zone, the size was about 20μm.

(4) A small amount of pores generated on Al side, diffused pores formed because the diffusion of Mg atoms to Al side in the diffused welding process, therefore, it is difficult to form density new phase layer and diffused pores formed nearby Al side transited layer.

(5) EPMA analysis results of Mg/Al dissimilar metals on diffused interface transited zone indicated that relatively independent concentration distributed zone generated on diffused welding interface transited zone. With diffused temperature increasing, the wide was generally increasing and the interface distribution was not uniform under long holding time.

(6) X-ray diffraction had shown that $Mg_{17}Al_{12}$ and Mg_2Al_3 alloy phases formed the diffusion of elements Mg and Al nearby Mg/Al diffused welding interface. Interface transited zone phase structure from Mg side to Al side was constituted of $Mg_{17}Al_{12}$ and Mg_2Al_3 in turn.

(7) Transmission electron microscopy observation had shown that Mg mainly appeared lump hexagonal crystal structure and Al was α-Al of fcc structure. $Mg_{17}Al_{12}$ phase distributed on Mg substrate and Mg_2Al_3 phase distributed on Al substrate. EDS composition analysis was also further proved the existing of $Mg_{17}Al_{12}$ and Mg_2Al_3 phases. On Al side transited layer, a large of mesh distributed edge dislocation produced to cause the one of reasons formed cleavage fracture.

(8) Process parameters were optimized by simulating stress field on interface. The best cooling rate was 10℃/min. The hardness of intermetallic compound $Mg_{17}Al_{12}$ reached 250HV, the hardness value caused brittle fracture and the hardness of intermetallic compound Mg_2Al_3 was lower, so that

alleviated the brittle on interface improved the strength on interface.

Table 6.1 Comparison of Mg-AZ31/Al-6061 with different bonding method

	Without pressure	Pressure
Interfacial microstructure		
Diffusion distance		
Intermetallic compound	$Mg_{17}Al_{12}$, Mg_2Al_3	$Mg_{17}Al_{12}$
Bond strength	110 MPa	90 MPa
Contact reaction brazing [1]		45 MPa
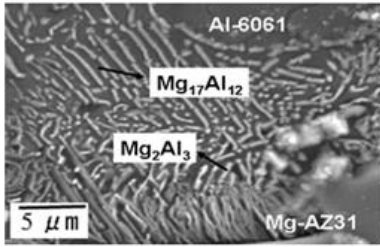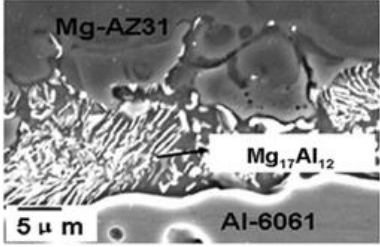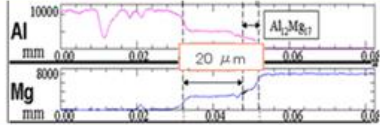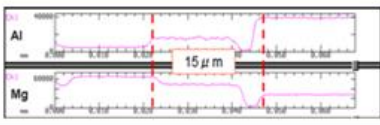
[1] L.M. Liu, J.H. Tan, X.J. Liu. Reactive brazing of Al alloy to Mg alloy using zinc-based brazing alloy. Materials Letters, 2007, 61, 2373-2377.

6.2 Recommendation

The future work as shown in followings:

1. The constitutive of relation of intermetallic compound phases $Mg_{17}Al_{12}$ and Mg_2Al_3 was confirmed. According to the relation, the simulating was conducted for bonding process, so that to further optimize bonding conditions.
2. The toughness on bonding interface was improved through tempering treatment process to reduce the hardness of intermetallic compounds, so that achieved the strength of the joint.

Related publications of the author

[1] Ming Zhao, Dongying Ju: Investigation of bonding interface and strength properties in diffusion bonding of MgAZ31/Al6061. Materials Science Forum Vol. 750 (2013) pp 160-163.

[2] Ming Zhao, Dongying Ju: Diffusion bonding of Mg-AZ31B / Al-6061 and characteristics with pressure and with no pressure. Advanced Materials Research Vols. 834-836 (2014) pp 812-815.

[3] Ming Zhao, Dongying Ju: Affects of heat treatment on strength of Mg-AZ31/Al-6061 alloy diffused bonding process. Materials Science Forum.(In printing)

[4] Ming Zhao, Dongying Ju:Effects of intermetallic compounds on diffusion bonding process of Mg-AZ31/Al-6061 alloy. Materials and Manufacturing Processes. (In review).

[5] Ming Zhao, Dongying Ju:Effects of intermetallic compounds diffused layers on MgAZ31/Al6061 bonding under pressure. Journal of Materials Engineering and Performance. (In review).

[6] Dongying Ju, Ming Zhao: Diffusion Bonding of 3Y-TZP and SUS440 by Using of Ti-Cu Powder/Sheet. Advanced Materials Research Vols. 314-316 (2011) pp 957-962.

[7] Ming Zhao, Dongying Ju: Analysis of bonging and interfacial characterization of 3Y-TZP and SUS304 by diffusion bonding. Materials Science Forum Vol. 750 (2013) pp 164-167.

Acknowledgements